Engineering Microbubbles with the Buried-Ligand Architecture for Targeted Ultrasound Molecular Imaging

Cherry Chen Chen

Submitted in partial fulfillment of the
requirements for the degree of
Doctor of Philosophy
in the Graduate School of Arts and Sciences

COLUMBIA UNIVERSITY

2011

ABSTRACT

Engineering Microbubbles with the Buried-Ligand Architecture for Targeted Ultrasound Molecular Imaging

Cherry Chen Chen

Microbubbles are gaseous microspheres stabilized with phospholipid monolayer shells. Because of their compressible gas core, they are highly echogenic. Taking advantage of this property, microbubbles are used as ultrasound contrast agents for signal enhancement. In addition, they are being developed for targeted diagnostic molecular imaging applications. Previous studies have shown that targeted microbubbles could induce complement activation and reduce their circulation persistence. In order to avoid the undesired immune response, a novel stealth microbubble design that consisted a bimodal poly(ethylene glycol) (PEG) brush layer, named buried-ligand architecture (BLA), was introduced. However, in order to utilize this BLA design for targeted imaging, it is essential to characterize the kinetics of ligand conjugation to BLA microbubbles and further study their *in vitro* and *in vivo* immunogenicity and contrast persistence properties.

In this project, ligand conjugation to BLA microbubbles was characterized using molecules with large molecular weight difference. Microbubbles with various PEG surface architectures were formulated, and ligands with large molecular weight difference were used to conjugate to the microbubbles in order to study the feasibility of generating targeted microbubbles using the post-labeling technique. It was shown that small ligands could be conjugated to BLA microbubbles to generate targeted contrast agents using post-labeling. A surprising result was observed during the experiment that complex surface microstructures could

be induced simply through streptavidin-biotin binding. This was the first time that these wrinkled structures were generated on the surface of microbubbles using a non-mechanical method.

In vitro immunogenicity studies showed that BLA microbubble indeed induced less complement activation than microbubbles with monomodal PEG brush layers, or exposed-ligand architecture (ELA) microbubbles. *In vivo* contrast persistence studies further demonstrated the improved circulation time of the BLA microbubbles and showed that the buried-ligand design did not compromise their ability for signal enhancement. The results presented in this project supported the previous findings that microbubbles with the buried-ligand architecture had reduced immunogenicity with prolonged circulation persistence and were more suitable to be developed for targeted molecular imaging applications.

Table of Contents

List of Tables

List of Figures

Acknowledgments

I would first like to thank my mother for her love, encouragement and support, for teaching me the value of good spirit and hard work. Without her, I would not be able to accomplish what I have achieved, or even one tenth of that.

I would like to thank my advisor, Dr. Mark Borden, for his constant support throughout my PhD life at Columbia University. He has taught me to think like a true scientist, to ask critical questions and not to say yes to all the results I am given. I owe a great deal of gratitude for his guidance.

I would like to thank Dr. Shashank Sirsi, for his countless efforts in helping me with my projects and keeping me on track to becoming a successful researcher. I am extremely privileged to have you as a mentor and a friend.

I would like to thank my committee members, for donating their time and expertise in helping me to complete this work.

In addition, I would like to thank Dr. Jovan Mijovic and Dr. Mary Cowman at Polytechnic University, for mentoring me during my undergraduate studies and helping me to discover my true interest in science. I would like to thank Dr. Peter Burns and everyone else from the Burns research group at the University of Toronto, for helping me during one of the most difficult times of my graduate years.

I also would like to thank the Hsu family, Warren, Lotus, Ted, Greg and Joanna, for taking me in like one of your own and giving me a home in this foreign land.

Lastly, I would like to thank all my friends, for supporting me at all times, good and bad; for accepting me for whom I am; for keeping me sane during the darkness and chaos. New York City is so much more enjoyable with you guys being here with me.

Dedication

To my mother, for having always stayed behind me with endless patience and unconditional love; for not giving up on me at times when all things seemed hopeless and impossible; for being my hero and my friend.

Chapter 1: Introduction

1.1. A Historical Perspective

1.1.1. The Discovery of Microbubbles

Merriam-Webster dictionary defines the word “bubble” as “a small globule body of gas within a liquid”. Microbubbles typically refer to gas-in-liquid emulsions with diameters ranging between 0.5-100 μm. Dilute air microbubbles occur in natural waters, and can be remarkably stable for hours, or even days (D'Arrigo 2003). The existence of naturally occurring microbubbles has been demonstrated in fresh water (Dean 1944), sea water (Johnson and Cooke 1981) and even blood and other body fluids (Harvey, Whiteley et al. 1944) by many investigators over the last century. These stable suspensions are topics of great concern to scientists and engineers in many fields with profound practical importance. In waste-water treatment, small microbubbles are required to efficiently separate colloidal pollutants from water during microflotation (Cassell, Kaufman et al. 1975; D'Arrigo 2003). In marine biology, the presence of bubbles in the near-surface region of the ocean has great significance over a number of oceanographic processes, such as converting organic carbon to particulate form through 3). In meteorology, air bubbles produced by breaking waves carry surface-active organic materials upon rising to the ocean surface and eject them into the air in the form of aerosols upon breaking and, therefore, affect the local air quality and rain formation (Blanchard 1975; D'Arrigo 2003). Among technological applications that utilize high power ultrasound, acoustic cavitation (the inertial collapse of a microbubble) is widely accepted as the main effector that determines the

efficiency of processes such as ultrasonic cleaning (Pohlman, Werden et al. 1972; Zeqiri, Gelat et al. 2003).

Indeed, microbubbles have a wide range of importance across many scientific fields. The origin of their long lasting stability, therefore, becomes the next important topic for scientists and engineers to study. The theory of microbubble surface stabilization was proposed in the early 1900s. Langmuir and Adam showed that a clean water surface, if left standing without cover, would soon be covered by a monomolecular organic layer (Langmuir 1917; Fox and Herzfeld 1954). Fox and Herzfeld proposed that these organic molecules, such as fatty acids, spontaneously encapsulate naturally occurring air bubbles in fresh water and serve as stabilizing agents as the bubbles are compressed (Fox and Herzfeld 1954). Experimental work done by Johnson and Cooke using photomicrography to observe the dissolution of microbubbles in seawater revealed that some bubbles did not dissolve completely; instead, “they stopped decreasing in size abruptly, sometimes becoming slightly aspherical, and remained as microbubbles apparently stabilized by films compressed during dissolution” (Johnson and Cooke 1981; D'Arrigo 2003). It was suggested that “some mechanical or diffusion-limiting effect that resists further bubble dissolution is activated during bubble contraction and the attendant compression of encapsulating surface films” (Johnson and Cooke 1981). Biochemical analysis of the surfactant found on natural microbubbles showed that it is mainly, if not all, composed of hydrophobic paraffinic lipids and glycoproteins that are partial degradation products of biological origin (D'Arrigo 2003). Interestingly, the surfactant systems widely used today for microbubble encapsulation in many industrial and biomedical applications are designed to be composed of similar materials, attempting to mimic the natural process of microbubble formation.

Microbubbles are currently used in a large scope of industrial and technological applications. As mentioned earlier, microbubbles are used in microflotation for wastewater treatment because of their large surface area and relatively slow rise velocities (Cassell, Kaufman et al. 1975; Kojima 2010). As microbubbles rise in wastewater, they come into contact with organic pollutants and other low-density particulates and carry them to the surface to form a collective foam layer for subsequent separation and purification processes. In the mineral industry, fine particles are separated from solutions using microbubbles in a similar fashion called electroflotation (Kraizman 1974). Electroflotation is a simple process that floats particles to the surface of a water body by microbubbles of hydrogen and oxygen gases generated from water electrolysis (Chen 2004). Because of the high surface-area-to-volume ratio, microbubbles are ideal for mass and energy transfer. In the bioprocessing industry, yeast biomass production mainly depends on the oxygen transfer efficiency of the aeration system carried out by microbubbles (Ago, Nagasawa et al. 2005). In the pharmaceutical industry, bioreactors require microbubble aeration systems to carry out similar air/oxygen mass transfer (Zimmerman, Tesar et al. 2008). In the more recent years, microbubbles have received increasing attention for biomedical applications. In the next section, a detailed developmental history of microbubbles as ultrasound contrast agents for diagnostic imaging is reviewed.

1.1.2. The Development of Ultrasound Contrast Agents for Diagnostic Imaging

The clinical use of microbubbles as ultrasound contrast agents originated with a chance discovery by a cardiologist, Dr. Claude Joyner, in the late 1960s (Gramiak and Shah 1968; Cosgrove and Harvey 2009). While performing an M-mode echocardiogram, he noticed a

transient increase in ultrasound signal in the aortic root each time an injection of saline solution was made via a cardiac catheter (Becker and Burns 2000; Kaufmann, Wei et al. 2007; Cosgrove and Harvey 2009). Subsequent research revealed that it was the free air bubbles, either suspended in the saline solution or formed at the tip of the catheter during the injection, not the liquid itself, responsible for the observed echo-enhancement. This exciting discovery initiated new investigations and the development of contrast enhanced ultrasound over the next several decades, and it ultimately led to the commercial exploitation of microbubbles as ultrasound contrast agents for diagnostic imaging applications.

Initial experiments with contrast agents relied on intracoronary injections of hand-agitated or low-energy sonicated free air bubbles to produce myocardial enhancement (Kaufmann, Wei et al. 2007). However, these techniques typically involved toxic chemical compounds such as hydrogen peroxide to generate the microbubbles (Kemper, Oboyle et al. 1983; Feinstein, Tencate et al. 1984). In addition, they were limited by the wide size range of microbubbles produced and the potential for large bubbles to be trapped within the microcirculation (Becker and Burns 2000; Kaufmann, Wei et al. 2007). In order to improve microbubble biocompatibility, reproducibility and clinical feasibility, attention was turned towards the development of stabilized microbubbles with diameters less than 10 μm in order to ensure the free passage of the contrast agents through the heart and pulmonary capillary network. High-energy sonication was utilized in an attempt to improve the size distribution. However, the microbubbles produced, typically from iodinated radiopaque contrast agents, were shown to acutely alter the hemodynamics, and their short persistence time still did not allow for intravenous administration (Gillam, Kaul et al. 1985; Moore, Smucker et al. 1986; Lang, Borow

et al. 1987). Figure 1.1 illustrates how a bolus injection of microbubble contrast agents may be used to assist the diagnosis of myocardial diseases during contrast echocardiography.

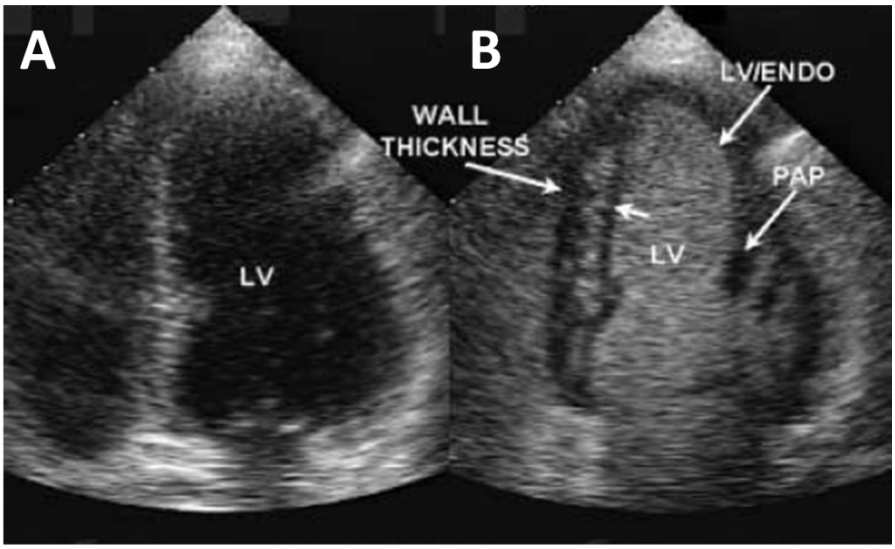

Figure 1.1. Left ventricular cavity opacification using microbubble contrast agents. (A) View of the left ventricle (LV). (B) The same view after a bolus injection of Imagent microbubble contrast agent. The left ventricle (LV), endocardial border (LV/ENDO) and papillary muscle (PAP) are clearly seen after microbubble injection, which allows myocardial thickening to be evaluated. When watching the heart in motion, normal functioning heard muscle thickens as it contracts, while abnormal heart muscle moves less and does not thicken. Taken from Schutt et al. (Schutt, Klein et al. 2003).

Surfactant encapsulated microbubbles dramatically advanced the contrast agent research field by solving many of the issues associated with stability and size distributions. The challenge was first met in 1984 by Feinstein et al. (Feinstein, Shah et al. 1984), who produced stable microbubbles by sonicating a solution of human serum albumin and showed through direct

microscopic visualization that they could pass through the capillary vasculature unhindered, similar to red blood cells, after a peripheral venous injection. This agent was subsequently developed commercially into Albunex (Molecular Biosystems, Inc., San Diego, CA), the first product approved by the US Food and Drug Administration (FDA) for use in the United States. A list of examples of commercially available contrast agents is presented in Table 1.1.

Table 1.1. Reported doses for commercially available microbubble contrast agents

Name	Shell Material	Gas	Concentration (mL^{-1})	Mean Diameter (μm)	Recommended Dose[†]
Albunex	Albumin	Air	$3.0\text{-}5.0 \times 10^8$	3-5	15-20 mL
Definity	Lipid	Perfluoropropane	1.2×10^{10}	1.1-3.3	10 μL/kg BW[*]
Echovist	Galactose	Air	200-300 mg	2	3.0-10.0 mL
Imagent	Lipid surfactant	Perfluorohexane	$5.9\text{-}13.7 \times 10^8$	6[+]	6.25 μL/kg BW[*]
Levovist	Galactose/Lipid	Air	200-400 mg	2	6.5-19.5 mL
Optison	Albumin	Perfluoropropane	$5.0\text{-}8.0 \times 10^8$	3.0-4.5	0.5-3.0 mL
Sonazoid	Lipid	Perfluorobutane	1.2×10^9	3[+]	15 μL/kg BW[*]
SonoVue	Lipid	Sulfur hexafluoride	2.0×10^8	3	2.0-2.4 mL

[*] **Per kilogram of body weight**

[+] **Based on volume-weight, all other mean diameters are expressed as number-weight**

[†] **Bolus intravenous injection into peripheral vein**

Modern, first-generation contrast agents still used air as the core gas. These air bubbles were surrounded by a fatty acid, lipid, or protein shell (Miller, Averkiou et al. 2008). The encapsulating shell increased the stability of the microbubbles both in the vial and during circulation. In addition to Albunex, other commercially available first-generation contrast agents included Echovist (SH U454; Schering AG, Berlin, Germany) and Levovist (SH U508 A;

Schering AG, Berlin, Germany), both of which were microcrystalline galactose microspheres, with improved formulation made for Levovist using palmitic acid coating for further stabilization. Both Echovist and Levovist were only available in Europe, Canada and part of Asia for Doppler enhancement of the liver, kidney and heart. The other uses of Echovist and/or Levovist were in contrast sonography in gynecology to assess uterus abnormalities (Becker and Burns 2000; Quaia 2005; Greis 2008; Miller, Averkiou et al. 2008).

One of the problems with "first generation" microbubbles was the limited persistence and efficacy after intravenous injections (Miller, Averkiou et al. 2008). Because of the inherent unsaturation of dissolved gasses in blood owing to alveolar ventilation-perfusion mismatch (Gattinoni, Carlesso et al. 2011), the air contained within these microbubbles readily diffused out, resulting in a very short half-life (~1 min) and the inability to produce sufficient ultrasound contrast for most diagnostic applications (Quaia 2005). In order to solve this problem, "second generation" contrast agents utilized inert gases with low solubility and diffusivity, such as perfluorocarbons and sulfur hexafluoride gas (SF_6). These microbubbles retained their gas core for a longer period of time. Thus, the duration of contrast enhancement was increased from several seconds to several minutes (van Liew and Burkard 1995; Miller, Averkiou et al. 2008). Table 1.2 lists the solubilities and diffusivities of several commonly used inert gases for the stabilization of the second-generation microbubble contrast agents.

Optison (FS-069; GE Healthcare, Princeton, NJ) obtained approval from the FDA for echocardiography in 1998 as the first second-generation (non-air) contrast agent. As with Albunex, Optison also contains human serum albumin as the encapsulating microbubble shell, but it uses perfluoropropane gas, instead of air, for the gas core. The relatively insoluble gas is inert and eliminated through normal gas exchange in the lung (Schutt, Klein et al. 2003).

Optison was shown to opacify the left ventricular chambers at doses much smaller than Albunex (0.5-3 mL compared with 15-20 mL, respectively) and for a much longer period of time (>5 min compared with 30-45 seconds, respectively) (Quaia 2005; Miller, Averkiou et al. 2008).

Table 1.2. Critical characteristics of various filling gases used for microbubble stabilization (Schutt, Klein et al. 2003; Borden and Dayton 2008; Borden, Qin et al. 2010)

Gas	Gas Solubility in Water (25 °C) (mol/m^3)	Gas Diffusivity in Water x 10^6 (cm^2/s)*
Nitrogen (N_2)	0.63	20
Perfluorobutane (n-C_4F_{10})	0.021	6.9
Perfluorohexane (n-C_6F_{14})	2.7×10^{-4}	5.8
Perfluoropropane (n-C_3F_8)	0.19	7.7
Oxygen (O_2)	1.32	21
Sulfur Hexafluoride (SF_6)	0.27	6.7

*** For N_2 and O_2, data is measured at 25 °C; for all other gases, data is measured at 20 °C**

Definity (MRX-115, DMP-115; Lantheus Medical Imaging, North Billerica, MA) is another agent that uses perfluoropropane as the gas core for contrast enhancement. But this agent uses a monolayer of phospholipids as the shell material for stabilization. It requires a 45-second mechanical agitation for activation in a dental amalgamator. Small volumes of these microbubbles opacify the left ventricular chamber and enhance the Doppler signal from the peripheral vasculature for prolonged periods of time (Kitzman, Goldman et al. 2000). The microvascular rheology of Definity has been shown to be similar to that of red blood cells in circulation (Miller, Averkiou et al. 2008), and the gas elimination routes and shell metabolism is believed to be similar to Optison (Borden, Qin et al. 2010). Definity was the first lipid-coated second-generation contrast agent approved by the FDA for echocardiography and in Canada and

part of Europe for liver and kidney imaging. More recently, Definity obtained its approval for echocardiography in India, Australia, New Zealand, parts of the Pacific Rim and several countries in the Middle East.

A similar contrast agent, Imagent (AFO-150; IMCOR Pharmaceuticals, San Diego, CA), also contains a perfluorocarbon gas core (perfluorohexane) to increase its *in vivo* circulation persistence. It similarly uses phospholipids as the encapsulating shell together with other water-soluble structural agents, buffers and salts (Quaia 2005). Like the other two approved agents, Imagent was approved by the FDA in 2003 and is indicated only for echocardiography.

Although not approved for sale in the United States, SonoVue (BR-1; Bracco Imaging, Amsterdam, the Netherlands) is also a second-generation contrast agent approved for use in Europe, Canada and Asia. SonoVue uses SF_6 as the stabilizing gas surrounded by a flexible phospholipid shell. The uniformity of the microbubble diameter improves its backscattering and harmonic behavior at low acoustic power insonation (Gorce, Arditi et al. 2000; Quaia 2005). SonoVue was originally approved by the European Union medical agency in March 2001 for a broad range of indications, including echocardiography, vascular Doppler enhancement and assessment of vascularity of focal lesions in liver and breast (Greis 2008). However, it was later issued a warning statement that extra caution should be exercised in patients with conditions such as severe hypotension, cardiac arrest and myocardial infarction (Miller, Averkiou et al. 2008). Currently, SonoVue is under clinical trials in the United States for contrast-enhanced ultrasound imaging of multiple organs, including focal liver and breast lesion characterizations (Greis 2008).

Another similar agent that is still under clinical trials in Europe and the United States is Sonazoid (NC100100; GE Amersham, Oslo, Norway). Sonazoid consists of lipid-coated microspheres that are stabilized with perfluorobutane gas. Similar to SonoVue, it also has a well-defined size distribution with a volume-weight median diameter of approximately 3 μm (Quaia 2005; Sontum 2008). Japan is the first country that approved Sonazoid injections for contrast enhanced diagnosis of hepatic tumor. In addition, Sonazoid is currently being tested for myocardial perfusion imaging. Preclinical data revealed that Sonazoid was almost exclusively internalized by Kupffer cells during late phase after injection, suggesting a potential liver-specific entrapment strategy for targeted ultrasound imaging (Quaia 2005).

The second generation contrast agents combined two principle ways of increasing microbubble stability and persistence in the peripheral circle: external encapsulation with surfactants and selection of gases with low solubility and diffusion coefficient. A third generation of contrast agents is currently being developed to engineer the microbubble shell to impart unique functional features to these contrast materials. Currently, several agents have already reached to their late stages of the initial preclinical testing, once again signaling an exciting advancement of the development of modern ultrasound contrast agents.

BR-14 (Bracco Research SA, Geneva Switzerland) is a phospholipid-stabilized third-generation contrast agent that uses perfluorobutane gas to produce persistent contrast enhancement of tissue perfusion even at low power insonation (Quaia 2005). Initial experiments attributed this prolonged persistence to the transient microbubble retention within the capillaries (Fisher, Christiansen et al. 2002), and an early phase I study showed promising results for safety and efficacy in assessment of liver and kidney perfusion (Basilico, Blomley et al. 2002).

CARDIOsphere (PB-127; Point Biomedical Corp., San Carlos, CA) is composed of a bilayer shell made up of polylactide polymer and human albumin (Miller, Averkiou et al. 2008). The polylactide inner layer is a biodegradable polymer that governs the acoustic behavior of the microbubble, while the albumin outer layer ensures the biocompatibility of the agent. The microspheres are filled with nitrogen gas and are designed to collapse under very specific ultrasound conditions. Once destroyed, the nitrogen gas quickly dissolves into the surrounding blood, and this rapid loss of gas produces an intense signal that can be detected using low power imaging techniques (Leong-Poi, Song et al. 2002).

Microbubbles with targeting ligands attached to the surface also belong to the third generation of contrast agents that are currently being developed for diagnostic imaging applications. Adhesion molecules are added to the contrast agent shell so that the microbubbles will adhere to a specific region expressing biomarkers along the vascular endothelium. Targeting ligands, such as monoclonal antibodies, peptides and polysaccharides, can be incorporated into the shell of the microbubbles to provide selective adhesion to the biomarkers expressed on the endothelium (Borden, Qin et al. 2010). After injection into the bloodstream, the contrast agents accumulate via adhesion receptors at the targeting site, providing echo-enhancement for detection. Research in targeted ultrasound contrast imaging has evaluated many molecular biomarkers associated with intravascular pathology, including tumor angiogenesis, thrombosis and inflammation (Lanza and Wickline 2001; Borden, Qin et al. 2010). A detailed introduction to targeted ultrasound molecular imaging is provided in Section 1.4. To date, although several research groups have produced initial results, no human clinical studies have been performed.

1.2. Physicochemical Properties of Microbubbles

1.2.1. Microbubble Fabrication

Various methods have been developed to generate microbubbles for ultrasound imaging. The most popular method has been emulsification by entrainment of a gaseous core into the aqueous phase by mechanical agitation at the gas-liquid interface (Borden, Qin et al. 2010). Both shaking (amalgamation) and sonication techniques fall into this category. These techniques can produce microbubble suspensions rapidly (on the order of tens of seconds) with relatively high concentration and a polydisperse size distribution, ranging between sub-micrometers to tens of micrometers in diameter.

The acoustic behavior of contrast agents is strongly affected by their size (Gorce, Arditi et al. 2000; Sirsi, Feshitan et al. 2010; Streeter, Gessner et al. 2010). For both diagnostic imaging and therapeutic applications, a high degree of control over the size and uniformity of the microbubble suspensions is required in order to achieve the highest level of contrast enhancement, to ensure accurate dosing of a given drug and to maximize delivery efficiency. Moreover, as more advanced imaging techniques are developed, which exploit the complex nonlinear features of the microbubble signals in order to enable quantification of tissue perfusion and molecular biomarker expression, the ability to predetermine the acoustic response of a microbubble suspension is becoming increasingly important (Stride and Edirisinghe 2009). Consequently, a number of new methods have been developed to improve the control over microbubble size and other characteristics.

One way to control microbubble size is to size fractionate a pre-formed microbubble suspension using flotation (Kvale, Jakobsen et al. 1996). This separation method takes

advantage of the buoyant nature of the microbubbles. More recently, following the same governing principles, Feshitan et al. developed a size fractionation technique using differential centrifugation to rapidly select microbubble subpopulations based on size (Feshitan, Chen et al. 2009). Figure 1.2 compares the images of initial polydisperse and final size-isolated microbubbles using differential centrifugation technique in both bright field and epi-fluorescence mode. While size fractionation methods require additional steps after microbubble generation to reduce the polydispersity of the samples, the method is relatively straightforward and results in high microbubble yields. Other more sophisticated techniques have been developed to produce monodisperse microbubbles, including flow focusing (Talu, Hettiarachchi et al. 2008), T-junction (Xu, Nie et al. 2005), ink-jet printing (Bohmer, Schroeders et al. 2006) and coaxial electrohydrodynamic atomization (CEHDA) (Stride and Edirisinghe 2008). These techniques mainly utilize microfluidic processing methods to generate microbubbles with narrow size distributions. However, they require more complicated equipment setup in comparison to the sonication method and have much lower microbubble production rate in terms of processing time.

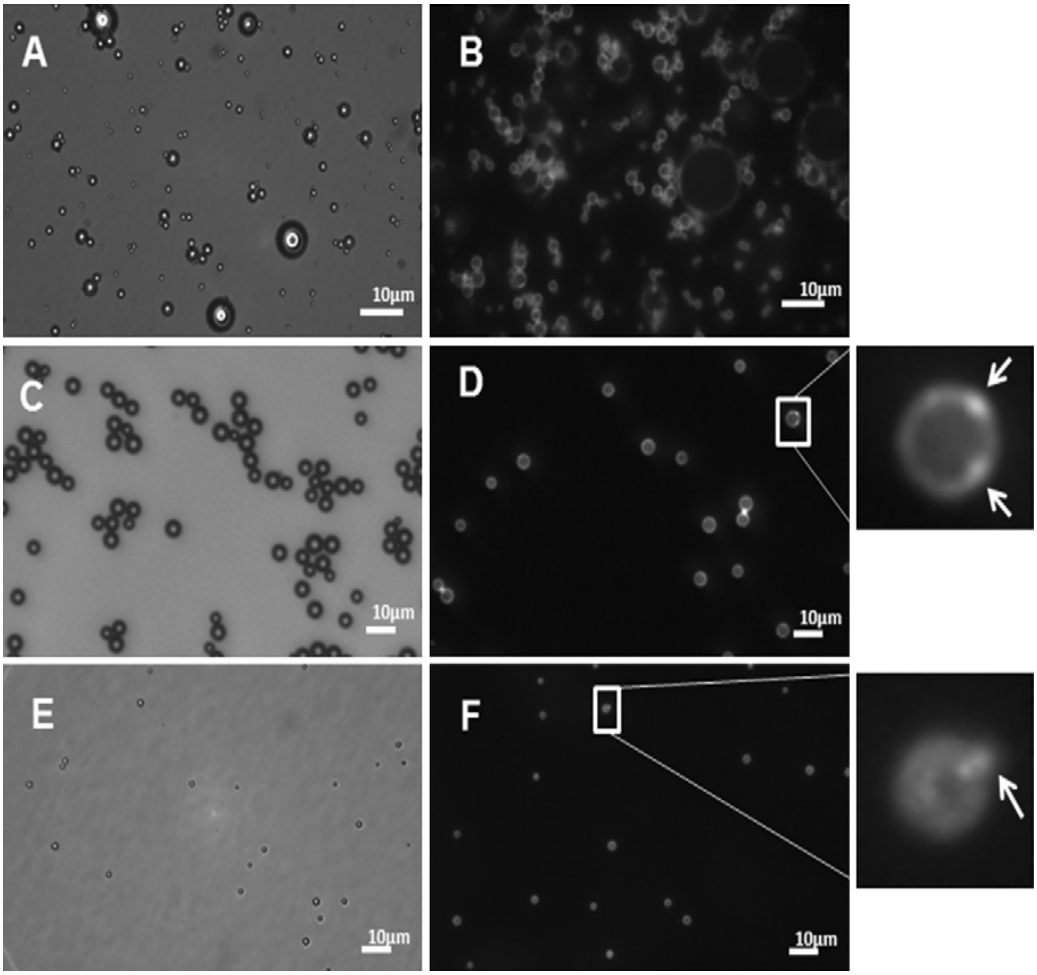

Figure 1.2. Microscopy images of initial polydisperse and final size-isolated microbubbles using the differential centrifugation technique in both bright field (left) and epi-fluorescence (right) mode. Freshly made microbubble suspensions are highly polydisperse (A, B). Size isolation allows rapid selection of microbubble subpopulations based on their diameters (4-5 µm C, D and 1-2 µm E, F). Taken from Feshitan et al. (Feshitan, Chen et al. 2009).

There are many ligand attachment strategies to conjugate targeting molecules to the monolayer shell of the microbubbles (Klibanov 2005; Klibanov 2009). However, all strategies may be grouped in two major approaches: pre- and post-labeling. The formal approach referred to as pre-labeling involves coupling the targeting ligand to the shell-forming molecule, typically

lipid molecules, in a separate procedure. This strategy offers the ability to fully control the synthesis and purification of targeted microbubbles in a step-by-step manner, ensuring high product yield and purity. The latter approach, referred to as post-labeling, requires the incorporation of functionalized lipids into the microbubble shell, and the targeting ligands are conjugated to the monolayer surface through either covalent bonds or non-covalent interactions after the microbubbles have been formed. This technique increases the efficiency of attaching targeting ligands, since not all lipid molecules in the original liposomal mixture are incorporated into the microbubble shells. This is particularly true for size-selected microbubbles using the differential centrifugation method (Feshitan, Chen et al. 2009). Instead of having a ligand attached to all lipid molecules, one can calculate the amount of ligand needed for conjugation based on the microbubble concentration, the size distribution, and the area fraction of functionalized lipids of the microbubble suspension, thereby reducing the cost of synthesis. Post-labeling also increases versatility by allowing multiple ligands to be conjugated to the same microbubble batch. This platform strategy for targeted contrast agent production is expected to increase safety, economy, and ease-of-use, when compared to pre-labeling.

1.2.2. Microbubble Monolayer Shell Properties

1.2.2.1. Surface Architectures

Microbubble shells are typically composed of two major components: an amphiphilic phospholipid species and a poly(ethylene glycol) (PEG) derivatized emulsifier (Figure 1.3). The surface architecture refers to the internal structure of the PEG brush layer on the microbubble shell, which depends on both lipid composition and shell microstructure (Borden, Qin et al.

2010). The incorporation of the PEGylated lipid into the shell enhances microbubble stability, and this stabilizing effect depends on the amount of PEG chains and their confirmations on the surface (Needham, Zhelev et al. 1999). Similar to the design of long-circulation liposomes, it is commonly believed that the brush layer of PEG chains can form a steric barrier against coalescence and adsorption of macromolecules to the microbubble surface (Klibanov, Maruyama et al. 1990; Klibanov 1999). This protective role of PEG is assumed to be due to the steric hindrance effect of the polymer brush; each PEG chain forms an impermeable "cloud" over part of the microbubble surface, which inhibits other molecules from diffusing into the brush layer (Torchilin, Papisov et al. 1995; Needham, Zhelev et al. 1999). Needham et al. (Needham, Zhelev et al. 1999) showed that small PEG mushrooms could retard the binding of fluorescently labeled avidin to biotinylated liposomes. As the PEG concentration increased, the overall vesicle fluorescence intensity decreased, indicating that the binding of avidin was retarded or even completely prevented due to the presence of PEG. Kuhl et al. (Kuhl, Leckband et al. 1995) also showed using a surface force apparatus (SFA) that the dominant force that stabilized liposomes with short polymer chains grafted on the surface was steric repulsion. Repulsive thermal fluctuation forces swamped short-ranged van der Waals attraction and longer-range electrostatic interactions, and provided a physical barrier around the bilayer to prevent close approach of other surfaces, improving liposome *in vivo* circulation persistence through reduction in opsonization and vesicle aggregation.

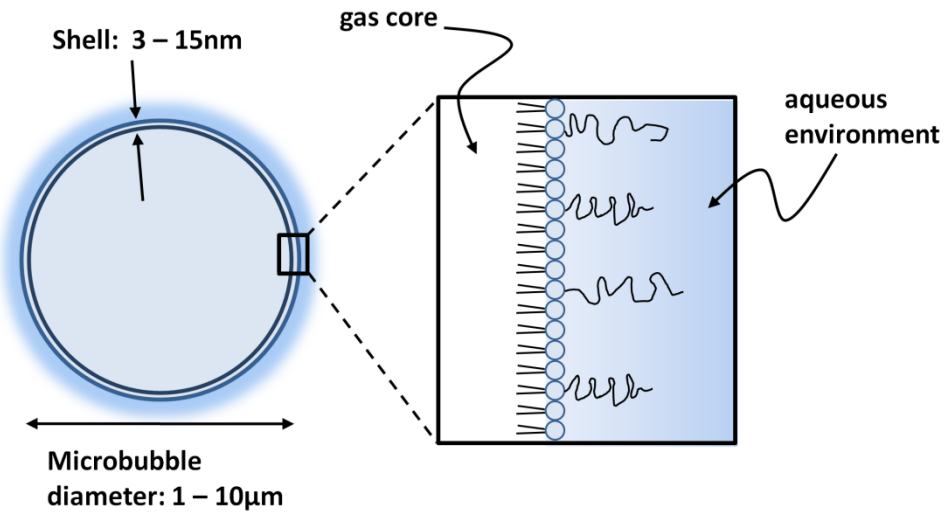

Figure 1.3. Cartoon illustrating the PEG polymer brush on the lipid monolayer shell of a microbubble.

For targeted contrast agents, the targeting ligands are normally attached to the distal end of the PEG chains, where the polymer can be extended beyond the average brush layer height to allow the ligand to efficiently bind to its target. However, targeting ligands typically present chemical groups (e.g., nucleophiles such as hydroxyl groups) that could trigger immune activation and decrease microbubble circulation persistence. Thus, a useful structure may be a bimodal mixture of grafted PEG chains: a fraction of shorter PEGs bearing targeting ligands and a fraction of longer PEGs without ligands to minimize undesired immune complement activation and nonspecific adhesion (Borden, Sarantos et al. 2006; Borden, Zhang et al. 2008).

1.2.2.2. Tethered Ligand-Receptor Interactions in a Bimodal Polymer Brush Layer

The structure and molecular interactions of bimodal polymer mixtures have been widely studied both theoretically (Birshtein, Liatskaya et al. 1990; Lai and Zhulina 1992; Dan and Tirrell 1993; Chen and Dormidontova 2005; Longo, Thompson et al. 2008) and experimentally (Dhoot, Watanabe et al. 1994; Levicky, Koneripalli et al. 1998; Goedel, Luap et al. 1999; Kim, Klibanov et al. 2000; Moore and Kuhl 2006; Kuhlman, Taniguchi et al. 2007). Using a numerical self-consistent field model, Dan and Tirrell (Dan and Tirrell 1993) showed that vertical segregation between the segments of the shorter and longer polymer chains occurred irrespective of the molecular weight differences or composition in a bimodal polymer brush layer. When two bimodal polymer surfaces were compressed, this stratification persisted. Lai and Zhulina (Lai and Zhulina 1992) used Monte Carlo simulations to further confirm the segregation of the free ends of longer and shorter chains. They also showed that the structural properties of the shorter chains depended very little on the lengths of the longer chains when both were highly stretched.

Experimentally, Kim et al. (Kim, Klibanov et al. 2000) showed in a force microscopy experiment that adhesion to avidin-coated glass beads failed when biotin ligands were tethered to short PEG chains buried in a longer PEG overbrush. In addition, they showed proof that the presence of a spacer moiety could improve the effective interaction range of a ligand past the steric barrier created by PEG chains into a partially obscured binding site, supporting a similar finding made by Wong et al. (Wong, Kuhl et al. 1997) using bilayer surfaces. Borden et al. reported similar results, in which specific adhesion of microbubbles with a bimodal polymer brush was partially prevented in hydrodynamic conditions in comparison to microbubbles with a monodisperse polymer brush layer (Borden, Sarantos et al. 2006). These results indicated that

ligand accessibility could be reduced when targeting ligands are attached to the shorter PEGs in a bimodal mixture of PEG chains, therefore reducing undesired potential immune response and nonspecific adhesion.

1.3. Microbubbles as Ultrasound Contrast Agents

1.3.1. Acoustic Behavior of Microbubbles

1.3.1.1. Microbubble Scattering and Resonance

The high echogenicity of microbubbles comes from their compressible gas core. It has low density and high compressibility, allowing it to expand and contract in response to the application of an ultrasound field (Borden and Dayton 2008). As a result, microbubbles undergo volumetric oscillation (pulsation) (Figure 1.4) and consequently scatter much more energy than solid or liquid spheres of the same size (Stride and Saffari 2003). Fortuitously, the resonance frequency of a microbubble able to pass through human capillaries (<7 μm) lies within the acoustic bandwidth of typical diagnostic scanners (1-10 MHz), meaning that the amplitude of microbubble oscillations (and hence the scattering effect) is thus maximized (Stride and Saffari 2003; Borden and Dayton 2008; Borden, Qin et al. 2010). A resonant microbubble is a thousand times more echogenic than a non-resonant microbubble of the same diameter (Calliada, Campani et al. 1998). Due to this high degree of backscatter in comparison to blood and surrounding tissues, Klibanov et al. demonstrated that it was possible to detect individual microbubbles (~0.004 pL gas volume) with a clinical ultrasound system (Klibanov, Rasche et al. 2004).

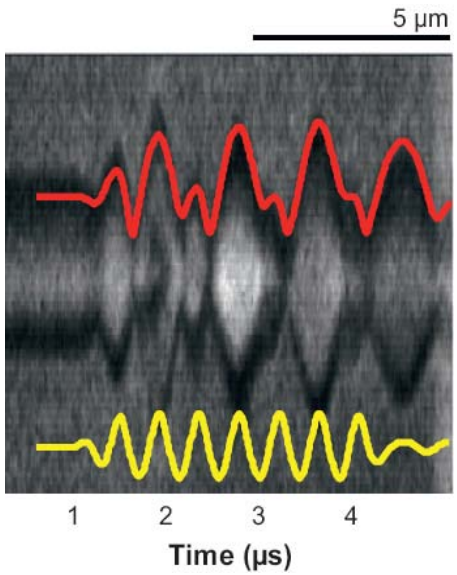

Figure 1.4. Radius-time streak image of a microbubble oscillating in response to an acoustic pressure field. The transmitted pulse is shown in yellow, and the predicted microbubble radius-time curve is shown in red. Taken from Ferrara et al. (Ferrara, Pollard et al. 2007).

A unique aspect of microbubble acoustic behavior is that they expand to a greater degree than they can be compressed (McCulloch, Gresser et al. 2000; de Jong, Emmer et al. 2009). Depending on the peak negative pressure (PNP) of the incident ultrasound beam, the scattering behavior of microbubbles may be linear or nonlinear (de Jong, Emmer et al. 2009). For low acoustic pressure exposure, the instantaneous radius of a microbubble oscillates linearly in relation to the amplitude of the applied external ultrasound pressure field. As the pressure is increased, the pulsation of the microbubbles starts to show nonlinear characteristics, returning echoes not only at the fundamental frequency but also at multiples of the resonance frequency (i.e. harmonics). As the pressure if further increased, microbubble destruction can occur, resulting in the release of the encapsulated gas into the immediate environment. While tissues can also produce echoes that are rich in harmonic frequencies, substantial differences in the

pressures and frequencies associated with harmonic spectra allow microbubble and tissue echoes to be differentiated. The resulting "harmonic imaging" improves the signal-to-noise ratio, optimizing visualization of the contrast agent population (McCulloch, Gresser et al. 2000).

1.3.1.2. Microbubble Attenuation

In the case of dilute microbubble suspensions, the power of the backscattered signal is proportional to the contrast agent concentration (de Jong, Hoff et al. 1992). Therefore, a local increase in blood volume is reflected by an increase in contrast agent concentration, which can be quantified by measuring the increase of backscattered power (Stapleton 2007). However, above a certain concentration threshold, microbubble attenuation becomes significant, and the backscattered power will no longer increase linearly with concentration (de Jong, Hoff et al. 1992). It becomes difficult, therefore, to perform quantitative contrast flow measurements at high microbubble concentrations. A clear indication of microbubble attenuation is the shadowing effect observed during imaging, in which the underlying structure is obscured after a high concentration microbubble injection (Figure 1.5).

Microbubble attenuation is due to viscous, thermal and radiation damping effects as the microbubbles oscillate (Stapleton 2007). The total attenuation as ultrasound passes through a bubbly medium is the sum of absorption and scattering. For microbubbles oscillating below their resonant frequencies, attenuation is dominated by absorption; while for microbubbles driven above their resonance, attenuation is dominated by scattering (Stapleton 2007).

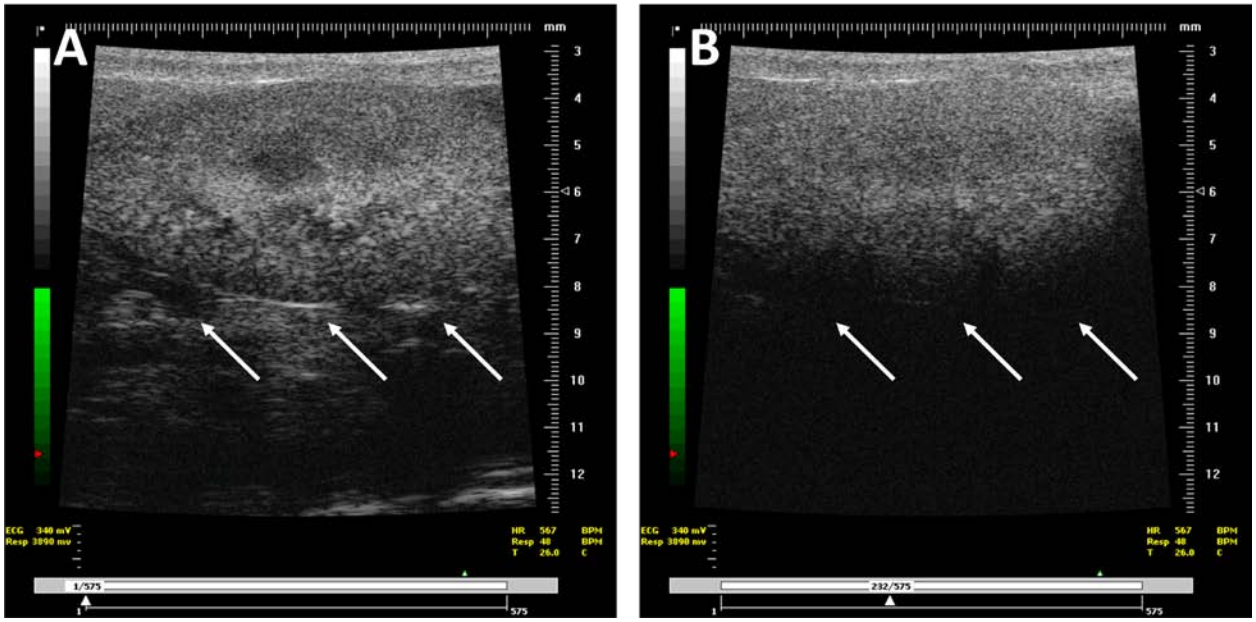

Figure 1.5. Illustration of the shadowing effect caused by microbubble attenuation. (A) Prior to the administration of microbubbles, the underlying structure below the mouse kidney was visible (arrows). (B) A 100 µL bolus injection of 4-5 µm size-isolated microbubble samples was made. Significant shadowing was observed in the mouse kidney as a result of microbubble attenuation. The underlying structure under the kidney was completely obscured. Courtesy of Dr. Shashank Sirsi.

1.3.1.3. Effect of Ultrasound Radiation Force on Microbubbles

When a traveling ultrasound wave is absorbed by a particle, the momentum associated with the wave produces a net primary radiation force in the direction of the ultrasound wave propagation (Nyborg 2006). For compressible objects, such as microbubbles driven at their resonant frequency, they experience far larger radiation forces than their incompressible counterparts. Dayton et al. (Dayton, Allen et al. 2002) showed that using low-amplitude resonant frequency ultrasound pulses of many cycles, microbubbles could be physically pushed

over distances on the order of millimeters. Therefore, it is possible to force contrast agents circulating in the blood pool into contact with targeting sites on the endothelium under a specific ultrasound field. Assuming that the great majority of microbubbles and targets will reside in the capillaries, it may be sufficient to displace the contrast agents only a few microns in order to facilitate binding (Zhao, Borden et al. 2004). In addition, using intravital microscopy, Dayton et al. (Dayton, Klibanov et al. 1999) demonstrated that microbubbles traveled at a reduced velocity when concentrated near the vessel wall in comparison to those in the center of the flow system, allowing more contract time for ligand-receptor bond formation.

For ultrasound contrast agents, the effect of the radiation force is maximized when microbubbles are driven at their resonance frequencies. For a typical microbubble that can pass through microvasculature freely without being trapped and cause embolism, its resonance frequency lies within 1-10 MHz. However, for small animal imaging, high frequency is normally desired to achieve higher spatial and temporal resolution. Therefore, there is a great need to develop an imaging transducer that can offer dual-frequencies for improved small animal imaging: one at low MHz range to physically manipulate the microbubbles by pushing them against the endothelium and one at high MHz range for contrast enhanced imaging.

In addition to the primary radiation force, secondary radiation force has been reported to affect microbubble populations as well. When two neighboring microbubbles oscillate in an ultrasound field, both of these vibrating gas bodies generate additional sound fields of the same frequency, and each of them serves as both source and receptor of an attractive secondary radiation force (Nyborg 2006). Photographic evidence of bubble clustering as a result of secondary radiation forces has been reported as early as 1975 by Crum (Crum 1975). More recently, Dayton et al. (Dayton, Morgan et al. 1997; Dayton, Allen et al. 2002) confirmed the

occurrence of clustering and found good agreement between the predicted and measured speeds of approach of neighboring microbubbles. Interestingly, the clusters were found to be resistant to separation during insonification even at low pressures. But they dispersed as soon as transmission was stopped. Thus, the effects of secondary radiation forces were only found to be significant at high pulse repetition frequencies (Stride and Saffari 2003).

For a low-amplitude resonant frequency pulse that is currently used for clinical ultrasound imaging, the oscillation of the microbubbles could expose the targeting ligands on the surface of BLA microbubbles to initiate site-specific binding. However, current clinical ultrasound systems are not yet designed to produce the necessary pulse sequences to utilize radiation force enhanced targeting. There are still great needs to design a new generation of ultrasound transducers with optimized acoustic parameters to selectively activate stealth microbubbles and to enhance their targeting abilities for molecular imaging.

1.3.2. Safety

The safety of diagnostic microbubbles is a complex issue because not only must their safety as drugs be studied, but additionally, the effects of sonication also need to be taken into consideration (Cosgrove and Harvey 2009). The constituents of microbubble contrast agents, including the shell materials and the core gas, are carefully chosen to their biological inertness and have passed numerous stringent safety tests. The acoustic power needed during contrast-enhanced ultrasound is well characterized using mechanical index (MI) to guide the clinical usage of microbubbles, in order to minimize any potential bioeffects due to the interaction of ultrasound waves with the gas bodies, such as inertial cavitation. A detailed introduction to

potential microbubble immunogenicity is provided in Section 1.3.3. In this section, the results from several multicenter studies regarding the safety of contrast agents in clinical settings are reviewed.

A multicenter Italian study retrospectively checked the records of 23,000 patients who had been studied for liver lesions using contrast-enhanced ultrasound and found only 29 adverse events, of which two were severe enough to require treatment (Cosgrove and Harvey 2009). The adverse event rate was only 0.0086%, and no deaths were reported. The adverse events were hypotensive reactions occurring within 2 min after injection, and were treated successfully by standard resuscitation techniques. A more recent American retrospective study compared over 4,300,000 patient records for acute mortality (death occurring within 24 hr after injection) showed that no increase in acute mortality resulted due to the injection of contrast agents (Main, Ryan et al. 2008). No statistical significance ($P = 0.61$) was detected between patients who underwent non-contrast echocardiography studies (24-hr mortality rate = 1.08% with $n = 45,789$ deaths) and patients who underwent contrast-enhanced studies (24-hr mortality rate = 1.06% with $n = 616$ deaths). These findings suggested that the deaths related to contrast-enhanced ultrasound simply resulted from “pseudo complication”, the progression of the underlying disease (Main, Ryan et al. 2008). In light of these large scale clinical safety studies, the FDA relaxed the restrictions and warnings on the use of contrast agents in 2008. However, the basic safety principles of weighing the possible risks against the potential benefits for contrast agent injection should still be practiced for each patient. Nevertheless, physicians using or controlling the use of microbubble contrast agents must be familiar with standard resuscitation techniques and have the appropriate monitoring and rescue apparatus to hand (Cosgrove and Harvey 2009).

There is numerous compelling evidence of the efficacy of microbubble contrast agents to support the notion of their usage for diagnostic ultrasound imaging. However, microbubbles are currently only approved in the United States for cardiology imaging (Wilson, Greenbaum et al. 2009). The major concern involved in the clinical approval of microbubbles used for noncardiac imaging is the potential anaphylaxis reaction to these agents. The current project is to address this very issue by engineering a stealth microbubble design in the attempt to minimize their potential immunogenicity while keeping other targeting properties for molecular imaging applications.

1.3.3. Microbubble Immunogenicity

1.3.3.1. Introduction to the Complement Immune System

The complement system, consisting of over 30 soluble plasma and cell-surface bound proteins, is an important effector arm of both innate and adapted immunity (Murphy, Travers et al. 2008). There are three pathways to activate the complement system: the classical pathway, the lectin pathway and the alternative pathway. The classical pathway is triggered by the binding of complement component C1q to immune-complexes on the antigen surfaces; the lectin pathway is triggered by the binding of mannose-binding lectin to arrays of carbohydrates on foreign microorganisms; and the alternative pathway is triggered by the binding of spontaneously activated complement component C3 in plasma to the surface of foreign particles. All three pathways converge to the formation of C3 convertases, which cleave C3 into C3b and C3a for further opsonization and mediation of inflammation in the complement cascade. Figure 1.6

shows the crystal structure of complement component C3 obtained using x-ray diffraction with the location of its surface active thioester bond pointed out.

There are also three ways in which the complement system initiates subsequent responses once it is activated. First, it generates a large number of activated complement proteins that bind covalently to pathogens, opsonizing them for engulfment by phagocytes (i.e., priming). Second, the small fragments of some complement proteins act as chemoattractants and anaphylatoxins (e.g., C3a) to recruit more phagocytes to the site of complement activation, and also to activate these phagocytes. Third, the final components in the complement pathway form the membrane attack complex to create pores in the pathogen membrane.

One key site for the activation of the complement system is the surface of foreign particles (Murphy, Travers et al. 2008). Regardless of the activation pathway, the main effectors of the complement system (such as C3 convertases and C3b) need to bind to the surface of the particle in order to initiate the phagocytic process. Therefore, the accessibility of the complement component proteins to the foreign particle surface, or rather to the specific recognition sites on the surface, is important in determining complement activation.

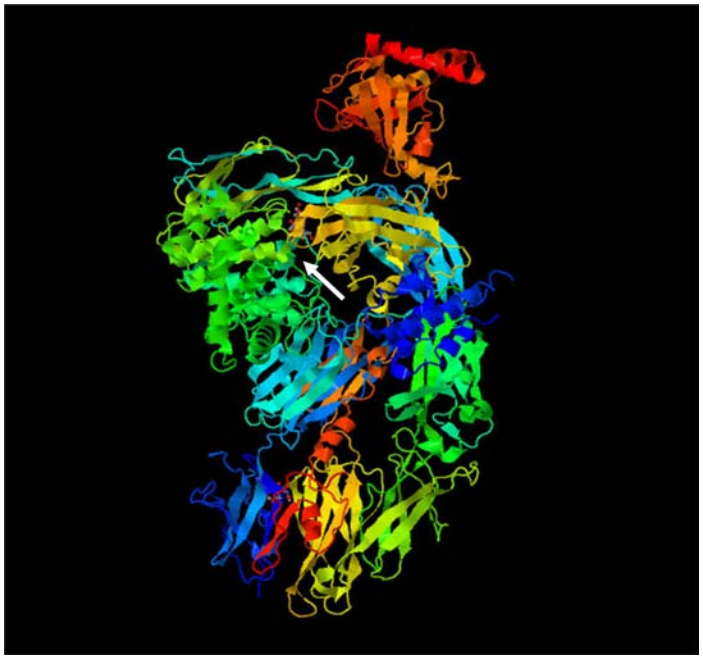

Figure 1.6. Crystal structure of complement component C3 with the location of its surface active thioester bond pointed out by arrow. Adapted from Janssen et al. (Janssen, Huizinga et al. 2005).

1.3.3.2. Microbubble Immunogenicity

When administered intravenously, microbubbles or other conventional colloidal particles are rapidly removed from the bloodstream by the mononuclear phagocyte system (MPS) (Mosqueira, Legrand et al. 2001). Previous studies have shown that the biodistribution of microbubbles was substantially different as compared to free lipids or liposomes (Tartis, Kruse et al. 2008). They are mainly retained by the liver, spleen and lungs (not the kidneys) shortly after injection, and this rapid uptake is attributed to the Kupffer cells and macrophages of the MPS (Walday, Ostensen et al. 1994; Walday, Tolleshaug et al. 1994; Perkins, Frier et al. 1997; Willmann, Cheng et al. 2008).

Walday et al. (Walday, Tolleshaug et al. 1994) studied the biodistribution of radiolabeled Albunex in both rats and pigs up to 90 min after intravenous administration and found that about 60% of the albumin microspheres were recovered in the liver, 9% of them were recovered in the spleen, and 5% of them were recovered in the lungs 3 min after injection in rats. In contrast, in pigs, more than 90% of the microbubbles were recovered in the lungs, and this was explained by the presence of intravascular macrophages in the porcine lungs (Walday, Tolleshaug et al. 1994). Using commercially available targeted microbubbles, MicroMarker (Bracco Research; Geneva, Switzerland), labeled with radioactive antibodies specific to VEGFR2, Willmann et al. (Willmann, Cheng et al. 2008) showed similar results that rapid accumulation in both liver and spleen were detected using tumor mice models. He also showed that a small amount of targeted microbubbles were accumulated in the mouse kidneys, which could be due to VEGFR2 expression in normal renal tissue rather than non-specific adhesion.

The MPS protects the systemic circulation by distinguishing foreign and endogenous substances, and the fast clearance of foreign particles is mediated through endocytosis with recognition of specific cell surface receptors, such as complement receptor 1 (CR1) and Fc receptor (Harashima, Sakata et al. 1994; Murphy, Travers et al. 2008). Endocytosis is classified into three categories: receptor-mediated endocytosis (RME), pinocytosis and phagocytosis (Lodish, Berk et al. 2008). Depending on the size of the particle, it can be eliminated from the system either through RME and/or pinocytosis (for small compounds) or phagocytosis (for large particles such as microbubbles). Evidence of microbubble phagocytosis has been demonstrated both *in vitro* (Yanagisawa, Moriyasu et al. 2007) and *in vivo* (Quaia, Blomley et al. 2002; Lim, Patel et al. 2004). Although not required, phagocytosis is often triggered by specific receptor recognition, and such ligand-receptor interactions typically exist between the cellular receptor

specific for the proteins bound to the colloidal particles rather than for the particles themselves. Thus, serum protein adsorption is extremely important in determining particle uptake by phagocytes and predicting the fate of colloidal particles after administration. Immunoglobulin G (IgG) and complement components are known as major opsonins for the uptake of large particles, such as bacteria, viruses, and remnants of dead cells. In particular, complement activation plays a critical role in the recognition of microbubbles by the immune system (Szebeni 2005).

For targeted contrast agents, the targeting ligands conjugated to the surface typically present nucleophilic groups (e.g., hydroxyl and amino) that could trigger the alternative pathway of the complement activation cascade and decrease microbubble circulation persistence. Clinical reports have shown data indicating that long circulating PEGylated liposomes, with similar surface structures to microbubbles, could trigger acute hypersensitivity reaction in sensitive individuals (Szebeni 2005; Szebeni 2005). These reactions are classified as complement activation-related pseudoallergy (CARPA) due to their common trigger mechanism: complement activation (Szebeni 2005; Moghimi, Andersen et al. 2010). Despite the common belief that water-soluble PEG chains on the surface of Stealth liposomes can prevent immune recognition by reducing protein adsorption and vesicle aggregation, recent studies have suggested that PEGylated liposomes are capable of triggering the complement system in human serum and fixing opsonic complement proteins (Moghimi and Szebeni 2003; Szebeni 2005; Moghimi, Hamad et al. 2006; Moghimi and Hamad 2008). It was reported that complement activation was detectable as quickly as 10 min after injection of the marketed liposomal drug Doxil (Centocor Ortho Biotech Inc.; Horsham, PA) (Szebeni 2005), which is on the same time scale as microbubble persistence *in vivo*. The reason behind the long circulation of PEGylated liposomes while they are associated with complement activation is still not fully understood. One

hypothesis is that the surface grafted PEG chains inhibit the accessibility of complement surface fixation and thus prevent the ligation to complement receptors (Borden, Qin et al. 2010). Therefore, it is important to design targeted microbubbles with a surface architecture that minimizes complement recognition by minimizing C3/C3b fixation, in order to reduce CARPA and prevent premature microbubble clearance from the circulatory system. At the same time, avoidance of complement fixation can keep the ligand pristine and, therefore, allow it to retain specificity to the target receptor.

1.4. Targeted Ultrasound Molecular Imaging

1.4.1. Introduction to Targeted Ultrasound Molecular Imaging

Molecular imaging is an emerging field that aims to visualize, characterize and measure biological processes at the molecular and cellular levels in humans and other living systems. This new discipline seeks to represent the individual molecular events in order to understand the molecular basis of the disease and to develop drugs directed at those molecular targets (Mancini, Greco et al. 2009). Targeted ultrasound molecular imaging utilizes contrast-enhanced ultrasound with labeled microbubbles that are engineered specifically to target molecular biomarkers that are associated with intravascular diseases (Figure 1.7). Furthermore, microbubbles could carry therapeutic drugs that can be released to the targeted sites upon injection. Therefore, targeted ultrasound molecular imaging may provide potential therapeutic implications over other traditional imaging modalities.

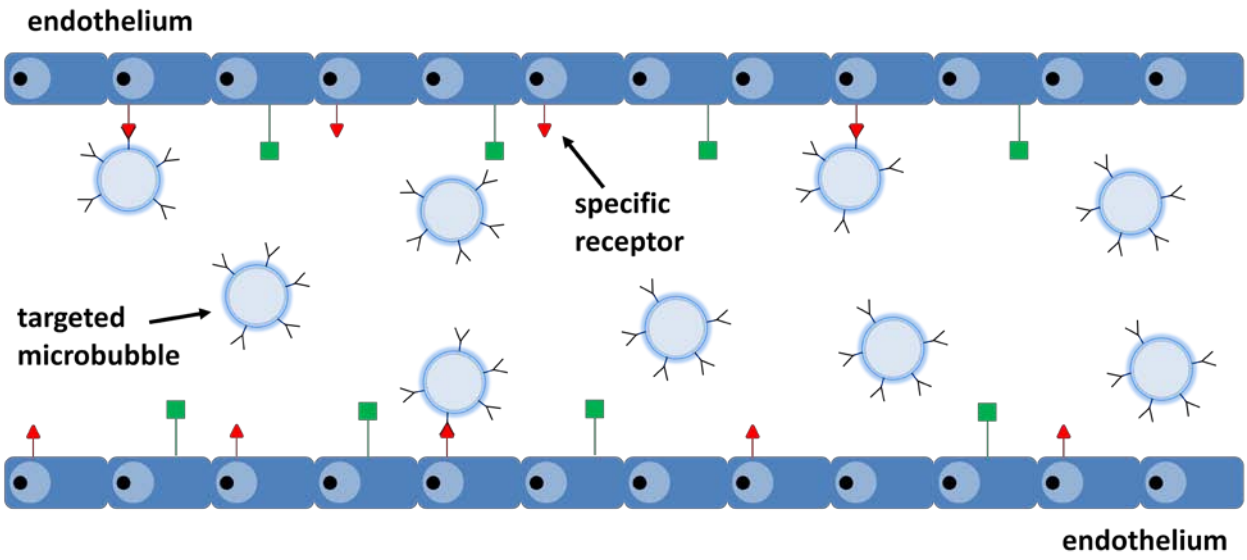

Figure 1.7. Cartoon illustrating targeted microbubbles binding to specific biomarkers along the endothelium during circulation for molecular imaging applications.

There are two major approaches to promote targeting of microbubbles to a specific region of interest *in vivo*: passive targeting and active targeting (Mancini, Greco et al. 2009). The former approach takes advantage of inherent chemical or electrostatic properties of the microbubble shell, leading to the adhesion of microbubbles along the endothelium. This method relies on the non-specific binding between microbubbles and endothelial receptors that are up-regulated due to disease. It allows for functional imaging of the pathophysiological condition that induces the over-expressed cell surface biomarkers, although it does not exhibit molecular specificity. The latter method, referred as "active targeting", takes advantage of the functionalized contrast agents with targeting ligands deliberately attached to the surface. The targeting ligand binds to specific receptors along the endothelium, resulting in the accumulation of targeted contrast agents to disease sites and allowing a quantitative measurement of the expression of these molecular biomarkers. Since the microbubbles remain within the vasculature

because of their micron size, specific marker molecules have to be located in the intravascular space. For instance, intercellular adhesion molecule-1 (ICAM-1) that is up-regulated during atherosclerosis can be used as targeted markers for ultrasound molecular imaging.

The protocol used for targeted ultrasound molecular imaging may be different from what is followed for regular ultrasound imaging procedures (Dayton and Borden 2008; Mancini, Greco et al. 2009) (Figure 1.8). After a bolus injection of targeted contrast agents, a 4-15 min dwell time is allowed before starting the contrast enhanced imaging. This wait time serves two purposes: first, it allows the retention of adhesive microbubbles at the target site; second, it allows for the clearance of freely circulating (non-adherent) contrast agents, which would otherwise interfere with the detection of the targeted agents. Microbubbles accumulated at the target site are imaged using a destruction-subtraction algorithm. Typically, a background image is recorded first, and a 2-3 sec breaking pulse with high mechanical index (MI) is then applied to remove all the bound microbubbles. An intermittent imaging at a pulsing interval of 10 sec is performed to derive the signal only from any remaining freely circulating microbubbles. The image acquired before the destruction pulse corresponds to the signal given from freely circulating as well as adherent microbubbles. The image acquired after the destruction pulse corresponds to the signal coming from circulating microbubbles returning to the region of interest. The second image is subtracted from the original one to obtain the signal given only from the retained microbubbles at the target site. The entire imaging procedure typically lasts about 30 min, then data analysis is performed offline (Mancini, Greco et al. 2009).

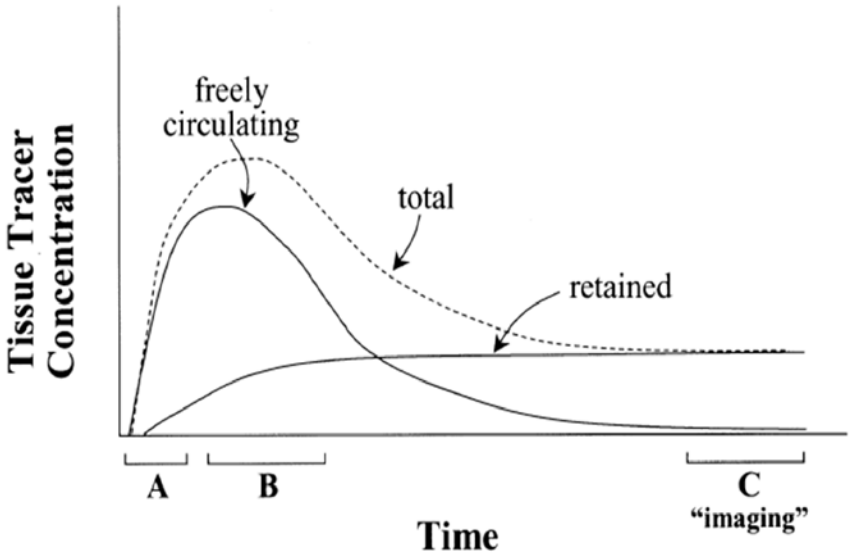

Figure 1.8. Commonly used imaging strategy for targeted contrast agent detection in molecular imaging. After a bolus injection, the total contrast signal in tissue rises rapidly and is largely attributed to the freely circulating microbubbles (A). The rate of targeted agent adhesion in diseased tissue is highest when the free contrast concentration is high (B). After a waiting period for clearance of freely circulating agents, remaining contrast in tissue is due to retention of targeted agents, and imaging of targeted microbubbles is performed. Taken from Lindner et al. (Lindner 2004).

Targeted ultrasound molecular imaging offers a powerful tool for physicians to study diseases at the molecular and cellular levels, allowing the establishment of a more accurate diagnosis, the monitoring of prognosis longitudinally and the tailoring of therapeutic treatments for individual patients. It allows diagnosis and evaluation of the response to a particular therapy by quantifying the change in the expression profile of endothelial biomarkers over time. In a clinical scenario, before a therapy (e.g., angiogenic inhibitor) is given, the patient would be sequentially administrated a panel of labeled microbubbles, which target a variety of known

biomarkers such as integrin $\alpha_v\beta_3$ (Willmann, Kimura et al. 2010), vascular endothelial growth factor receptor 2 (VEGFR2) (Willmann, Lutz et al. 2008) and Notch receptors (Wu, Cain-Hom et al. 2010). This provides a baseline expression for these molecules involved in tumor angiogenesis. When the patient returns after treatment, this same panel could be repeated to look for changes in the endothelial expression and regression of the tumor. Since tumor growth is a multiparametric and dynamic process, it is important to repeat this protocol throughout the patient's therapy at various time points in order to assess the progression of the disease and to adjust the treatment for more personalized medicine.

It is important to differentiate targeted molecular imaging from targeted drug delivery. Targeted drug delivery requires high specificity between the targeting vehicle and the targeted site in order to accurately deliver the therapeutic agent only to the diseased cells. The concept behind drug targeting is to increase the therapeutic index by increasing the potency of the drug by delivering a greater dose to the culprit cells and decreasing the toxic side effects by avoiding healthy cells. Targeted drug delivery is therefore extremely challenging. On the other hand, targeted molecular imaging has more relaxed restrictions for targeting specificity since it does not require the biomarkers to be expressed only in the targeting organ. There are fewer concerns for toxicity in targeted molecular imaging than in drug delivery because the contrast agent is not highly bioactive. Targeted molecular imaging is a method that gives physicians the tool to assess the expression of endothelial biomarkers in order to establish a more accurate diagnosis, to monitor the progression longitudinally and to tailor the treatment for individual patients. It does not offer a treatment of the disease, but rather a tool to assess and evaluate the efficacy of the treatment.

However, current technique still has its limitations and needs further advanced research from multiple disciplinarities for the utilization of targeted molecular imaging for clinical development. First, it requires improved knowledge of molecular biology to identify specific ligand-receptor pairs that can be used as biomarkers for particular diseases. This is especially important for the development of antiangiogenic therapies in oncology (Sessa, Guibal et al. 2008). Second, targeted ultrasound molecular imaging only offers insights to the endothelial expression of biomarkers. The relevancy of their expression to the response rate of a particular therapy needs to be pre-established in order to correctly assess the development of the diseases and to adjust the treatment for personalized therapy. Third, targeted ultrasound molecular imaging is limited to the vasculature. Because of the size of the contrast agents, they are confined to the blood pool and can only bind to receptors located in the intravascular space, on the luminal surface of vascular endothelium. Intracellular molecular imaging using targeted microbubbles is still hard to achieve although phagocytosed microbubble imaging has been reported by several groups (Walzog, Schuppan et al. 1995; Villanueva, Jankowski et al. 1997).

1.4.2. Applications for Targeted Microbubbles Used as Molecular Imaging Agents

1.4.2.1. Angiogenesis

Angiogenesis refers to the process of growing new vasculature from pre-existing blood vessels and/or circulating endothelial stem cells (Mancini, Greco et al. 2009; Deshpande, Pysz et al. 2010). It is a fundamental biological mechanism that is involved in many physiological processes, from wound repair and the female menstrual cycle to the growth and metastasis of solid tumors. Tumor-associated angiogenesis typically has two phases: an avascular and a

vascular phase that are separated by the “angiogenic switch” (Deshpande, Pysz et al. 2010). The avascular phase of tumors refers to small lesions that stay dormant for prolonged periods and subsist on diffusion of nutrients from the normal host vessels. These small avascular tumors can only grow several millimeters in size before their supply of nutrients becomes limited. At this point, a small subset of dormant tumors enter the vascular phase in which exponential tumor growth ensues by shifting the local equilibrium between negative and positive endogenous regulators of angiogenesis. The final result is the alignment and organization of endothelial cells to form new blood vessels and a vascular network within the tumor (Mancini, Greco et al. 2009; Deshpande, Pysz et al. 2010).

Since the shedding of large numbers of tumor cells from the primary tumor may not begin until the tumor has developed a sufficient network of blood vessels, angiogenesis may also be used to correlate with metastatic potential (Mancini, Greco et al. 2009). Advances in knowledge of tumor angiogenesis have resulted in the identification of several molecules involved in tumor angiogenesis signaling, including integrin $\alpha_v\beta_3$, vascular endothelial growth factor receptor 2 (VEGFR2), and notch receptor. These molecules have been exploited for their use as targets for molecular imaging and quantification of tumor angiogenesis at the molecular level. Several groups have shown that targeted microbubbles with monoclonal antibodies against vascular endothelial growth factor receptor 2 (VEGRF2) attached to the surface via a streptavidin-biotin linker resulted high ultrasound signal in tumor tissue in comparison to non-targeted control microbubbles (Lyshchik, Fleischer et al. 2007; Rychak, Graba et al. 2007; Lee, Lyshchik et al. 2008). Small peptide sequences are also being studied for their potential as targeting ligands for molecular imaging. Willmann et al. (Willmann, Kimura et al. 2010) showed that $\alpha_v\beta_3$ integrin-targeted microbubbles with surface-conjugated small knottin peptides

as the targeting ligand resulted in an imaging signal higher than that provided by large antibody labeled microbubbles. A new approach to increase microbubble-enhanced ultrasound imaging signal for detection of tumor angiogenesis was recently explored using dual-targeted microbubbles (Deshpande, Pysz et al. 2010). Both VEGRF2 and integrin $\alpha_v\beta_3$ targeted ligands were attached to the contrast agents for site specific imaging. Increased signal level was detected, and this could be used in cases such as the early detection of cancer when tumors are too small to cause detectable morphologic changes but large enough to induce tumor angiogenesis (Willmann, Lutz et al. 2008).

1.4.2.2. Inflammation

Most of the early development of targeted ultrasound contrast agents has focused on imaging inflammation because of its importance in tissue damage and organ dysfunction in many disease processes (Mancini, Greco et al. 2009). Inflammation is mediated by a variety of receptors that are exposed to the blood pool. These molecular biomarkers are well characterized and very specific for the regions of inflammation. Taking these technical factors into consideration, the detection of inflammation is ideal for targeted ultrasound molecular imaging.

Tissue inflammation is originally assessed through passive targeting using non-targeted microbubbles (Villanueva, Jankowski et al. 1997). These microbubbles bind to the activated leukocytes within the microcirculation of the inflamed tissue, and the binding is influenced by the composition of the microbubble shell: albumin microbubbles adhesion is mainly through the leukocyte β_2 integrin Mac-1; while lipid microbubbles adhesion is mainly through opsonization by serum complement (Lindner, Dayton et al. 2000). *In vitro* studies showed that microbubbles

were phagocytosed intact by activated leukocytes within minutes and remained acoustically active (Lindner, Dayton et al. 2000; Lindner 2009; Mancini, Greco et al. 2009). However, the ultrasound signal is relatively low because of the small portion of retained contrast agents and the viscoelastic damping of microbubbles once phagocytosed. In order to address this issue, targeting ligands are attached to the microbubbles to enhance the avidity of adhesion for activated leukocytes. This active targeting method is more suitable for the detection of mild or chronic inflammation using contrast enhanced ultrasound (Lindner 2009). Monoclonal antibodies can be attached to the microbubble surface to target selectins, ICAM-1 and vascular cell adhesion molecule-1 (VCAM-1) (Villanueva, Jankowski et al. 1998; Lindner, Song et al. 2001; Lindner 2009). Similar to molecular imaging of angiogenesis, the dual-targeting strategy is also utilized for inflammation imaging (Ferrante, Pickard et al. 2009). Under shear flow that was similar to physiological conditions, Ferrante et al. showed that dual-targeted microbubbles to P-selection and VCAM-1 adhered almost twice as efficiently as single-targeted microbubbles. This finding may be useful for the detection of early stage atherosclerosis plaques (Ferrante, Pickard et al. 2009).

1.5. Research Motivations and Specific Aims

Microbubbles are ubiquitous in nature, and they are important for many industrial processes. Over the past several decades, microbubbles have been developed for biomedical applications as ultrasound contrast agents. More recently, specific ligand molecules are attached to the surface of microbubbles in an attempt to combine targeted ultrasound with molecular imaging for the detection and monitoring of intravascular pathologies. In order to improve the

circulation persistence time and reduce microbubble-induced complement activation, different surface architectures of contrast agents have been proposed, including one with a bimodal PEG brush layer. Prior to this study, there was a need for a better understanding of ligand diffusion and conjugation in a bimodal polymer brush layer on the monolayer shell of the microbubbles. In addition, more experimental studies, both *in vitro* and *in vivo*, were needed in order to provide design principles for chemical engineering of the microbubble formulation and to show the suitability of this new design for potential clinical applications. To address these issues, the current research project was set to accomplish the following aims:

1. *Characterize ligand diffusion and conjugation in a bimodal PEG brush layer on the microbubble shell.*
2. *Study microbubble-induced complement activation using microbubbles with different surface architectures in vitro.*
3. *Study the effect of PEG brush surface architecture on microbubble contrast persistence in vivo.*

The following hypotheses were made regarding these specific aims:

1. Ligand diffusion and binding to the tethered functional groups at the distal end of a polymer chain is affected by the PEG overbrush in a bimodal PEG brush layer due to the steric hindrance effect. However, this effect can only be applied to ligands larger than a certain size limit since small molecules are expected to diffuse freely through polymer brushes.
2. PEG chains on the surface of microbubbles can efficiently reduce the binding of complement proteins to targeted microbubbles, and therefore, reduce their

immunogenicity. This effect is largely influenced by the surface architecture on the surface of microbubbles.

3. Targeted microbubbles with a bimodal PEG brush layer on the surface have longer circulation persistence *in vivo* due to the effective protection from the polymer chains to shield the ligands against opsonization, phagocytic uptake and non-specific adhesion.

Chapter 2: Ligand Conjugation to Targeted Microbubbles with Bimodal Poly(ethylene glycol) Brush Layers

2.1. Introduction

As mentioned in the previous chapter, microbubbles are gaining increasing attention from the science and engineering communities over the past several decades for being developed as ultrasound contrast agents for biomedical applications. A microbubble is a gas-filled colloidal particle with diameter of less than 10 μm, of which the surface typically comprises amphiphilic phospholipids self-assembled to form a lipid monolayer shell. Poly(ethylene glycol) (PEG) chains, or PEG chain derivatives, are generally incorporated into the shell of microbubbles as a stabilizing emulsifier.

The same principles of molecular diffusion in a polymer brush that characterize reactions in a polymer-grafted flat surface also apply to the surface of a curved gas-liquid interface, such as that posed by the surface of a microbubble. The flexible PEG polymer brush on the microbubble surface protects it against coalescence and macromolecule surface adsorption due to the steric hindrance effect. In aqueous solutions, PEG chains assume a coiled configuration whose dimensions depend upon polymer chain size and surface density (de Gennes 1980). Such a microstructure exerts a steric pressure and forms a repulsive barrier that inhibits contact-mediated interactions with the microbubbles (Kenworthy, Hristova et al. 1995; Kim, Klibanov et al. 2000). Large molecules, such as antibodies, are commonly assumed to be excluded from this impermeable PEG brush layer. However, for small molecules, this assumption is not expected to

hold because they can find a path to the surface through the excluded volume (Needham, Zhelev et al. 1999).

For molecular imaging applications, the primary goal is to engineer a targeted contrast agent that has both high specificity and low immunogenicity. There are many surface functionalization strategies for conjugating targeting ligands to microbubbles, most notably through attaching specific ligands to the distal end of tethered PEG chains. However, targeting ligands typically present chemical groups that could trigger an immune response and decrease microbubble contrast persistence during circulation. In order to address this issue, a stealth microbubble design with a bimodal PEG brush surface architecture, termed buried-ligand architecture (BLA), was proposed by Borden et al. (Borden, Sarantos et al. 2006; Borden, Zhang et al. 2008). The BLA microbubbles involved bimodal PEG polymer chains on the surface; the targeting ligand was attached to the shorter PEG chains (~2000 Da) and was hidden, while the longer PEG (~5000 Da) overbrush served as a shield to inhibit ligand exposure and, hence, reduced the complement activated immune response in addition to prolonging *in vivo* circulation persistence (Figure 2.1C). BLA microbubbles experienced transient conversion from stealth to active under ultrasound radiation force (USRF); the shielded ligand was only revealed for binding during microbubble oscillation in the acoustic field but buried again at the end of the USRF pulse, allowing triggered and specific adhesion at the targeted site. This BLA design allowed spatial and temporal control of targeted adhesion. Promising results have shown that BLA microbubbles, in comparison with exposed-ligand architecture (ELA) microbubbles, reduced immunogenicity without reduction in targeted adhesion.

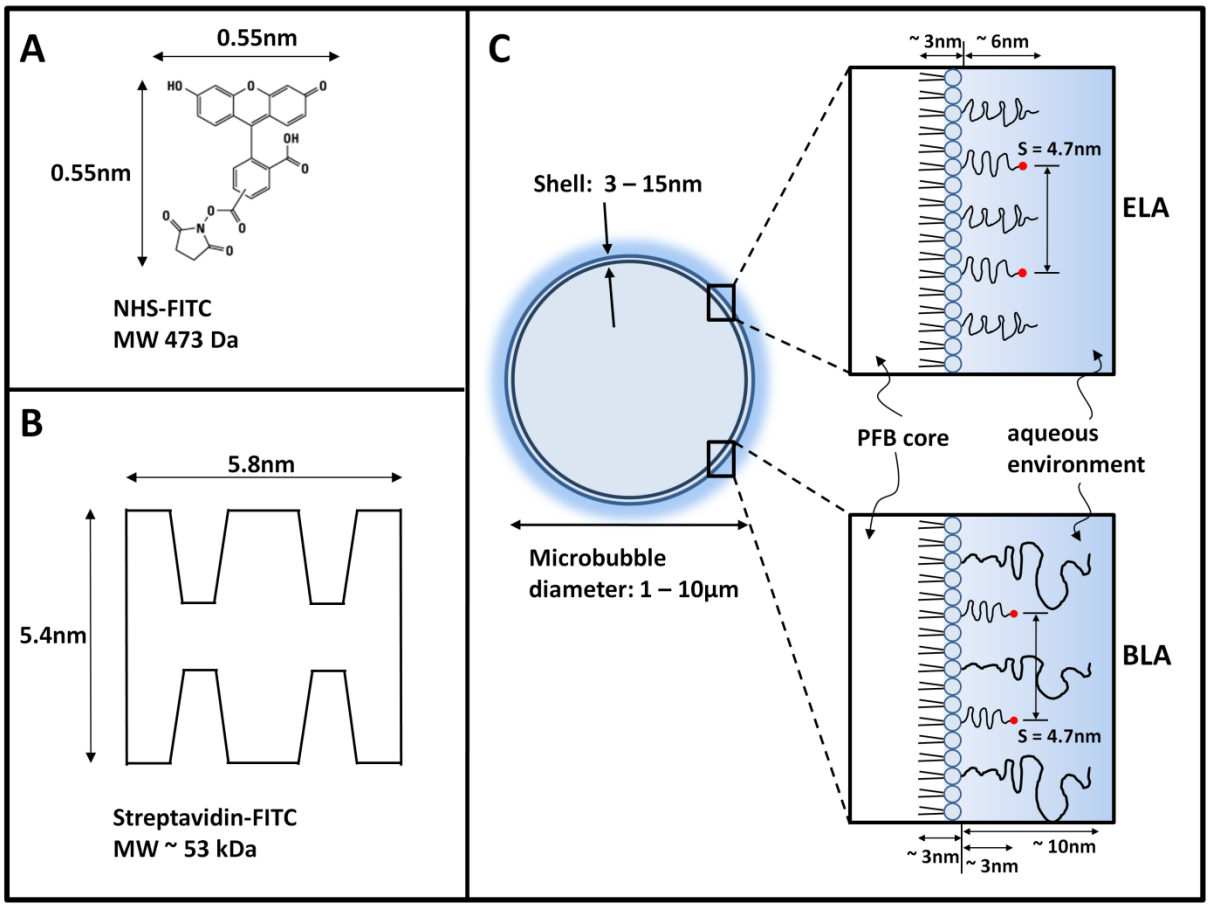

Figure 2.1. Schematic experimental design for ligand conjugation studies. (A) Molecular structure of NHS-FITC showing its estimated dimensions using the well-known Stokes-Einstein equation for the diffusion of a sphere in a liquid (Bird, Stewart et al. 2002). The diffusion constant of a free FITC molecule at 21.5 °C in water was calculated to be 0.49×10^{-9} m^2/s (Rani, Pitts et al. 2005), and the dynamic viscosity of water was estimated to be 0.979×10^{-3} kg/m·s. (B) Schematic diagram of streptavidin-FITC showing its estimated dimensions (Cooper, Shen et al. 1994). (C) Cartoon showing the dimensions of a microbubble with either ELA or BLA. The PEG chain length was estimated using self-consistent field (SCF) theory (Lai and Zhulina 1992) using values of 0.44 nm^2 for the average projected area per lipid molecule (Hollinshead, Harvey et al. 2009) and 0.35 nm for PEG monomer length. The lipid monolayer thickness was estimated to be ~3 nm based on the persistence length of the stearoyl chains (Borden, Zhang et al. 2008).

As mentioned in the previous chapter, post-labeling technique for ligand conjugation to the surface of microbubbles offers advantages such as safety, economy and ease-of-use when compared with pre-labeling. In order to utilize post-labeling for BLA microbubbles, one critical issue remains to be addressed: will the targeted ligand be able to diffuse through the PEG overbrush and bind to the tethered functional groups at the surface? On one hand, it is plausible that PEG will partially prevent the diffusion and attachment of macromolecules. However, polymer chains in solution are highly dynamic due to thermal fluctuations. Their thermally driven conformational sampling property, the breathing mode of the polymer chains, is expected to strongly affect the ligand accessibility. Jeppesen et al. (Jeppesen, Wong et al. 2001) showed that tethered molecules extend well beyond their average equilibrium configuration over an experimental time scale of seconds, which broadens the overall spatial range of tethered ligand-receptor binding. It opens the argument that, for large molecules that are excluded from the brush layer due to steric hindrance, binding to the surface is still possible due to these transient excursions of polymer chains. The kinetics of such reactions will depend on a complex interplay between polymer dynamics, molecular diffusion, and intermolecular forces.

The purpose of the present study is to experimentally test the differences in ligand diffusion and binding rate between various PEG brush architectures on the surface of microbubbles, ligand sizes, and binding modes. ELA and BLA microbubbles were generated to represent different polymer architectures. Solute size was varied by using 5/6-carboxyfluorescein succinimidyl ester (NHS-FITC) and fluorescein conjugated streptavidin (SA-FITC). NHS-FITC represents a class of smaller molecular ligands (<1 kDa, Figure 2.1A), while SA-FITC represents a class of macromolelcular ligands (>10 kDa, Figure 2.1B). By monitoring the fluorescence intensity change during binding, we showed evidence that BLA microbubbles indeed partially

prevented the binding of large molecules to the surface while allowing the uninhibited attachment of smaller ones. These findings provide insight for binding of solutes to tethered groups in various brush architectures on a Langmuir-monolayer-coated colloidal particle, such as the one posed on a microbubble.

2.2. Materials and Methods

2.2.1. Microbubble Surface Architecture Design

The microbubble phospholipid shell used for this study was designed so that the desired vertical segregation was achieved to shield the ligand from the surrounding environment when the microbubble was static, and only to reveal the ligand for targeting when the microbubble was oscillating in an ultrasound field (Figure X) (Borden, Zhang et al. 2008). The analytical expressions used for calculating the PEG brush heights were derived from self-consistent field theory by Birshtein et al. (Birshtein, Liatskaya et al. 1990), and are as follows:

$$H_0 = \left(\frac{8pv\sigma}{\pi^2}\right)^{1/3} N_S \qquad \text{Equation 2.1}$$

$$H_S = H_0\sqrt{1 - q^{2/3}} \qquad \text{Equation 2.2}$$

$$H_L = H_0\left(1 + \alpha q^{1/3}\right) \qquad \text{Equation 2.3}$$

where H_0, H_S and H_L are the monodisperse, short and long chain brush heights, respectively; p is the chain stretching parameter (assumed unity for the flexible PEG chains); v is the second virial coefficient (assumed unity for PEG in water at standard temperature and pressure); σ is the normalized surface coverage; N_S is the persistence length of the short chain; q is the fraction of the long chain and α is the relative difference in chain lengths. The value predicted using these

expressions are the PEG brush heights as time and spatial averages, and are expected to have local variations due to polymer thermal fluctuations (Jeppesen, Wong et al. 2001) and monolayer shell heterogeneities (Borden, Pu et al. 2004; Borden, Martinez et al. 2006). Equally importantly, the above expression does not include the attractive intermolecular interactions between PEG chains (such as hydrogen bond formation (Israelachvili 1991)) or the additional mass effect of the conjugated RGD peptide on the distal end of the PEG chains.

2.2.2. Materials

All phospholipids were purchased from Avanti Polar Lipids, Inc. (Alabaster, AL), including 1,2-distearyol-sn-glycero-3-phosphocholine (DSPC), 1,2-distearyol-sn-glycero-3-phosphoethanolamine-N-[methoxy(polyethylene glycol)2000] (DSPE-PEG2000), 1,2-distearyol-sn-glycero-3-phosphoethanolamine-N-[amino(polyethylene glycol)2000] (DSPE-PEG2000-A), 1,2-distearyol-sn-glycero-3-phosphoethanolamine-N-[biotinyl(polyethylene glycol)2000] (DSPE-PEG2000-B) and 1,2-distearyol-sn-glycero-3-phosphoethanolamine-N-[methoxy(polyethylene glycol)5000] (DSPE-PEG5000). The emulsifier polyoxyethylene-40 stearate (PEG40S) was purchased from Sigma-Aldrich (St. Louis, MO). All microbubble shell components were dissolved in chloroform (Sigma-Aldrich) and stored in the freezer at -20 °C. The perfluorobutane gas (PFB, 99 wt% purity) used for microbubble generation was purchased from FluoroMed, L.P. (Round Rock, TX). The fluorophore probes 3,3'-dioctadecyloxacarbocyanine perchlorate (DiO) and 1,1'-dioctadecyl-3,3,3;3;-tetramethylindocarbocyanine perchlorate (DiI) solutions (Invitrogen; Eugene, OR) were used to label microbubbles during the size-isolation and multimodality experiments, respectively. NHS-FITC and SA-FITC were obtained from Pierce (Rockford, IL) and dissolved in N,N-

dimethylformamide (DMF; Sigma-Aldrich) and 18 MΩ-cm deionized water (Direct-Q Millipore; Billerica, MA), respectively. Both solutions were stored at 4 °C and discarded after 2 weeks.

2.2.3. Microbubble Generation

The compositions of microbubble samples for each experiment performed are listed in Table 2.1. The indicated amount of each lipid species was mixed in a separate vial, and chloroform was evaporated by flowing a steady stream of nitrogen over the vial during vortexing for about 10 minutes followed by several hours under house vacuum. 0.01 M phosphate buffer saline (PBS) solution (Sigma-Aldrich) was filtered using 0.2 μm pore size polycarbonate filters (VWR; West Chester, PA), and mixed with 10 vol% glycerol solution (Sigma-Aldrich) and 10 vol% 2-propanol solution (Sigma-Aldrich) to increase viscosity and lipid solubility. The dried lipid film was then hydrated with PBS mixture to a final lipid/surfactant concentration of 1 mg/mL.

Table 2.1. Microbubble compositions for ligand conjugation studies

	Phospholipid Composition (mol%)				
Experiment	DSPC	DSPE-PEG2000	DSPE-PEG2000-A	DSPE-PEG2000-B	DSPE-PEG5000
ELA Control	90	10	-	-	-
ELA-Biotin	90	8	-	2	-
ELA-Amine	90	8	2	-	-
BLA Control	90	2	-	-	8
BLA-Biotin	90	-	-	2	8
BLA-Amine	90	-	2	-	8

Two methods of microbubble generation were used. For size isolation experiments, probe sonication was used as described elsewhere (Feshitan, Chen et al. 2009). Briefly, the hydrated lipid mixture was first sonicated with a 20 kHz probe (Model 250A, Branson Ultrasonics, Danbury, CT) at low power (power setting dialed to 3/10; 3 W) in order to heat the lipid suspension above the DSPC main phase transition temperature (~ 55 °C) and further disperse the lipid aggregates into small, unilamellar liposomes (Kim and Franses 2005). 1 mM DiO solution was added to the lipid suspension at an amount of 1 μL DiO solution per mL of lipid mixture. PFB was introduced by flowing it over the surface of the lipid suspension. Subsequently, high power sonication (power setting dialed to 10/10; 33 W) was applied to the suspension for about 10 s at the gas-liquid interface to generate microbubbles. No extra washing steps were done for the size-isolation experiment. For the multimodality and FITC-ligand binding experiment, the shaking method was used to generate microbubbles. The lipid suspension was first heated to 60 °C in a digital heatblock (VWR) for 10 min, and then sonicated at 60 °C in a bath sonicator (Model 1510, Branson Ultrasonics; Danbury, CT) for 30 s so that the lipid aggregates were completely dispersed. 1 mM DiI solution was added to the lipid suspension at an amount of 1 μL DiI solution per mL of lipid mixture to generate fluorescently labeled microbubbles for the multimodality experiment. 2 mL of lipid suspension was then transferred to a 3 mL serum vial and sealed for gas exchange. Gas exchange of the vial headspace was done by first vacuuming out air and then flowing PFB into the vial. At least three cycles of gas exchange were done to ensure the lipid suspension was saturated with PFB, and subsequently a 27G needle was used to vent the vial in order to release the excess pressure. Microbubbles were formed by shaking with a VialMix (ImaRx Therapeutics; Tucson, AZ) for 45 s. The generated microbubbles were then diluted to 10 mL suspension with PBS, and washed 3

times by centrifugation flotation in a bucket-rotor centrifuge (Model 5804, Eppendorf; Westbury, NY) at 250G for 5 min. The microbubble cake was finally diluted with PBS for subsequent experiments. For NHS-FITC binding, pH adjusted PBS solution (pH 8.5) was used. PBS at physiological pH (7.4) was used for all other experiments, unless otherwise stated.

2.2.4. Microbubble Size Isolation and Flow Cytometry Gate Determination

Microbubble size isolation was done as described elsewhere (Feshitan, Chen et al. 2009). This technique allowed us to more effectively isolate microbubbles with a desired diameter due to their multimodal size distribution. Three microbubble size ranges were isolated: 1-2 μm, 4-5 μm and 6-8 μm. An Accusizer optical particle counter (NICOMP Particle Sizing System; Santa Barbara, CA) was used to measure the size distribution and particle concentration. Flow cytometry ($1x10^5$ events) was performed immediately afterward using an Accuri C6 flow cytometer (Accuri Cytometers Inc.; Ann Arbor, MI). The forward-scatter height (FSC-H) threshold was adjusted to delineate the microbubble populations from instrument and sample noise. The system setting was held constant for all subsequent measurements.

2.2.5. Optimization of FITC Ligand:Functionalized Lipid Ratio

Based on the size distribution and concentration data obtained using the Accusizer, each microbubble sample was diluted to about $1x10^9$ #/mL. It is reported that the average projected area per lipid molecule for DSPC is 0.44 nm^2 (Hollinshead, Harvey et al. 2009). Keeping the same value for the other PEGylated phospholipid species, the total number of lipid molecules on the shell surface was calculated. Assuming the uptake of lipid molecules to the shell was the same for all species, the relative molar ratio of lipid components in the microbubble shell is

expected to be the same as in the bulk suspension (Borden, Martinez et al. 2006). The total number of functional groups present on the surface of microbubbles was then calculated, and the excess amount of FITC ligand (molar ratio varied from 0.04:1 to 100:1 and 0.05:1 to 1.5:1 for NHS-FITC:DSPE-PEG2000-A and SA-FITC:DSPE-PEG2000-B, respectively) needed for conjugation was obtained. 500 μL of microbubble suspension was transferred to a 3 mL syringe for NHS-FITC binding, and 100 μL of microbubble suspension was transferred to a 1 mL syringe for SA-FITC binding. Samples were incubated with the indicated amount of FITC ligand in the dark overnight on a benchtop rotator at room temperature. Unreacted NHS-FITC or SA-FITC was removed by centrifuging the sample at 250G for 5 min. The concentrated microbubble cake was then re-suspended in PBS and analyzed by flow cytometry.

2.2.6. FITC Ligand Binding Kinetics

Microbubble suspensions were incubated with the indicated amount of FITC ligand in the dark on a benchtop rotator at room temperature. FITC ligand binding was continuously monitored for 6 hrs. 2 μL samples were taken out at different time points for flow cytometry measurement. A pseudo-first order association kinetics model (Saltzman 2001), given by Equation 2.4, was used to fit all median fluorescence intensity versus time data,

$$Y = Y_{max}(1 - e^{-k_{obs}t}) \qquad \text{Equation 2.4}$$

where Y_{max} is maximum median fluorescence intensity (MFI) increase and k_{obs} is the observed binding rate constant in units of hr^{-1}. Curve fitting parameters for each data set were obtained using the nonlinear regression tool in Prism software (GraphPad Software, Inc; La Jolla, CA). All curves showed reasonable goodness of fit with R^2 values approximately 0.92 and above, except for SA-FITC ELA 1-2 μm microbubble sample (discussed below).

2.2.7. Optical Microscopy

Direct visual confirmation of microbubble fluorescence was performed within 24 hrs after FITC ligand binding. Microbubble samples were taken out of the reaction syringe and imaged at room temperature. Still images were taken using an Olympus 1X71 inverted microscope (Olympus; Center Valley, PA), and Z-scan images were taken using an Olympus BX60M upright microscope with 0.5-μm scan step size across a 10-μm distance. Images were captured in epi-fluorescence mode using a high-resolution digital camera (Orca HR, Hamamatsu; Japan) with a 100x oil immersion objective and processed with Simple PCI software (C-Imaging; Cranberry Township, PA). Subsequent image analysis was done using ImageJ 1.4g software (NIH; Washington DC.).

2.3. Results and Discussion

2.3.1. Microbubble Size Isolation and Flow Cytometry Gate Determination

Our group recently introduced a microbubble size isolation technique using differential centrifugation (Feshitan, Chen et al. 2009). It provides a rapid and robust method for size selection and reduces polydispersity of microbubble samples. As we previously reported, it also isolated the microbubbles from precursor liposomes and non-echogenic nanobubbles, which may be recycled for additional microbubble production. Based on the size distribution, we estimated that only between 1 – 10% of the original lipid molecules were incorporated into the microbubble shells. Similar to our previous report (Feshitan, Chen et al. 2009), we observed a multimodal size distribution using both the Accusizer and the flow cytometer. The black symbols shown in Figure 2A and 2B are the number % and volume % of sizing data from a freshly made (polydisperse) sample. Distinct peaks in both plots were detected, especially in the

volume % distribution, indicating dominant size ranges in the microbubble population. These distinct peaks were consistent across all microbubble samples. The corresponding forward- versus side-scatter (FSC vs. SSC) density plot for the polydisperse sample is shown in Figure 2C. A characteristic serpentine shape was detected as previously observed by our group (Feshitan, Chen et al. 2009). The serpentine scattergram appeared to correlate with the distinct peaks shown in the size distribution determined by Accusizer.

In order to further investigate microbubble size multimodality, we used a fluorescence-based detection method. DiI labeled microbubbles were centrifuged to remove the liposomes, nanobubbles and some of the 1-2 μm population so that the 1-2 μm and 4-5 μm peaks shown in the number % size distribution were of similar magnitude (Figure 2.3A). This step was necessary since 1-2 μm microbubbles present in a freshly made suspension dominated the events detected using flow cytometry. Microbubbles with different sizes could not be otherwise detected and represented on the fluorescence histogram. The FSC vs. SSC density plot and median fluorescence intensity (MFI) histogram of the centrifuged sample is shown in Figure 2.3B and 2.3C. The MFI histogram clearly showed a multimodal distribution that corresponded to the Accusizer measurement, lending support to the validity of the multimodal size distribution rather than an optical scattering phenomenon.

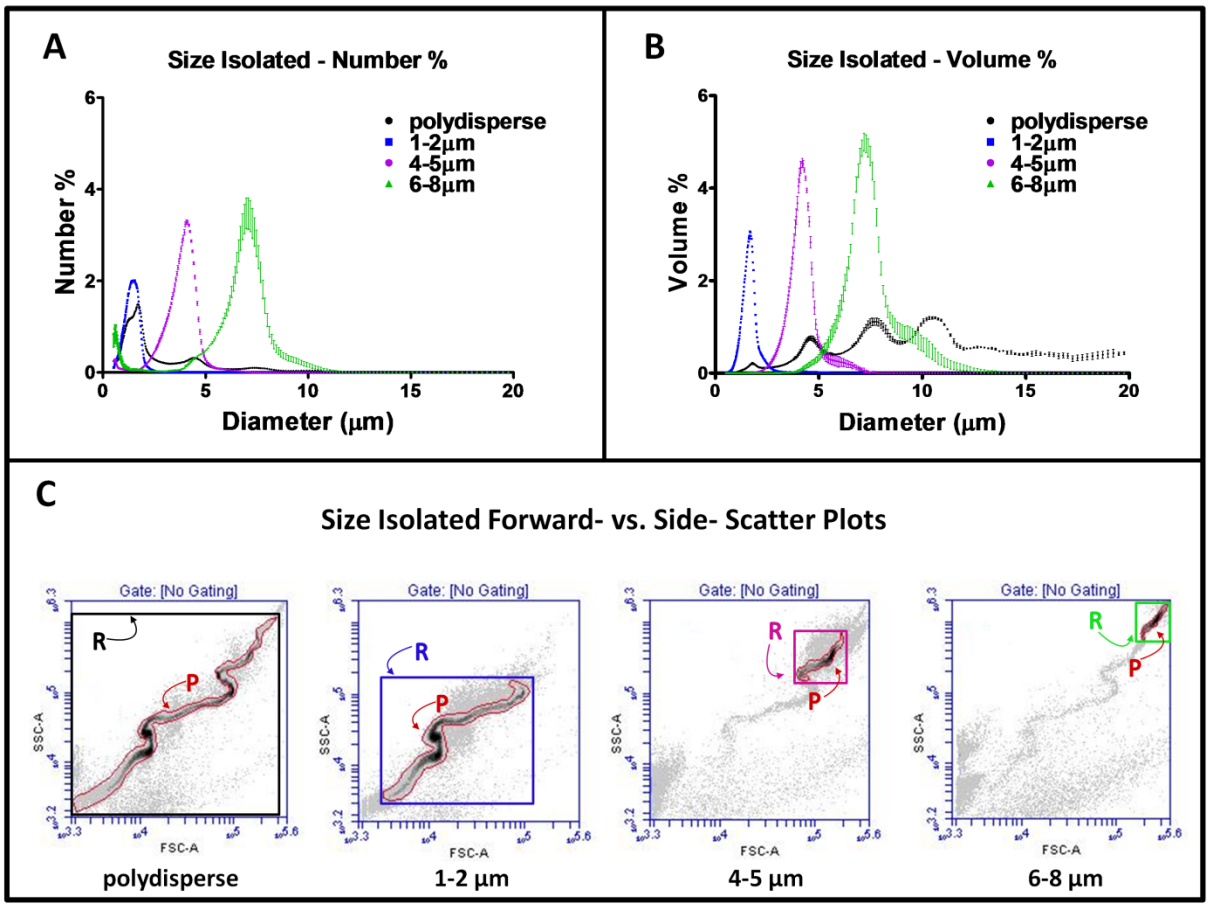

Figure 2.2. Microbubble size isolation and flow cytometry gate determination. Number-weighted (A) and volume-weighted (B) microbubble size distributions before and after size isolation are compared. Each curve is the average of three measurements with its SD plotted as error bars. (C) Forward-scattering (FSC) versus side-scattering (SSC) plots of corresponding microbubble samples before and after size isolation. A tight fitted P gate and a rectangular R gate were drawn for each scatter plot and saved as templates for all subsequent measurements in order to identify each size subpopulation in a polydisperse suspension.

Figure 2.2A and 2.2B also show the sizing data for the size-isolated microbubbles with diameter between 1-2 μm, 4-5 μm and 6-8 μm. The volume-weighted median diameters ± standard deviations (SD) were 1.71±0.01 μm, 4.07±0.12 μm and 7.13±0.12 μm, respectively. The corresponding FSC vs. SSC density plots for each population are shown in Figure 2.2C. A tight-fitted (P) gate and a rectangular (R) gate was drawn around the densest region of the scatter plots to identify each size subpopulation. The density plots for 4-5 μm and 6-8 μm size-isolated samples showed faint traces of the serpentine shape similar to the polydisperse sample, which might result from the presence of residual smaller microbubbles in the sample. By combining differential centrifugation and flow cytometric gating, we were able to accurately identify microbubble subpopulations in a polydisperse sample. The gate information determined using the size-isolated samples was saved as a template for all subsequent analyses of polydisperse microbubble suspensions. In order to ensure a proper representation of the entire microbubble population, $1x10^5$ events were measured for all samples.

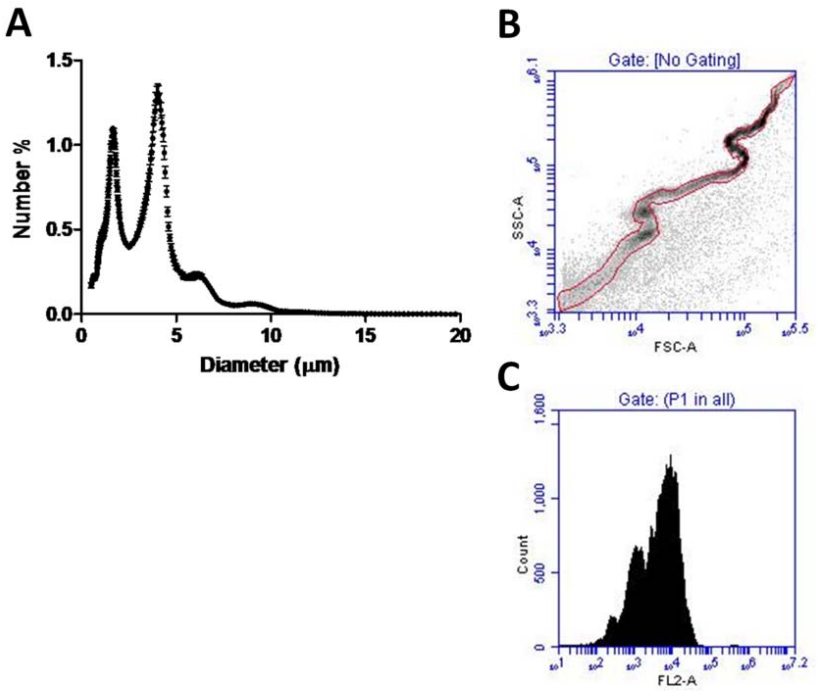

Figure 2.3. Illustration of multimodal size distribution of fluorescently labeled microbubbles. (A) Size distribution of the DiI labeled microbubble suspension after partially removing part of the 1-2 µm population. The 1-2 µm and 4-5 µm peaks shown in the number% size distribution were of similar magnitude to ensure proper event detection using flow cytometry. (B) FSC versus SSC density plot of the same microbubble suspension. (C) MFI histogram of the same microbubble suspension showing a multimodal size distribution that corresponded to the Accusizer measurement.

2.3.2. Optimization of FITC Ligand:Functionalized Lipid Ratio

Flow cytometry was used to analyze the binding of the FITC ligands to the PEG-terminal functional groups. Figure 2.4 shows sample MFI histograms before and after ligand conjugation. The washed polydisperse suspension, which had a dominant 1-2 µm peak and sometimes a relatively large 4-5 µm peak, gave a log-normal or sometimes bimodal distribution in fluorescence intensity (e.g., Figure 2.4A). Increased MFI, which was indicated by a shift of the

distribution to the right, confirmed the binding of FITC ligand on the microbubble surface. Control microbubbles showed very little or no MFI increase for either NHS-FITC or SA-FITC, regardless of the microbubble surface architecture.

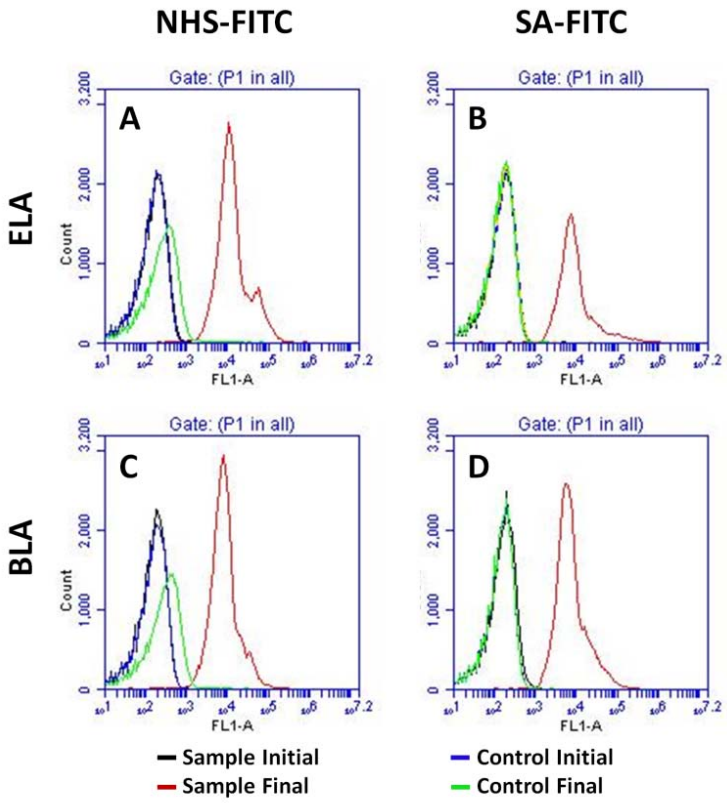

Figure 2.4. Typical flow cytometry fluorescence intensity histograms of microbubbles with different architectures before and after ligand conjugation. (A) NHS-FITC ELA binding. (B) SA-FITC ELA binding. (C) NHS-FITC BLA binding. (D) SA-FITC BLA binding.

In order to perform a sensitive analysis of ligand conjugation kinetics, studies were done to find the saturation point for NHS-FITC and SA-FITC (Figure 2.5). For both ELA and BLA, MFI change increased by about 3 orders of magnitude when the NHS-FITC:DSPE-PEG2000-A molar ratio was increased from 0.04 to 20 and leveled off to 100 (Figure 2.5A). A similar trend

was observed for SA-FITC:DSPE-PEG2000-B, although the saturation molar ratio occurred at 0.5 (Figure 2.5B). The 0.5 saturation molar ratio was consistent with the theoretical prediction since each SA-FITC molecule has four biotin binding pockets with only two facing the PEG brushes at a time. Both molar ratios were identified as the saturation point and used to calculate the appropriate amount of FITC ligand for all subsequent kinetics experiments.

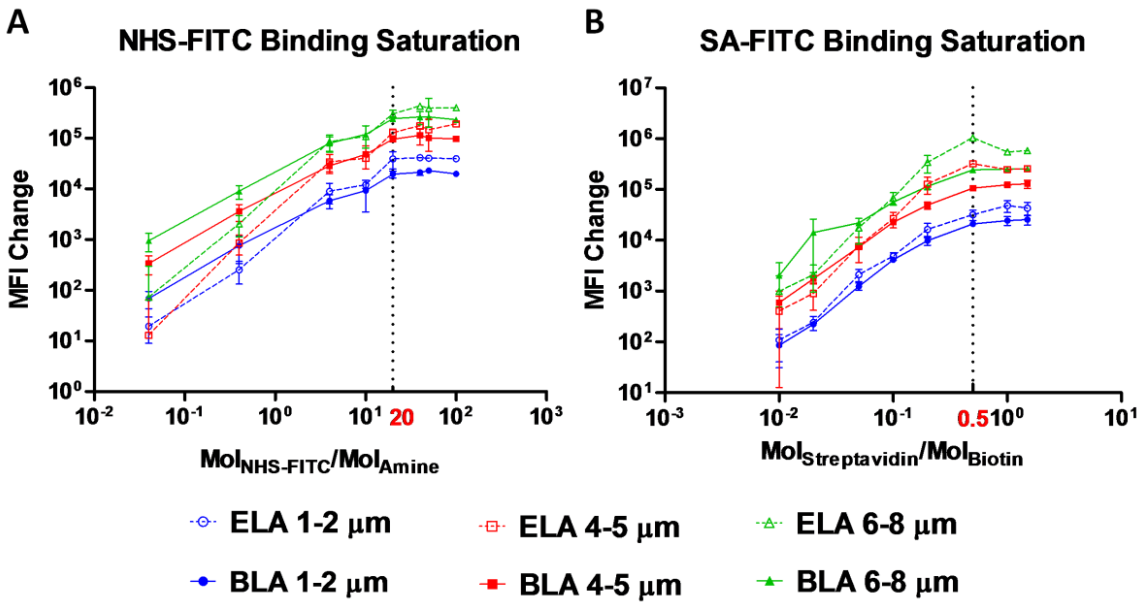

Figure 2.5. Optimization of ligand:functionalized lipid ratio. MFI was measured before and after microbubble samples reacted with various amounts of ligands after 12 hr at room temperature. (A) NHS-FITC/DSPE-PEG2000-A with molar ratio varied between 0.04 and 100. A molar ratio of 20 (dashed line) was used for all subsequent kinetics studies. (B) SA-FITC/DSPE-PEG2000-B with molar ratio varied between 0.01 and 1.5. A molar ratio of 0.5 (dashed line) was used for all subsequent kinetics studies.

2.3.3. Small Molecule (NHS-FITC) Binding Kinetics

It is commonly accepted that the protective mechanism of PEG polymer chains for liposomes (Klibanov, Maruyama et al. 1990) or microbubbles (Klibanov 1999) comes from their flexibility to form a "cloud" that sterically hinders the adsorption of opsonins to the surface and hence reduces the rapid clearance of these colloidal particles by the MPS (Torchilin, Papisov et al. 1995). However, it is unclear whether this mechanism interferes with the diffusion and attachment of targeting ligands to the buried PEG chains. It was hypothesized that smaller molecules, such as NHS-FITC, would be able to diffuse freely through the excluded volume of PEG and bind to the tethered amino groups at the end of the shorter PEG chains for both microbubble surface architectures. Indeed, by monitoring MFI increase using flow cytometry, almost identical NHS-FITC binding kinetics for each size range were obtained between ELA and BLA over 6 hr (Figure 2.6). Table 2.2 summarizes the best-fit values obtained for the pseudo-first-order kinetics parameter. Y_{max} and k_{obs} values for BLA microbubbles were more than 80% of those measured for ELA, independent of microbubble size. This result confirmed the hypothesis that the diffusion and binding of NHS-FITC to the tethered amino groups was not significantly inhibited by the PEG overbrush.

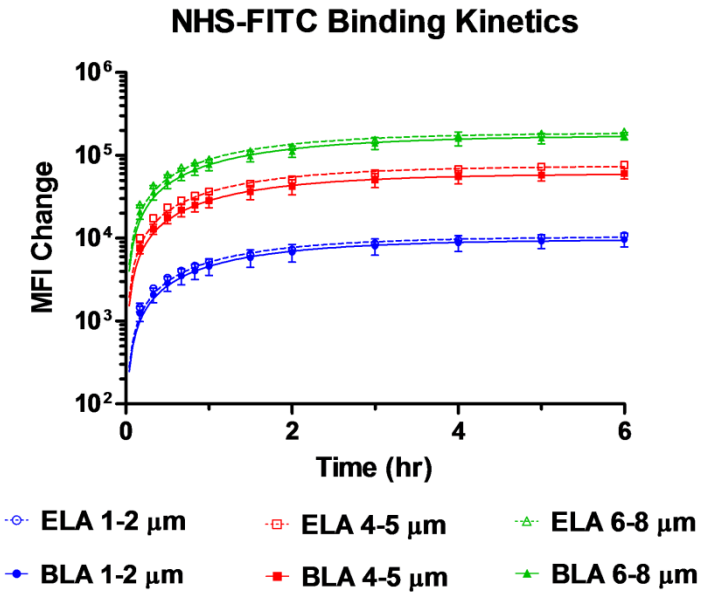

Figure 2.6. NHS-FITC binding kinetics to the tethered amino functional groups after microbubble formation. MFI was monitored continuously over 6 hr, and MFI change before and after reaction for each size range was plotted at different time points. Data was fitted using a pseudo-first-order reaction kinetic model. ELA and BLA showed good agreement for both the observed binding rate and the final MFI over the experimental time scale.

Table 2.2. Summary of best-fit values obtained for NHS-FITC ligand binding kinetics curves using a pseudo-first-order kinetics equation (Eq 1)

	NHS-FITC Binding			
	ELA		BLA	
Sample Size Range	Y_{max} (AFU)*	k_{obs} (hr^{-1})	Y_{max} (AFU)*	k_{obs} (hr^{-1})
1-2 µm	1.1×10^4	0.67	9.6×10^3	0.65
4-5 µm	7.5×10^4	0.66	6.0×10^4	0.64
6-8 µm	1.9×10^5	0.64	1.7×10^5	0.58

* **AFU: arbitrary fluorescence unit**

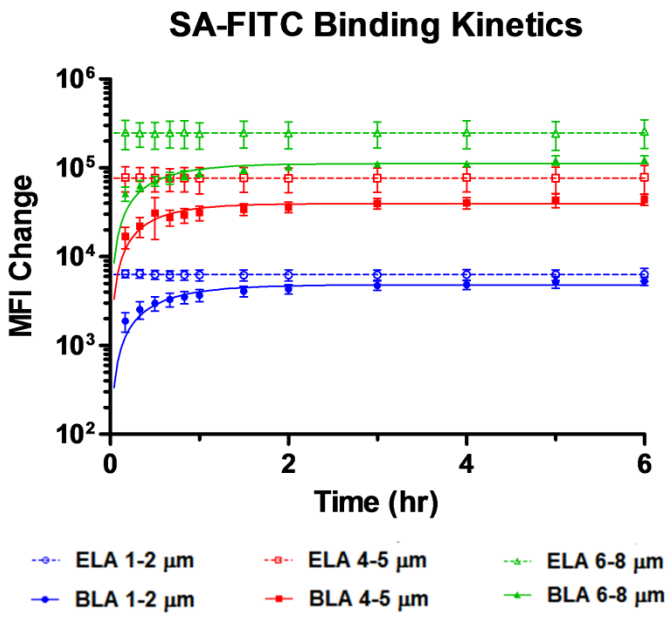

Figure 2.7. SA-FITC binding kinetics to the tethered biotin functional groups after microbubble formation. ELA reached saturation binding within the first 10 min of reaction. However, BLA showed a gradual increase of MFI over the first 2 hr of reaction with a half-time around 30 min for all size ranges. The differences in binding rate agrees with the hypothesis that the PEG overbrush interferes with the diffusion of large molecules to the surface of microbubbles and partially blocks their binding to the buried functional end groups.

In order to further analyze the binding kinetics, MFI changes were normalized using the final MFI value taken at 6 hr (Figure 2.8A and 2.8C). Interestingly, binding curves for all three size ranges collapsed to a single curve over the 6 hr experiment. This indicated that NHS-FITC ligand binding occurred at the same rate, independent of microbubble size, in both ELA and BLA designs.

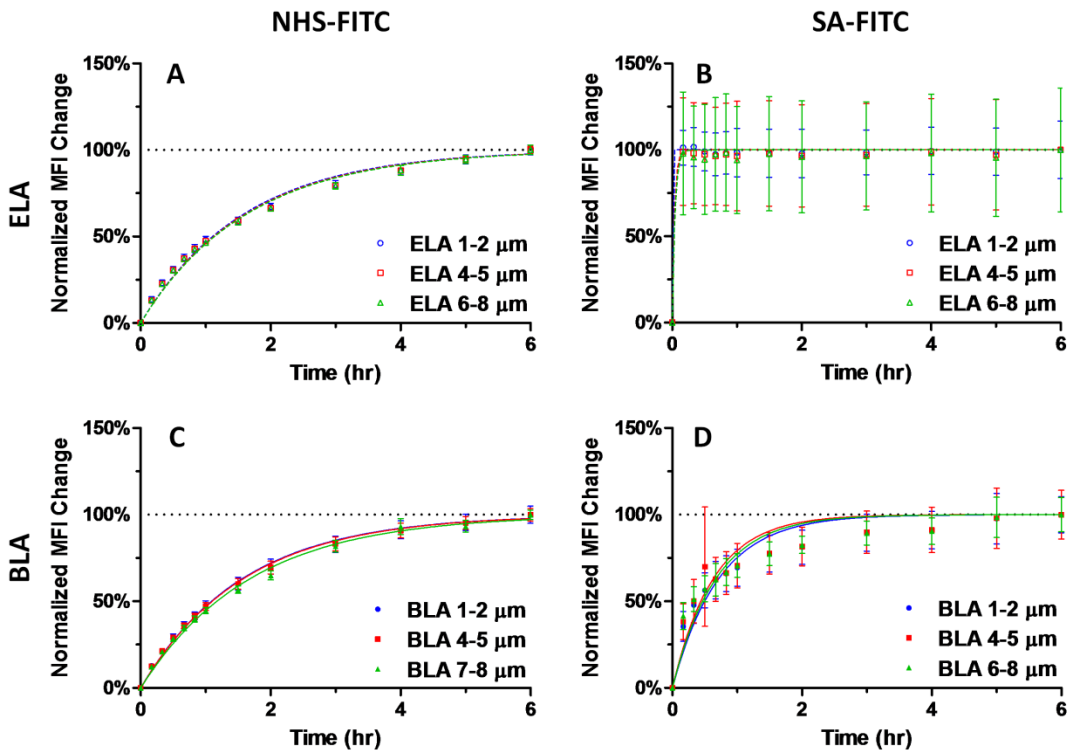

Figure 2.8. Comparison of normalized MFI change between ELA and BLA microbubbles for all size ranges. The last measured MFI was used for normalization as the final saturation value. The curves were obtained using a pseudo-first-order kinetic model. The fitted binding rate for all size ranges was the same for each condition, indicating that the ligand binding rate was independent of microbubble size.

NHS-FITC is similar in molecular weight to several small-molecule peptide ligands, such as cyclic-arginine-glycine-asparagine (RGD). RGD has been shown to bind to an overexpressed angiogenic biomarker, $\alpha_v\beta_3$ integrin, with high affinity and specificity (Miller, Pien et al. 2005; D'Andrea, Del Gatto et al. 2006). Using RGD labeled microbubbles with ultrasound molecular imaging, one can monitor and guide therapy of VEGF-blockage for cancer therapy (Iagaru, Chen et al. 2007; Hargreaves 2008). By showing that NHS-FITC was able to diffuse through the PEG overbrush and bind to the tethered PEG, the feasibility of post-labeling for small-molecule ligand

(<1 kDa) to BLA microbubbles to generate stealth targeted ultrasound contrast agent was demonstrated.

2.3.4. Macromolecule (SA-FITC) Binding Kinetics

It was hypothesized that macromolecules (>10 kDa), such as SA-FITC, would not be able to diffuse freely through the PEG overbrush and bind to tethered biotin end groups due to steric hindrance in the buried-ligand architecture. Indeed, Figure 2.7 shows significant differences in SA-FITC binding curves between ELA and BLA for each microbubble size range. ELA binding curves reached the saturation MFI values within the first 10 min of reaction and stayed constant throughout the rest of the experiment. BLA binding curves, on the other hand, showed a gradual increase during the first hour of reaction, reaching the saturation MFI values at approximately 2 hr. the final MFI values for each size range in ELA were significantly higher than those in BLA, with the average Y_{max} percentage being only 58% of that for ELA (Table 2.3), indicating that the binding of SA-FITC to buried biotin groups was significantly inhibited by the longer PEG chains.

Table 2.3. Summary of best-fit values obtained for SA-FITC ligand binding kinetics curves using a pseudo-first-order kinetics equation (Eq 1)

	SA-FITC Binding			
	ELA		BLA	
Sample Size Range	Y_{max} (AFU)*	k_{obs} (hr^{-1})	Y_{max} (AFU)*	k_{obs} (hr^{-1})
1-2 μm	6.3×10^3	-	4.8×10^3	1.80
4-5 μm	7.7×10^4	-	4.- x 10^4	2.18
6-8 μm	2.5×10^5	-	1.1×10^5	1.98

* **AFU: arbitrary fluorescence unit**

Again, the effect of microbubble size on SA-FITC conjugation was investigated. Normalized MFI changes showed all binding rates collapsed into a single curve, indicating that SA-FITC binding for microbubbles with different diameters was the same (Figure 2.8B and 2.8D). Similar to the case of NHS-FITC, the diffusion and binding of SA-FITC was not affected by microbubble size for either ELA or BLA designs.

The kinetics curves for the 1-2 μm size range are shown in Figure 2.9 to further illustrate the significant difference in binding rate between ELA and BLA microbubbles for different ligand sizes. For NHS-FITC, the normalized binding curves showed very little difference between the two brush architectures over 6 hr, with the fitted k_{obs} values in close agreement between ELA and BLA (Table 2.4). On the other hand, for SA-FITC binding, the ELA kinetic curve closely resembles a step function with the MFI value reaching its saturation Y_{max} within 10 min; yet the BLA kinetic curve showed a more gradual increase over time with a much slower binding rate constant. Unfortunately, due to the fact that ELA samples reached their saturation MFI before the first flow cytometry measurement was taken, reliable k_{obs} values were not obtained for a more quantitative comparison.

Table 2.4. Summary of best-fit values obtained for normalized FITC ligand binding kinetics curves*

	NHS-FITC Binding		SA-FITC Binding	
Sample Size Range	ELA k_{obs} (hr^{-1})	BLA k_{obs} (hr^{-1})	ELA k_{obs} (hr^{-1})	BLA k_{obs} (hr^{-1})
1-2 μm	0.63	0.64	-	1.40
4-5 μm	0.62	0.63	-	1.58
6-8 μm	0.61	0.59	-	1.48

***All MFI values were normalized by the corresponding best-fit Y_{max} values listed in Table 2.2 and 2.3**

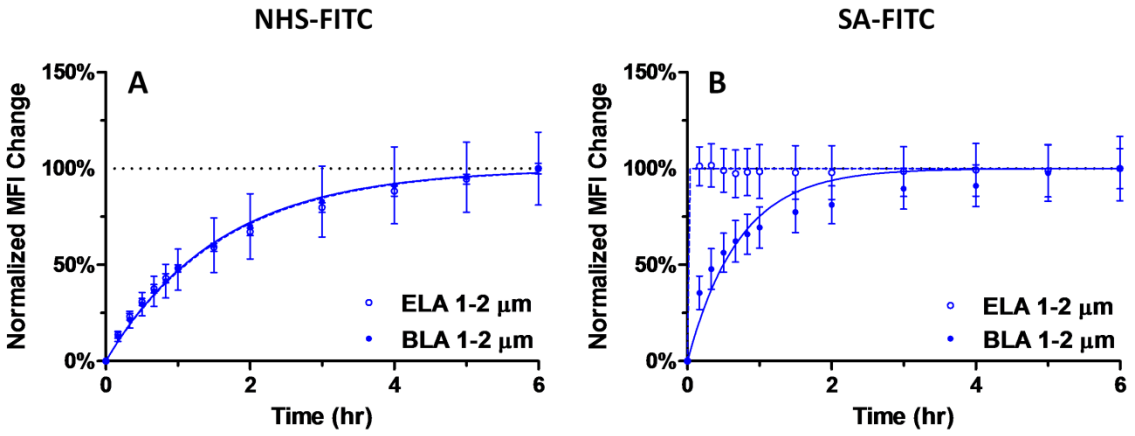

Figure 2.9. Sample comparison between normalized MFI change for ELA and BLA 1-2 µm microbubbles. The binding rate for NHS-FITC between ELA and BLA was the same, confirming the hypothesis that the diffusion and attachment of small molecules to the tethered short PEG chains was not affected by the overbrush. On the other hand, the binding rate for SA-FITC between ELA and BLA was significantly different, particularly during the first 30 min of reaction, indicating that the binding of large SA-FITC molecules was slowed by the PEG overbrush in BLA.

2.3.5. Availability of Tethered Functional Groups in a Bimodal Polymer Brush

Interestingly, the PEG overbrush did not completely eliminate macromolecule conjugation. Previous findings have shown that phase separation between phospholipid species can exist on lipid monolayers coating the microbubble surface (Kim, Costello et al. 2003; Borden, Pu et al. 2004; Borden, Martinez et al. 2006; Tanwir and Tsoukanova 2008; Lozano and Longo 2009; Lozano and Longo 2009). It is suggested here that two distributions of PEG-lipid conjugates may exist on the surface of microbubbles, which are formed during the initial self-assembly process: domains with DSPE-PEG2000-X and DSPE-PEG5000 well mixed, and peripheral regions comprising buried ligands that are not completely shielded by the PEG overbrush (Figure 2.10). Smaller ligands, such as NHS-FITC, may diffuse freely through the

excluded volume of PEG and bind to the amino groups in the center of the PEG-rich domains. Needham and co-workers (Needham, Zhelev et al. 1999; Kim, Klibanov et al. 2000) modeled the diffusion of small molecules through a surface-grafted PEG layer as a function of polymer molecular weight. It was found that as the PEG molecular weight increased the volume fraction of polymer in the excluded volume decreased, indicating that there was more free-water volume for small molecules to penetrate. The results obtained in the present study illustrated that the presence of the DSPE-PEG5000 overbrush does not interfere with the diffusion of NHS-FITC molecules to the tethered amino groups.

On the other hand, the binding of SA-FITC to tethered biotin groups in BLA microbubbles was significantly lower (~58%) than that for ELA microbubbles. It is proposed that this is because the observed binding of SA-FITC mainly occurred to the tethered biotin groups on the peripheral DSPE-PEG2000-B chains, where the longer DSPE-PEG5000 chains did not form a complete dense cloud over the buried biotin groups. In the central PEG-rich domain regions, SA-FITC molecules could not overcome the steric hindrances of DSPE-PEG5000 chains and therefore were physically inhibited from binding to the biotin groups, which resulted in the differences in the final saturated MFI values between ELA and BLA microbubbles.

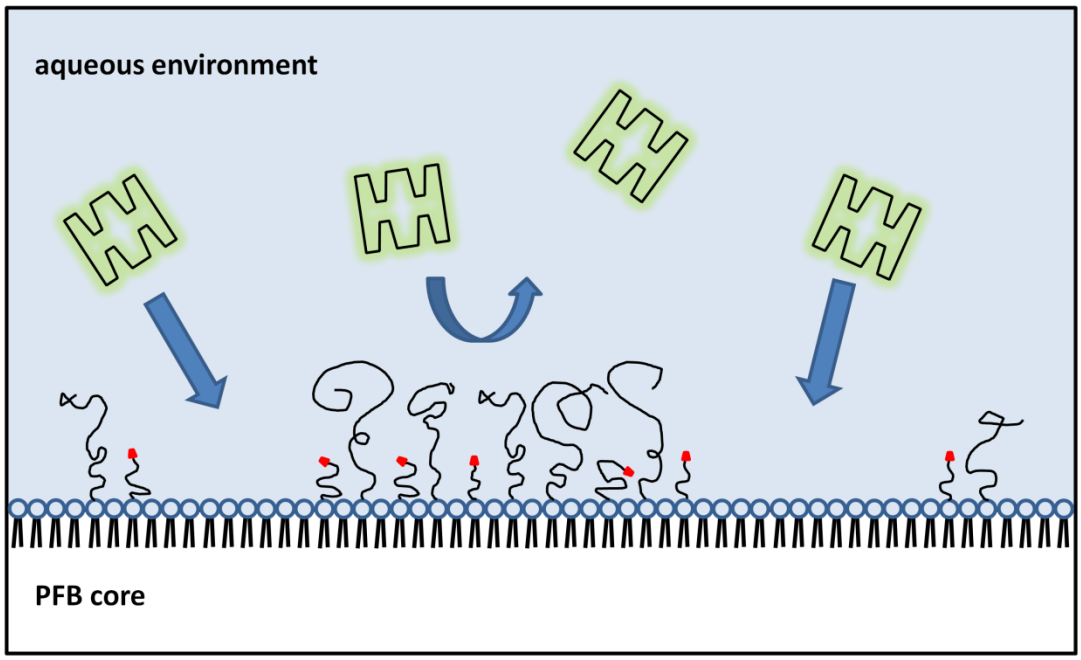

Figure 2.10. Cartoon illustrating possible phase separation between lipid species on the surface of microbubbles.

It is also possible that the transient excursion of PEG chains could result in some SA-FITC:DSPE-PEG2000-B binding in the central regions of the domains. If this were the case, SA-FITC would continue to bind, and a linear increase of MFI over time would be observed. However, the significantly lower MFI values of BLA microbubbles and the nonlinear binding curves both indicated that such events occurred at a very low frequency over the experimental period, suggesting that physical inhibition of SA-FITC molecules due to the steric repulsion resulted the difference in final MFI values between ELA and BLA microbubbles.

Using a surface force apparatus, Moore and Kuhl (Moore and Kuhl 2006) measured the specific and nonspecific forces between a streptavidin-coated surface and a bimodal PEG mushroom with buried biotin and a similar lipid composition as what was tested in the present study. It was found that the presence of longer PEG did not significantly change the capture

distance of specific adhesion even though the steric repulsion between these two surfaces was increased. The discrepancy between their results and what is reported here can be explained by the differences in experimental design. Moore and Kuhl had two surfaces slowly approach each other, allowing the tethered biotin end groups enough time to equilibrate and bind to apposed streptavidin molecules under compression (Moore, Mulder et al. 2008). The present study is different in that microbubbles and ligand molecules diffused freely in solution. There were no external forces acting on the system. Therefore, all measured binding events were the result of passive diffusion. The results presented here confirmed the previous findings reported by Borden et al. (Borden, Sarantos et al. 2006) using a similar system, where microbubbles were flowing through a parallel-plate flow chamber and allowed to bind to surface-adsorbed avidin molecules. It was shown that BLA microbubbles were able to successfully bury the targeting ligands and reduce specific adhesion in comparison with ELA microbubbles when no USRF was applied. In the current study, the presence of longer PEG showed a significant effect on the binding of SA-FITC, supporting the hypothesis that the diffusion of macromolecules through the PEG overbrush was partially inhibited.

2.3.6. Streptavidin-Induced Microbubble Surface Structure

Epi-fluorescence microscopy images provided direct visual confirmation for the conjugation of FITC ligands to the surface of microbubbles (Figure 2.11). All microbubble samples appeared to be stable during observation. When compared with bright-field images, all polydisperse microbubbles were visible under epi-fluorescence mode (data not shown). There was no preferential attachment of ligands due to microbubble size. Microstructural features

within the lipid shells were detected (see arrows in Figure 2.11A and 2.11B), indicating non-uniform distribution of FITC ligand on the microbubble surface.

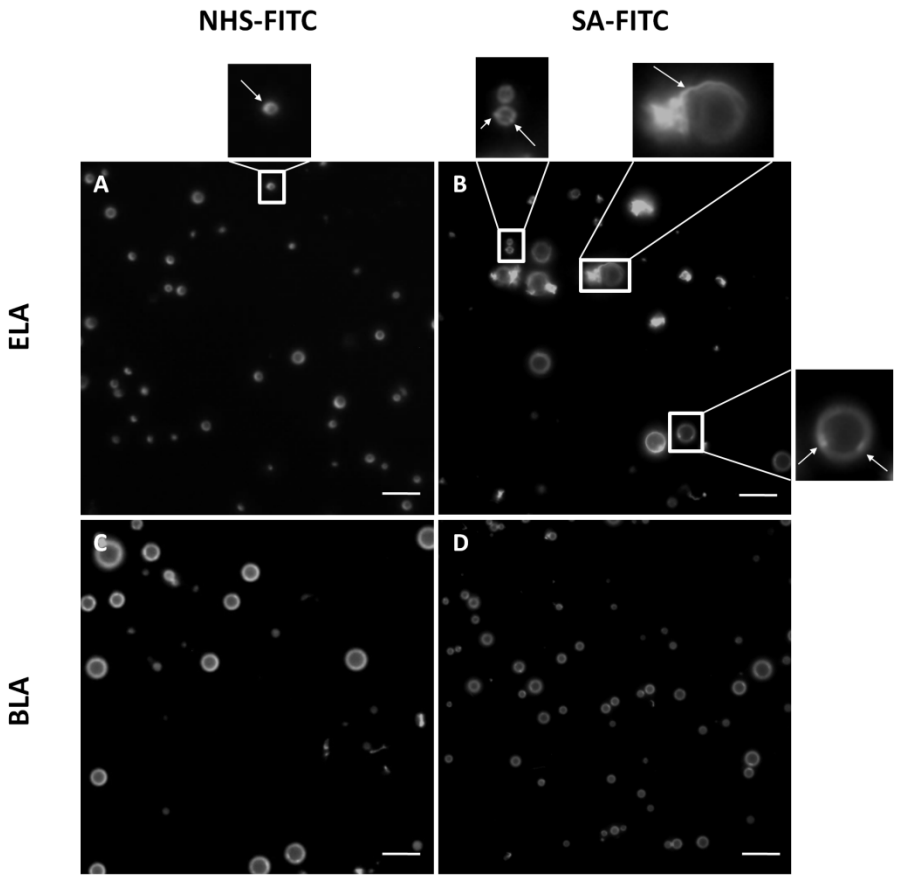

Figure 2.11. Epi-fluorescence images of microbubble samples after ligand binding. Arrows point to microstructural features of non-uniform FITC labeling. (A) NHS-FITC labeled ELA microbubbles. (B) NHS-FITC labeled BLA microbubbles. (C) SA-FITC labeled ELA microbubbles. (D) SA-FITC labeled BLA microbubbles. Scale bars correspond to 10 μm.

Surprisingly, during the preliminary screening for ligand saturation, it was noticed that the number of events (event%) that fell within the tight polydisperse P gate on the FSC versus SSC plot detected by flow cytometry stayed relatively constant for all microbubble samples

except for SA-FITC/ELA binding (Figure 2.12). A significant decrease of event% inside the gate was repeatedly observed immediately after SA-FITC binding to ELA microbubbles, and the relative change stayed constant throughout the 6 hr experiment. This change of event% was not accompanied by a corresponding decrease in total particle concentration (data not shown). Since SSC is a measure of particle granularity and texture (Traganos 1984), it was then hypothesized that this change of scattering property resulted from a change of microbubble surface structure.

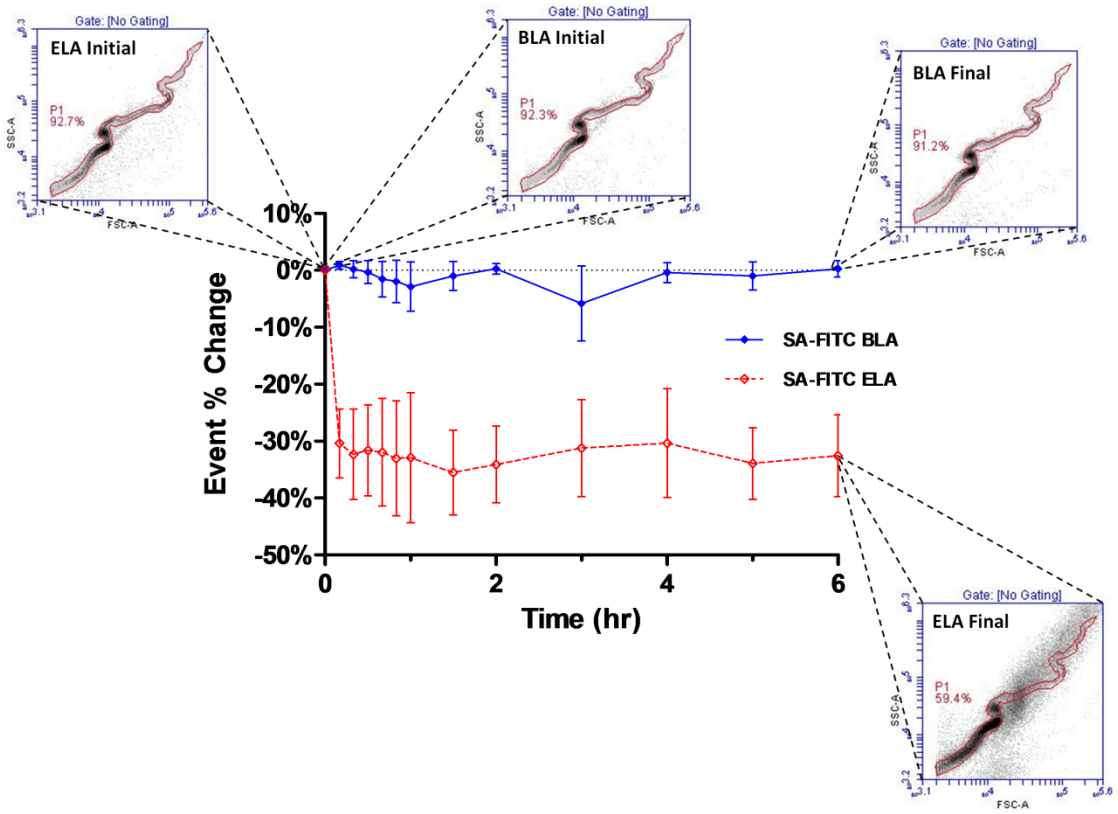

Figure 2.12. Flow cytometric identification of surface stractures induced by streptavidin binding. Shown is in the change in the percentage of events that fell within the serpentine P gate and the accompanying FSC versus SSC plots.

Epi-fluorescence images verified this hypothesis. Figure 2.11B (upper right) shows typical SA-FITC labeled ELA microbubbles exhibiting complex surface structure (e.g., folds, domains and protrusions) that were not normally found on either SA-FITC labeled BLA microbubbles or NHS-FITC labeled ELA microbubbles. Similar structures were found on almost all SA-FITC bound ELA microbubbles that were large enough (diameter >~3 μm) to be examined by optical microscopy. No visible changes, such as collapse, aggregate formation or vesicles shedding, were observed for these microbubbles over the observation time period (typically around 10-15 min).

The streptavidin-induced surface structures (folds and protrusions) were not observed for either SA-FITC labeled BLA microbubbles or NHS-FITC labeled ELA microbubbles, and they can be correlated to the flow cytometry measurement very closely (Figure 2.12). Figure 2.13 shows a cartoon concept of the streptavidin-induced surface structure. It is speculated that, during the early binding period, incomplete surface coverage of biotin moieties by the SA-FITC led to cross-linking between the monolayer shell and folds extending into the aqueous phase. (Small bilayer folds and protrusions were likely presented as defects in the microbubble shell prior to SA-FITC binding.) Furthermore, the cross-linking led to an effective spreading pressure of the bilayer fold over the monolayer surface, which pulled more lipids from the monolayer plane into the fold. As the spreading proceeded, a fold would grow until the SA-FITC molecules, which were the limiting reagent, were depleted or the SA-FITC molecules reached their maximum surface density. Fold nucleation and growth would likely be nucleated from shell heterogeneities and would induce gas dissolution from the core, consistent with results presented in Figure 2.11 and 2.12. This explanation was inspired by previous work done by others showing adhesion between apposing lipid vesicles induced by avidin-biotin interactions (Noppl

and Needham 1996; Nam and Santore 2007; Nam and Santore 2007). The avidin-biotin spreading pressure was able to bend and stretch the bilayer membranes to form large contact regions (e.g., plaques). Previous work done by Nam and Santore (Nam and Santore 2007) showed that the time scale for spreading in general was on the order of 1 second. For the present experiment, by the time the first data point was taken at 10 min, it is assumed that the growth and spreading of the folds and protrusions were completed and the system had reached a new equilibrium state.

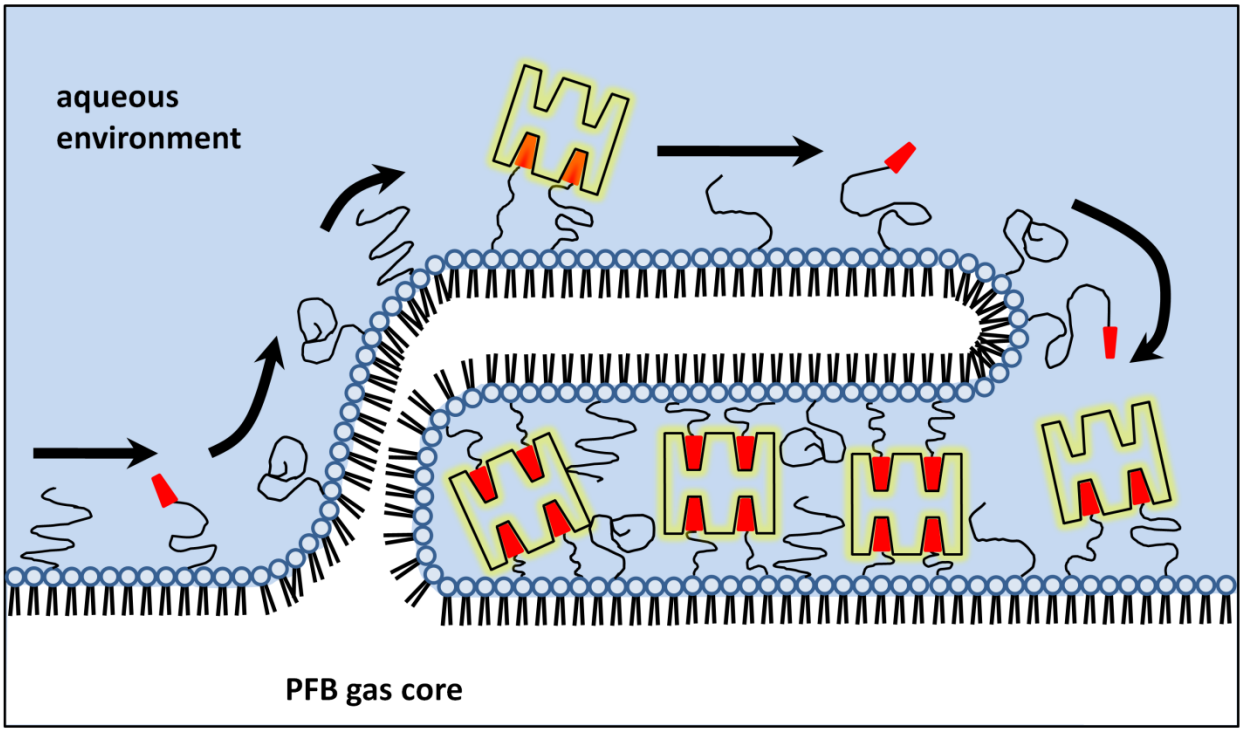

Figure 2.13. Cartoon illustrating possible streptavidin-induced monolayer protrusions.

In order to test the hypothesis that the formation of these surface structures was a streptavidin-biotin mediated phenomenon rather than a manifestation of gas core dissolution owing to dilution, the microbubble concentration change over the 6 hr experiment period was

plotted for each size range using the flow cytometry data (Figure 2.14). For ELA microbubbles binding to SA-FITC, all size ranges showed a significant decrease in concentration within the first 10 min and stayed constant throughout the rest of the experiment. For BLA microbubbles, on the other hand, none of the size ranges showed a significant change of concentration. Since both samples were prepared and diluted in the same manner, this result eliminated the possibility that the observed surface structures resulted simply from microbubble dissolution.

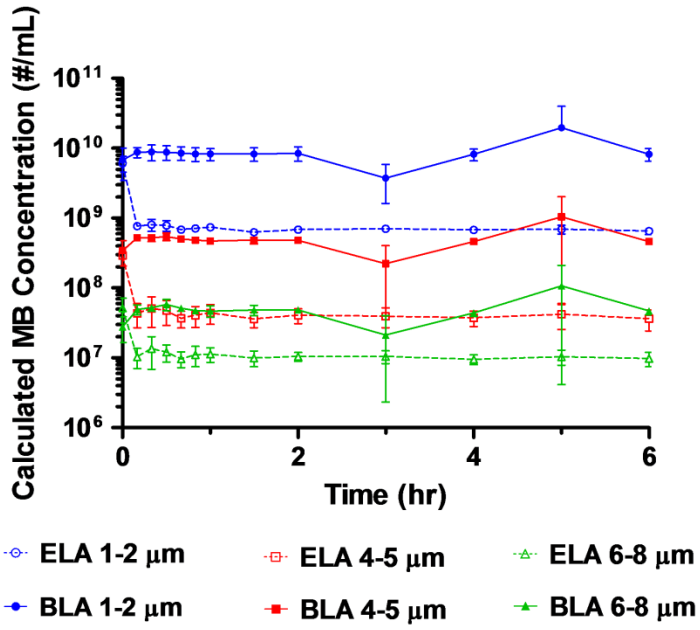

Figure 2.14. Concentration change for ELA and BLA microbubbles upon SA-FITC binding over 6 hr. Concentration data were obtained from flow cytometry data using the tight-fitted P gates.

The absence of the wrinkled structure observed for BLA microbubble could be due to the inhibited macromolecule diffusion into the bimodal PEG layer. The availability of the tethered biotin group in a bimodal PEG brush was much lower than that for the ELA counterpart. If there were not enough biotin-streptavidin interactions within a close proximity, the system may not

have been able to bend and stretch the monolayer enough to promote the growth of folds and protrusions.

While Rychak et al. (Rychak, Lindner et al. 2006) showed that they could use mechanical pressurization to create wrinkled microbubbles with increased surface area for loading targeting ligands and facilitating adhesion, a new method for inducing complex surface structure formation that resulted in similar folds and protrusions is presented in this study. The excess area of SA-FITC labeled ELA microbubbles may also stabilize specific adhesion. However, these surface structures may increase immunogenicity. Regardless, it was shown for the first time that these microbubble surface structures may be quantified using flow cytometry.

2.4. Conclusion

NHS-FITC and SA-FITC were used as model molecules to post-label ELA and BLA microbubbles. For small molecules, such as NHS-FITC, the diffusion and binding to the tethered amino end groups were not affected by the PEG overbrush in BLA microbubbles, and the overall binding rate between ELA and BLA microbubbles was the same. On the other hand, for macromolecules, such as SA-FITC, the diffusion and binding to the tethered biotin end groups were partially prevented by the PEG overbrush due to steric hindrances for BLA microbubbles, and the binding rate was significantly reduced. The total binding capacity for BLA microbubbles was significantly lower for macromolecules in comparison to the ELA counterpart (~58%), suggesting a possible phase separation between lipid species on the surface. These results proved the hypothesis that small molecules could diffuse through the excluded volume of PEG chains and react with surface functional groups while larger molecules were significantly inhibited. Post-labeling with BLA microbubbles is therefore highly feasible for

small ligands (<1 kDa) for generating targeted ultrasound contrast agents. In addition, the effect of microbubble size on ligand conjugation was investigated. It was shown that ligand conjugation was not affected by microbubble diameter regardless of the ligand size or microbubble surface architecture. A new way of introducing complex surface structures, or wrinkles, was also discovered through streptavidin conjugation to ELA microbubbles. It was proposed that the tight serpentine shape P gate and the event% parameter from the flow cytometry data can be used together with epi-fluorescence microscopy to detect these surface structures. Flow cytometry can give a quick quantitative indication of the percent of microbubbles in a given suspension that deviate from the normal spherical shape, while microscopy offers direct visual confirmation of the surface structure.

Chapter 3: The Role of Poly(ethylene glycol) Brush Architecture on *In Vitro* Complement Activation for Targeted Microbubbles

3.1. Introduction

For intravenously injected colloidal particles, such as ultrasound contrast agents, it is extremely important to ensure that they do not trigger any undesired immune response. The incorporation of the flexible PEG polymer chains in the microbubble shell is designed to reduce the immunogenicity of these contrast agents by physically preventing the diffusion and attachment of complement proteins or antibodies to the microbubble surface in a similar fashion as for Stealth Liposomes. However, recent studies have suggested that PEGylated liposomes are capable of triggering the complement system in human serum and fixing opsonic complement proteins (Moghimi and Szebeni 2003; Szebeni 2005; Moghimi, Hamad et al. 2006; Moghimi and Hamad 2008). In addition, decorating microbubbles with targeting ligands could further present chemical groups that bind to complement C3 proteins and trigger CARPA. Clearly, avoidance of an immunogenic response is desirable for targeted microbubbles, not only to minimize hypersensitivity reactions, but also to enable long circulation persistence for accumulation at the target site. Ideally, the targeting ligand would be hidden from the milieu until the microbubble reaches the region of interest, where it is exposed for binding via multiple ligand-receptor interactions that result in firm adhesion.

Microbubbles with the buried-ligand architecture may just offer the perfect solution for this issue. As explained in the previous chapters, the targeting ligands are attached to the shorter PEG chains, and are buried in a longer PEG overbrush from exposing to the surrounding environment until reaching to the target site during circulation. Because of the unique oscillation

property of microbubbles (expansion and contraction in response to an ultrasound field), the targeting ligands would only be revealed for adhesion during the acoustic pulse, and re-shielded at the end of each ultrasound cycle. This stealth microbubble design has been shown to facilitate selective adhesion in combination with USRF without compromising binding specificity. In an attempt to further experimentally test the effect of the PEG brush architecture on microbubble immunogenicity, microbubbles with various surface architectures were generated (Figure 3.1). Instead of using a pre-synthesized lipoprotein-peptide conjugate as one of the shell components, a post-labeling technique was utilized to conjugate RGD peptides to the tethered PEG chains after microbubble generation and isolation. It has been demonstrated in the previous chapter that small molecules, such as the RGD peptide with its molecular weight <1 kDa, could diffuse freely through the PEG overbrush and bind to the tethered functional groups to generate targeted contrast agents. In the present chapter, microbubbles with various PEG brush architectures were tested for immunogenicity *in vitro*. By quantifying the amount of complement C3/C3b binding to the microbubbles after human serum incubation, evidence was shown that the buried-ligand design indeed decreased microbubble immunogenicity. These findings further supported the utilization of the buried-ligand architecture to future designs of biocolloids as molecular imaging agents and drug delivery carriers.

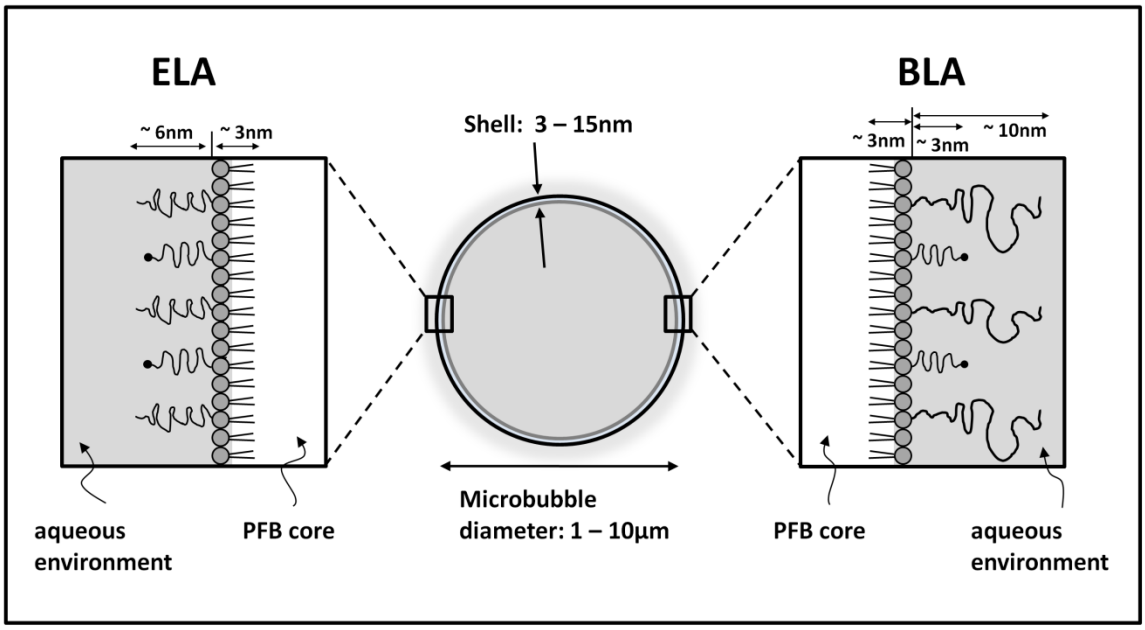

Figure 3.1. Cartoon illustrating microbubble surface architecture design for *in vitro* immunogenicity studies. The PEG chain length was estimated using self-consistent field (SCF) theory (Lai and Zhulina 1992) as mentioned in Chapter 2.

3.2. Materials and Methods

3.2.1. Materials

All phospholipids were purchased from Avanti Polar Lipids, Inc. (Alabaster, AL), including 1,2-distearyol-sn-glycero-3-phosphocholine (DSPC), 1,2-distearyol-sn-glycero-3-phosphoethanolamine-N-[methoxy(polyethylene glycol)2000] (DSPE-PEG2000), 1,2-distearyol-sn-glycero-3-phosphoethanolamine-N-[maleimide(polyethylene glycol)2000] (DSPE-PEG2000-M), 1,2-distearyol-sn-glycero-3-phosphoethanolamine-N-[methoxy(polyethylene glycol)3000] (DSPE-PEG3000) and 1,2-distearyol-sn-glycero-3-phosphoethanolamine-N-[methoxy(polyethylene glycol)5000] (DSPE-PEG5000). All phospholipids were dissolved in chloroform (Sigma-Aldrich; St. Louis, MO) and stored in the freezer at -20 ^{o}C. The perfluorobutane gas (PFB, 99 wt% purity) used for microbubble generation was purchased from

FluoroMed, L.P. (Round Rock, TX). The RGD peptide (cyclo [Arg-Gly-Asp-D-Phe-Cys], 99.9% purity) was purchased from Peptides International (Louisville, KY) and was dissolved in 3 vol% degassed acetic acid (Sigma-Aldrich). The dissolved RGD peptide was aliquoted into 50-μL volume and stored in nitrogen at -20 °C. The L-cysteine was purchased from Sigma-Aldrich and was dissolved in 18 MΩ-cm filtered deionized water (Direct-Q Millipore; Billerica, MA). The L-cysteine solution was prepared on each day immediately before use to ensure reactivity.

Human complement-preserved serum was purchased from Valley Biomedical (catalog no. HC1004; Winchester, VA). Serum was thawed once to aliquot into 1-mL eppendorf tubes and stored at -80 °C. Anti-human IgG-FITC antibody (catalog no. F4512) was purchased from Sigma-Aldrich. Both anti-human albumin-FITC antibody (catalog no. CLFAG2140) and anti-human C3/C3b-FITC antibody (catalog no. CL2103F) were purchased from Cedarlane (Burlington, NC). All antibody solutions were stored at 4 °C.

3.2.2. Microbubble Generation and RGD Peptide Conjugation

The compositions of microbubble samples are listed in Table 3.1. Microbubbles were generated as described in Chapter 2 and elsewhere (Feshitan, Chen et al. 2009). Briefly, the indicated amounts of each phospholipid species were mixed, and the chloroform was evaporated. The dried lipid film was hydrated with phosphate buffered saline (PBS) mixture (90 vol% PBS:10 vol% 1,2-propanediol:10 vol% glycerol; Sigma-Aldrich) to a final lipid/surfactant concentration of 1 mg/mL. Fully dispersed lipid suspension was then transferred to a 3-mL serum vial and sealed for headspace PFB gas exchange. Microbubbles were formed by shaking with a VialMix (ImaRx Therapeutics; Tucson, AZ) for 45 s. The generated microbubbles were then diluted to 10-mL suspension with PBS, and washed 3 times by centrifugation flotation in a

bucket-rotor centrifuge (Model 5804, Eppendorf; Westbury, NY) at 250G for 5 min. The microbubble cake was then diluted in 5 mM EDTA (pH 6.5) for subsequent experiments.

Table 3.1. Microbubble compositions for *in vitro* immunogenicity studies

	Phospholipid Composition (mol %)				
Samples	DSPC	DSPE-PEG2000	DSPE-PEG2000-M	DSPE-PEG3000	DSPE-PEG5000
ELA-P2K Control	90	10	-	-	-
ELA-P5K Control	90	-	-	-	10
ELA 5%	90	5	5	-	-
ELA 0.5%	90	9.5	0.5	-	-
ELA 0.05%	90	9.95	0.05	-	-
BLA-P2K/P5K Control	90	5	-	-	5
BLA 5%	90	-	5	-	5
BLA 0.5%	90	4.5	0.5	-	5
BLA 0.05%	90	4.95	0.05	-	5
BLA-P3K 5%	90	-	5	5	-

An Accusizer optical particle counter (NICOMP Particle Sizing System; Santa Barbara, CA) was used to measure the size distribution and particle concentration. The amount of RGD peptide needed was then calculated as described in the previous chapter. RGD peptide was added to react with maleimide functional groups on the distal end of PEG chains at a molar ratio of 30:1 (RGD:maleimide). The reaction was carried out on a benchtop rotator for 12 hours at 4 ^{o}C. To ensure there were no unreacted maleimide groups, L-cysteine was added at a molar ratio of 1000:1 (L-cysteine:maleimide) after regular RGD peptide conjugation. The sample was incubated on a benchtop rotator for 30 min at room temperature. Unreacted RGD peptide was removed by centrifuging the microbubble suspension at 250G for 4 min. The concentrated microbubble cake was then re-suspended in PBS and analyzed by Accusizer. The median

fluorescence intensity was measured using an Accuri C6 flow cytometer (Accuri Cytometers Inc.; Ann Arbor, MI). For zeta potential measurement, the washed microbubble cake was re-suspended in pH adjusted PBS solution (pH 7.2) and analyzed using a Malvern Zetasizer Nano-ZS (Malvern Instrument Ltd.; Worcestershire, UK).

3.2.3. HPLC Analysis of RGD Coupling to Microbubbles

RGD peptide conjugation was confirmed using HPLC and MALDI-TOF as reported elsewhere (Nallamothu, Wood et al. 2006; Liu, Ruan et al. 2010). Two ELA microbubble samples were made: one with 1:1 RGD:maleimide molar ratio and one with 30:1 RGD:maleimide molar ratio, following the same procedure as described above. No L-cysteine was added to cap the unreacted maleimide groups at the end of the coupling reaction. Upon reaction completion, the microbubble suspensions were sonicated at 60 °C for 30 min using a bath sonicator (model 1510, Branson Ultrasonics; Danbury, CT) until the lipids were completely dispersed in solution. HPLC injection samples were directly taken from the reaction vial without further filtering to ensure no RGD peptide was lost during handling. The 30:1 molar ratio microbubble sample was diluted according to calculation using deionized water prior to HPLC analysis.

The attachment of RGD peptides to the microbubble surface was ascertained indirectly by determining non-coupled peptide fraction using HPLC. A Nova-Pak C_{18} column (4 µm, 3.9 x 50 mm, Waters; Milford, MA) was used with a mobile phase consisting of 0.05% trifluoroacetic acid (TFA) in water (eluant A) and 0.05% TFA in acetonitrile (eluant B). The eluant gradient was set from 10% to 60% B in 50 min and subsequently back to 10% B over 5 min. Flow rate was set to 1 mL/min. The column was equilibrated for at least 10 min with 90% A and 10% B

between measurements. The uncoupled RGD peptide was detected by measuring absorbance at 214 nm. The detected peaks were collected for MALDI-TOF mass spectrometry analysis.

3.2.4. MALDI-TOF Mass Spectrometry Analysis of HPLC Sample Peaks

The samples for the MALDI-TOF experiment were first freeze-dried and resuspended in 5 µL 20% acetonitrile in water containing 10% TFA. 0.5 µL of the resulting solution was mixed with 2.5 µL of nitrogen saturated matrix solution. The matrix solution was made by dissolving 35 mg α-cyano-4-hydroxycinnamic acid in 0.8 mL of 50% acetonitrile in water containing 1% TFA. 2 µL of this mixture solution containing the HPLC sample was spotted on a stainless steel sampling plate and allowed to air dry. The MALDI-TOF measurement was carried out on a Voyager-DE BioSpectrometry Workstation (PerSeptive Biosystems; Framingham, MA) with linear positive model. The main instrumental settings were made manually, with typical voltage being 25,000 V, grid being 95 and delay time being 100 ns.

3.2.5. Human Complement-Preserved Serum C3/C3b Activity Assay

Serum aliquots were randomly chosen from each batch to test for complement component C3/C3b activity at different time points throughout the entire immunogenicity study. C3/C3b activity was measured using an ELISA kit purchased from Assaypro (catalog no. EC2101-1) following the manufacturer's instruction. No serum was re-frozen after ELISA assay to ensure complement activity.

3.2.6. Microbubble Serum Stability Analysis

1 mL serum was preheated in a water bath at 37 °C using a digital block heater (VWR; West Chester, PA) for at least 20 min. A total of $5x10^8$ RGD-conjugated microbubbles were added to the serum, and the size distribution and microbubble concentration was continuously monitored for 2 hr at 37 °C using both Accusizer and flow cytometer. The same amount of sample (6 μL for Accusizer and 4 μL for flow cytometry) was taken out at different time points for measurement to ensure consistency. Incubated samples were vortexed regularly to prevent microbubble aggregation at the top of the serum. Flow cytometry size isolated gating was used for data analysis as described in the previous chapter.

3.2.7. Microbubble Antibody Binding Analysis

A total of $5x10^8$ microbubbles (about 100 μL in volume) were incubated with 900 μL serum on a benchtop rotator for 2 hr at room temperature. The sample was then washed once by centrifugation floatation at 250G for 3 min. The concentrated microbubble cake was re-suspended in 100 μL PBS solution and analyzed by both the Accusizer and flow cytometer. For anti-human C3/C3b, anti-human IgG and anti-human albumin FITC-antibody binding, 5 μg antibody was added. All FITC-antibody binding experiments were carried out in the dark on a benchtop rotator for 1 hr at room temperature. At the end of the incubation period, the microbubble sample was again analyzed by flow cytometry and microscopy without washing. The measured median fluorescence intensity data was analyzed according to microbubble diameter using size-isolated microbubble gating information as described in the previous chapter.

3.2.8. Optical Microscopy

Direct visual confirmation of microbubble fluorescence was performed within 24 hrs after FITC antibody binding. Microbubble samples were taken out of the reaction syringe and imaged at room temperature. Still images were taken using an Olympus 1X71 inverted microscope (Olympus; Center Valley, PA). Images in both bright field and epi-fluorescence mode were captured for the same field of view using a high-resolution digital camera (Orca HR, Hamamatsu; Japan) with a 100x oil immersion objective and processed with Simple PCI software (C-Imaging; Cranberry Township, PA). Subsequent image analysis was done using ImageJ 1.4g software (NIH; Washington DC.).

3.3. Results and Discussion

3.3.1. Targeted Microbubble Generation

For each set of microbubble components, the vial shaking method produced a milky, white microbubble suspension that was stable over the experimental timeframe. It has been shown in the previous chapter that small ligands with molecular weight < 1 kDa, such as RGD peptides, could diffuse freely through the PEG overbrush and react with functional groups at the distal end of buried PEG chains. Here, HPLC and MALDI-TOF were used to ensure the complete attachment of RGD peptides to the surface of BLA microbubbles using the post-labeling technique (see below). Since several factors, such as microbubble size and surface charge, could influence the interactions between microbubbles and serum antibodies, the physicochemical properties of the samples were examined (Table 3.2). Microbubble samples were matched in concentration after the RGD conjugation and/or washing steps. We measured

similar size distributions for all samples, with a dominant peak between 1 and 2 μm and a secondary peak between 4 and 5 μm (Figure 3.2A and 3.2B). The conjugation of RGD peptide to the surface of microbubbles did not affect either the microbubble size distribution or concentration. The number-weighted mean diameters for all microbubble samples were found to be similar, while the volume-weighted mean diameters ranged between 4.7 and 8.2 μm. Measurement of zeta potential showed that the negative charge of P2K microbubbles tended to increase by the conjugation of RGD peptide at pH 7.2. At the same time, the addition of the PEG overbrush (DSPE-PEG5000) into the microbubble shell tended to neutralize this negative charge.

Table 3.2. Microbubble physicochemical properties

Samples	Initial Concentration (#/mL) (Mean)	Number-Weighted Mean Diameter (μm) (Mean ± SD)	Volume-Weighted Mean Diameter (μm) (Mean ± SD)	Zeta Potential (mV) (Mean ± SD)
ELA-P2K Control	5.19E+09	1.3 ± 0.0	5.4 ± 0.6	-24.1 ± 1.7
ELA-P5K Control	4.19E+09	1.4 ± 0.1	6.7 ± 2.0	-9.50 ± 2.1
ELA 5%	4.59E+09	1.4 ± 0.1	8.2 ± 2.1	-38.9 ± 2.8
ELA 0.5%	6.10E+09	1.4 ± 0.0	6.9 ± 0.8	-31.4 ± 0.9
ELA 0.05%	5.29E+09	1.3 ± 0.0	6.8 ± 0.4	-30.0 ± 1.1
BLA-P2K/P5K Control	5.89E+09	1.4 ± 0.1	4.8 ± 0.8	-12.0 ± 0.6
BLA 5%	4.83E+09	1.4 ± 0.1	5.2 ± 0.7	-19.2 ± 0.3
BLA 0.5%	6.57E+09	1.5 ± 0.1	6.8 ± 0.6	-14.6 ± 0.8
BLA 0.05%	6.78E+09	1.4 ± 0.1	7.0 ± 3.2	-12.5 ± 1.7
BLA-P3K 5%	4.63E+09	1.3 ± 0.0	4.7 ± 0.3	-37.6 ± 0.2

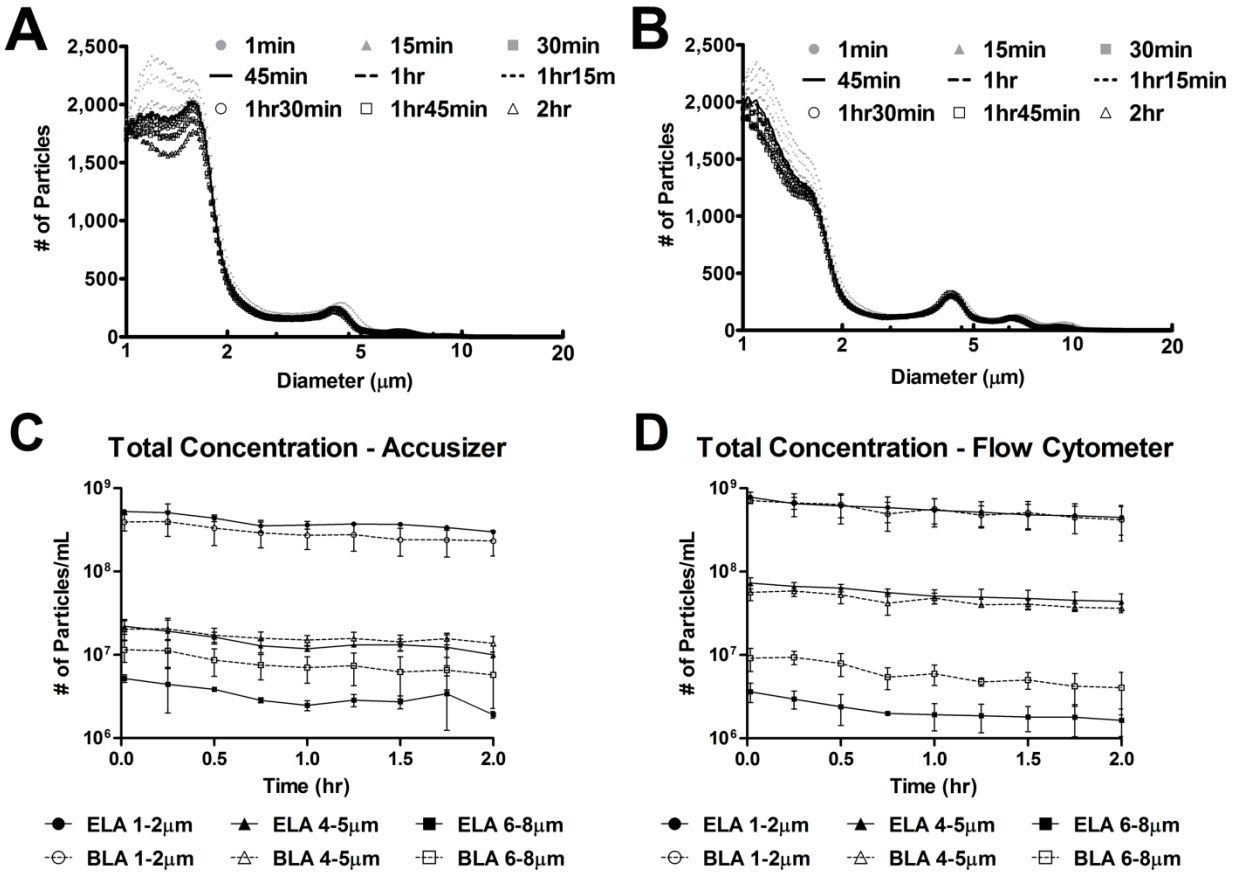

Figure 3.2. 5% RGD peptide labeled microbubble size distribution (A, B) and concentration (C, D) change during human complement-preserved serum incubation at physiological condition. The size distribution was continuously monitored for 2 hrs for both ELA (A) and BLA (B) microbubble samples. With the exception that some smaller microbubbles (diameter <2 μm) showed a decrease in number detected over time, the majority of targeted microbubbles were stable during incubation with no significant change in size. The total concentration, as measured by Accusizer (C) and flow cytometer (D), was plotted against time according to microbubble diameter ranges. Both techniques showed data in good agreement; even though a concentration decrease was observed for both designs at the end of 2-hr incubation time, more than 70% of the targeted microbubbles were stable at 30 min, which was in the same time scale as for a typical ultrasound contrast imaging session.

3.3.2. HPLC Analysis of RGD Coupling to Microbubbles

An HPLC method was adapted to determine the extent of coupling of the RGD peptide to the microbubbles as previously described (Nallamothu, Wood et al. 2006; Liu, Ruan et al. 2010). The method involved detecting the amount of free RGD left in the microbubble suspension after the coupling reaction. Standard RGD peptide dissolved in the mobile phase eluted at about 8-min retention time (P1) as shown in Figure 3.3A. This peak was monitored as the standard for the estimation of free RGD in the final microbubble formulations.

The reacted microbubble samples were injected to determine the extent of the coupling reaction. To ensure the accuracy of a negative detection of the free RGD peak was due to the complete coupling reaction, rather than an instrumental sensitivity issue, the injection volume for each microbubble sample was calculated so that the amount of RGD peptide would be the same (1 μg RGD/injection) assuming no reaction took place. As shown in Figure 3.3B, there was no significant peak for the free RGD around 8 min, indicating that there was no considerable amount of free RGD peptide left unreacted in the 1:1 molar ratio sample.

It was hypothesized that bound RGD to DSPE-PEG2000-M would give a different retention time than the free RGD peptide. Figure 3.3C shows the HPLC spectrum of the 30:1 molar ratio microbubble sample with known excess amount of free RGD peptide presented in solution (positive control). As expected, the free RGD peak was observed at about 8-min retention time again, confirming the sensitivity of this analysis method to detect free RGD in the presence of RGD-lipid conjugates.

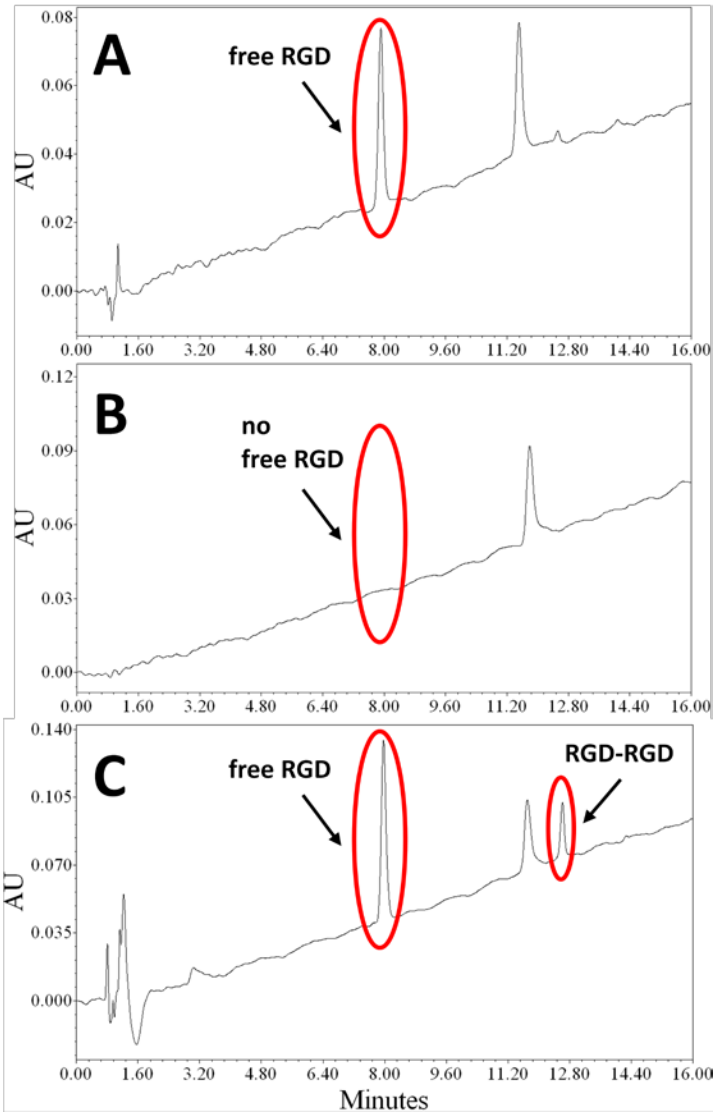

Figure 3.3. HPLC analysis confirming RGD coupling to microbubbles. (A) Standard RGD peptide injection showed free RGD had an around ~8-min retention time. This peak was used as the standard for all subsequent injections to confirm the completion of the RGD-microbubble coupling reaction. P2 (11-min retention time) was confirmed using MALDI-TOF to be impurities presented in the sample. (B) 1:1 molar ratio microbubble sample showed no free RGD peak at 8 min, indicating that all RGD peptides were conjugated to the microbubble surface. (C) 30:1 molar ratio microbubble sample (positive control) showed free RGD peak at 8 min, confirming the sensitivity of the analysis method to detect free RGD in the presence of RGD-lipid conjugates. P3 (13-min retention time) was confirmed using MALID-TOF as cross-linked RGD peptides.

3.3.3. MALDI-TOF Mass Spectrometry Analysis of HPLC Sample Peaks

Two additional peaks were detected on the HPLC spectra: one at ~11-min retention time (P2) and one at ~13-min retention time (P3) (Figure 3.3). MALDI-TOF analysis was done in order to delineate these peaks from the free RGD peak (Figure 3.4). Figure 3.4A confirms that P1 was indeed the free RGD peptide. Some cross-linking between RGD peptides was detected, which may occur during sample handing post RGD-microbubble coupling reaction. P2 showed an unknown sample mass at around 700 m/z, which could be PBS salts or impurities presented in the microbubble samples (Figure 3.4B). P3 contained both impurities and double-linked RGD peptides, which suggested that cross-linking of the RGD peptides occurred during the coupling reaction (Figure 3.4C).

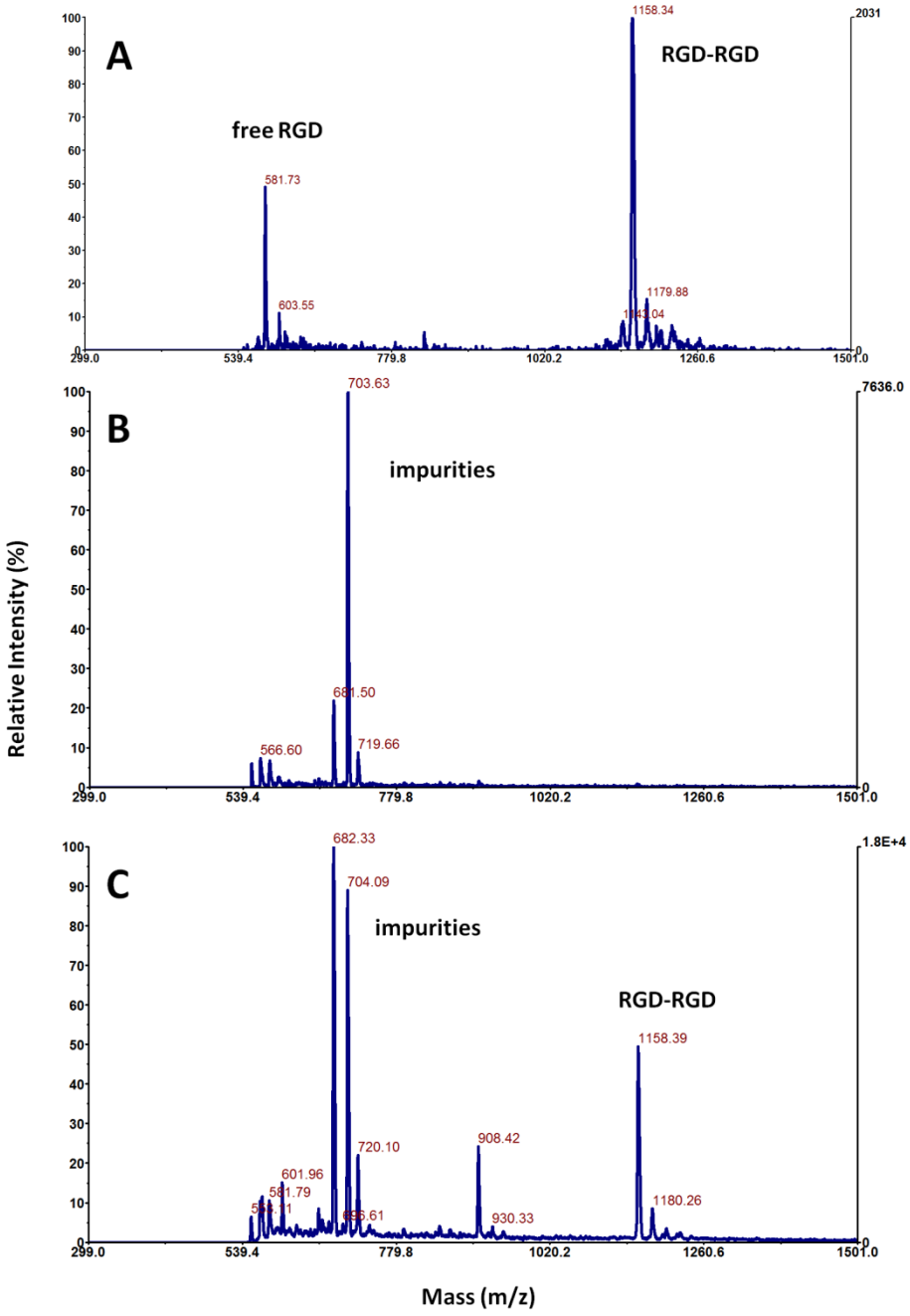

Figure 3.4. MALDI-TOF mass spectrometry results confirming the identities of HPLC sample peaks. (A) P1 was confirmed as free RGD. Some cross-linking between RGD peptides occurred shown as the doubled mass peak at around 1158 m/z. (B) An unknown sample mass was detected in P2, which suggested to be either PBS salts or impurities presented in the microbubble samples. (C) P3 was confirmed as the cross-linked RGD product.

3.3.4. Microbubble Serum Stability

The stability of microbubbles with 5% RGD peptide during incubation in human serum at physiological temperature was investigated. Figure 3.2A and 3.2B shows the size distribution change for ELA and BLA microbubbles, respectively, during the 2-hr incubation as measured by the Accusizer. For both surface architectures, smaller microbubbles with diameter less than 2 μm showed a decrease in number detected over time, while larger microbubbles showed no significant change. The total microbubble concentration change was monitored using both the Accusizer and the flow cytometer (Figure 3.2C and 3.2D). Both detection methods showed results that were in good agreement: a decrease in microbubble concentration was observed for both surface architectures at all size ranges at the end of 2 hrs, with the highest decrease being 59% and 53% for ELA and BLA 6-8 μm microbubbles, respectively. However, the concentration decrease for all microbubble samples after 30 min incubation ranged from only 11% to 30%. Based on these results, it is concluded that targeted microbubbles, regardless of surface architecture, were stable in human serum during incubation at physiological temperature within the time scale for a typical ultrasound contrast imaging session (~30 min) (Borden, Zhang et al. 2008).

3.3.5. Human Serum Factor Binding to Microbubbles

It has been reported that the concentration of serum strongly affects activation of the complement system (Toda, Kitazawa et al. 2008). Therefore, undiluted complement-preserved human serum was used for all experiments. To ensure the validity of the immunogenicity data, complement activity of the serum samples was continuously monitored by measuring complement component C3/C3b activity of randomly chosen serum aliquots throughout the

study. Figure 3.5 shows the quantified C3/C3b activity as measured by ELISA assay for all 38 samples. The measured C3/C3b activity was 30 ± 16 μg/mL of serum (mean ± SD). The human serum samples from different batches were statistically identical in terms of complement C3/C3b activity, and the aliquots were stable for the duration of the experiments. By showing consistent complement activity, it is ensured that any measured C3/C3b binding difference in the immunogenicity study was due to the difference in complement activation by various microbubble samples, not due to batch-to-batch variability in serum C3/C3b activity.

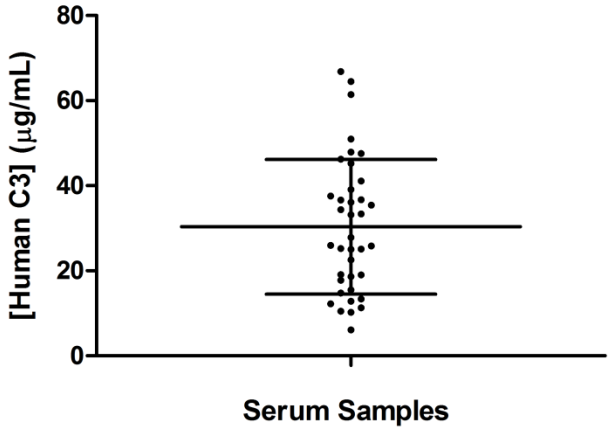

Figure 3.5. ELISA results of complement component C3/C3b activity for human complement-preserved serum aliquots. Serum aliquots were randomly chosen to be tested throughout the immunogenicity experiments. The average of measured C3/C3b activity was 30 ± 16 μg/mL of serum (mean ± SD). The human serum samples from different batches were statistically identical in terms of complement C3/C3b activity.

Next, the binding of human complement component C3/C3b, IgG and albumin to targeted microbubbles with 5% RGD conjugated to the surface was investigated. Sufficient

incubation time (2 hr) was given to allow the full exposure of microbubbles to the serum environment. Detection of fluorescent antibodies by flow cytometry allowed an assessment of serum factor binding to the microbubble shells. Figure 3.6 shows the median fluorescence intensity (MFI) values for 1-2 μm ELA and BLA microbubbles after incubation with human serum and FITC-antibodies. The 1-2 μm size range was chosen because these microbubbles were the most abundant in all the samples and could correctly represent the MFI trend for the entire population. All three serum factors were detected on the targeted microbubble samples. However, increases in MFI for IgG and albumin were small (<10%) compared to C3/C3b binding to ELA and BLA microbubbles (3.8-fold and 1.3-fold increase, respectively). It was therefore concluded that complement C3/C3b was the main opsonin involved with the recognition of targeted microbubbles by the immune system.

Epi-fluorescence microscopy images provided direct visual confirmation of FITC-antibody binding to the surface of targeted microbubbles. Only anti-human C3/C3b FITC-antibody labeled targeted ELA microbubbles were visible under epi-fluorescence mode. Figure 3.7 shows both the bright field and epi-fluorescence images for the same field of view of these polydisperse microbubbles. All microbubbles appeared to be stable during observation. No visible changes, such as collapse, aggregate formation or vesiculation were observed for these microbubbles over the observation time period (typically around 10-15 min). Almost all microbubbles visible under the bright field mode were also seen under the epi-fluorescence mode, indicating FITC-antibody binding to the surface. There was no preferential binding due to microbubble size. However, non-uniform FITC-antibody attachment was observed (see enlarged images), indicating heterogeneous binding of complement C3/C3b.

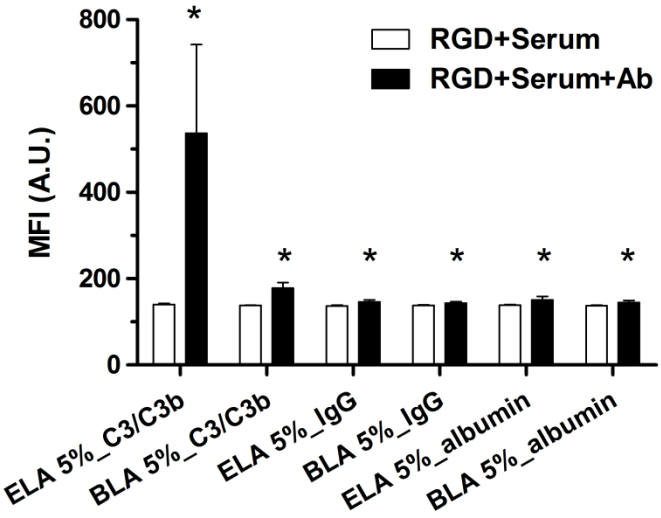

Figure 3.6. Human serum factor binding to 5% RGD peptide labeled 1-2 μm microbubbles. The median fluorescence intensity (MFI) was measured after RGD peptide conjugation, after 2 hrs human serum incubation and after 1 hr anti-human serum factor FITC-antibodies incubation. All three serum factors were observed to bind to both targeted microbubbles. However, only complement C3/C3b showed significant MFI increases (>284%); while IgG and albumin showed much less binding (maximum MFI increase was <29%). "*" denotes a significant increase vs. the corresponding "RGD+Serum" measurement ($p<0.05$).

Using streptavidin-FITC as model ligand, it was previously shown that the PEG overbrush does not completely eliminate macromolecule conjugation to the surface of microbubbles, suggesting the existence of two distributions of PEG-lipid conjugates on the microbubble surface (see Chapter 2). In the present study, a small amount of C3/C3b binding to BLA microbubbles was observed, lending further support to our suggestion that such non-uniform distributions of lipid molecules in the microbubble shell (e.g., domains and folds) may

yield incomplete shielding of the targeting ligands. The heterogeneous fluorescence observed on the shell was another indication of the existence of such microstructural features (Figure 3.7).

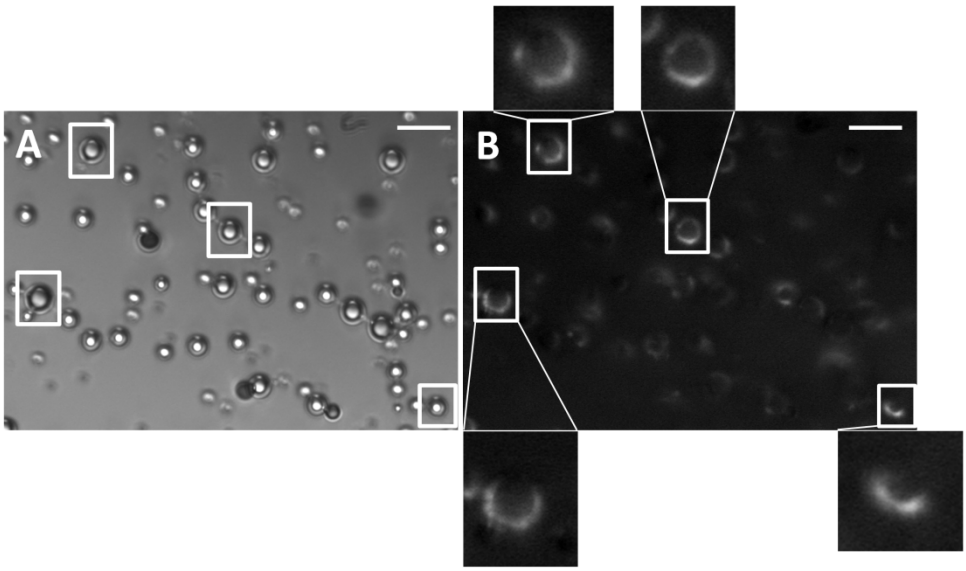

Figure 3.7. Microscopic images of 5% RGD labeled ELA microbubbles after C3/C3b binding in both bright field (A) and epi-fluorescence (B) mode. Both images show the same field of view. Enlarged images indicate microstructural features of non-uniform C3/C3b binding. Scale bars correspond to 10 μm.

3.3.6. Human Serum Complement C3/C3b Binding to Control Microbubbles

Control microbubbles without RGD peptide were first tested for immunogenicity after human serum incubation (Figure 3.8). Three different surface architectures were studied. Significantly lower MFI values were detected for P2K/P5K control than those for P2K control in all microbubble size classes. P5K control microbubbles showed the lowest MFI among all three

control samples. For the same methoxy DSPE-PEG surface coverage, the MFI for P5K control 4-5 μm and 6-8 μm microbubbles was only 36% and 31%, respectively, of those for their corresponding P2K control groups. These data suggest that some complement C3/C3b may be binding to the underlying phospholipid as well, and that the longer PEG reduces this effect (Moghimi, Hamad et al. 2006).

It is commonly accepted that water-soluble, nonionic PEG can protect colloidal particles, such as microbubbles and liposomes, from aggregation and macromolecule adsorption due to the steric hindrance effect of the polymer brush; each PEG chain forms an impermeable "cloud" over the surface because of its large excluded volume, which inhibits most macromolecules from diffusing into the brush layer. Here, evidence is shown to further support this conclusion: the incorporation of DSPE-PEG5000 into the microbubble shell forced the PEG chains to extend further away from the surface than either the DSPE-PEG2000 alone or the DSPE-PEG2000/5000 mixture, therefore forming a thicker and denser protective layer against complement protein adsorption.

For a given architecture, an increase in complement C3/C3b fixation with microbubble size was observed (Figure 3.8). The increase in MFI was found to be proportional to microbubble surface area, indicating that the surface density of C3/C3b was independent of microbubble diameter. This result was consistent across all microbubble samples, including those with RGD targeting ligands (see below). In addition to the higher total complement fixation, the larger microbubbles could also render them more susceptible to splenic clearance, possibly resulting in shorter circulation persistence. Interestingly, our group previously found that the echoes from untargeted 6-8 μm microbubbles persisted much longer in the mouse kidney

than their 1-2 μm or 4-5 μm counterparts, suggesting other mechanisms, such as gas core dissolution, may be at play (Sirsi, Feshitan et al. 2010).

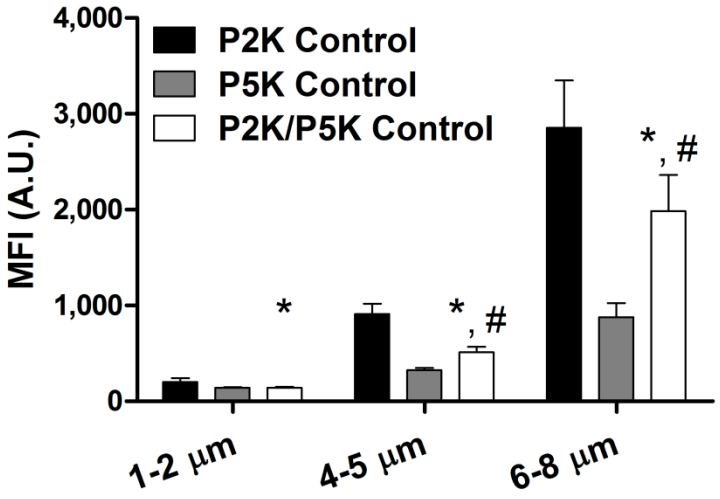

Figure 3.8. Human complement C3/C3b binding to control microbubbles. P2K/P5K control microbubbles showed significantly lower C3/C3b binding than P2K control in all microbubble size ranges. P5K control microbubbles showed the lowest amount of C3/C3b binding, suggesting a thicker and denser protective layer was formed by the DSPE-PEG5000 chains than either DSPE-PEG2000 or DSPE-PEG2000/5000 mixture. "*" denotes a significant difference vs. the corresponding P2K control, and "#" denotes a significant difference vs. the corresponding P5K control ($p<0.05$).

3.3.7. Effect of RGD Ligand Surface Density

The complement fixation on targeted microbubbles was tested next. Figure 3.9 shows the dependence of complement C3/C3b binding on RGD peptide surface density. Targeted ELA

microbubbles showed more C3/C3b binding than targeted BLA microbubbles for all RGD peptide surface coverages. For targeted ELA microbubbles, as the amount of conjugated RGD peptide increased, the binding of C3/C3b increased accordingly, indicating a correlated immune response (Figure 3.9A). Complement binding was linearly dependent on microbubble surface area, and the slope (change of MFI per μm^2) increased as the RGD surface density increased. However, this trend was not seen for targeted BLA microbubbles. For each size class, the MFI did not increase significantly even when the amount of conjugated RGD peptide was increased by two orders of magnitude (Figure 3.9B). These results agreed with the previous findings that the buried-ligand architecture protects the targeting ligands by inhibiting the adsorption of macromolecules to the microbubble surface (See Chapter 2). Since the extent of opsonization dictates the degree of complement activation, we conclude that BLA microbubbles triggered less immune recognition than their ELA counterparts.

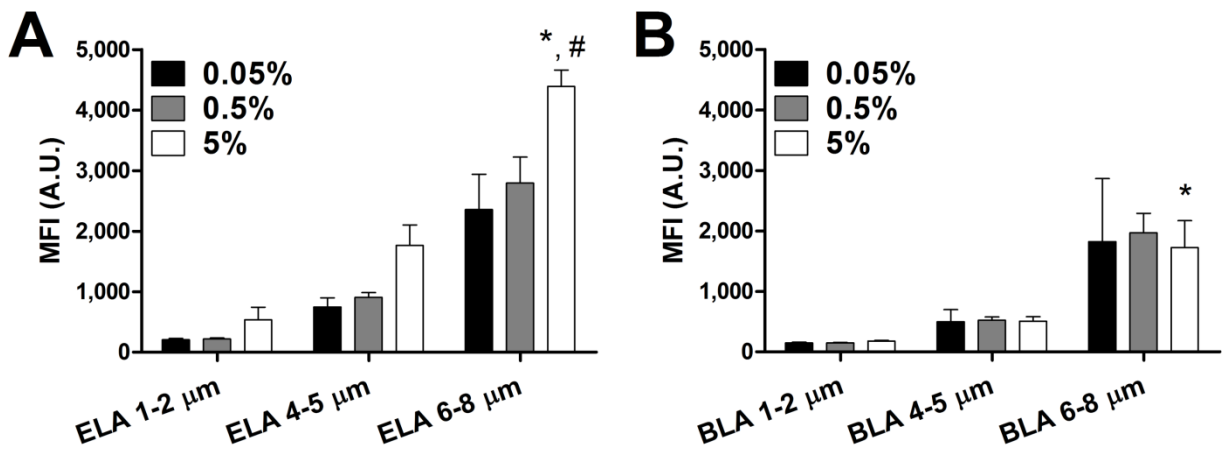

Figure 3.9. RGD surface coverage and size dependence of complement C3/C3b binding to targeted ELA (A) and BLA (B) microbubbles. For ELA microbubbles, higher RGD surface coverage led to more complement C3/C3b binding. But for BLA microbubbles, the PEG overbrush successfully protected the RGD peptide; no significant increase of MFI values was detected when the RGD conjugation amount was increased by two orders of magnitude. For both surface architectures, large targeted microbubbles (6-8 μm) showed significantly higher C3/C3b binding than smaller ones (1-2 μm and 4-5 μm), possibly due to the higher amount of RGD peptide presented on the surface. "*" denotes a significant increase vs. the corresponding 4-5 μm sample with 5% RGD, and "#" denotes a significant increase vs. the corresponding 6-8 μm sample labeled with 0.5% RGD ($p<0.05$).

To further investigate the role of targeting ligand presentation on human complement C3/C3b binding, MFI values were compared for targeted and control microbubbles with the same surface PEG brush layer configurations (Figure 3.10). The 1-2 μm size range was used to represent the entire population of microbubbles. The exposed-ligand architecture led to a significant increase in complement activity compared to the P2K control (3.8-fold increase for ELA 5% vs. 1.5-fold increase for P2K control). It is suggested that this increase in C3/C3b

binding was due to the presence of RGD peptide on the surface, which interacts with complement proteins in serum. C3 molecules contain unstable thioester bonds upon cleavage of C3a from C3b (Murphy, Travers et al. 2008). RGD peptides contain such nucleophilic groups (e.g., the carbonyl group on Asp and the amino group on Arg), which could trigger the immobilization of C3/C3b molecules on the ELA microbubble surface and activate the alternative pathway. The addition of RGD peptide to the surface of BLA microbubbles similarly led to a significant increase in C3/C3b binding. However, when compared to ELA microbubbles, the increase was much lower (1.3-fold increase for BLA 5% vs. no increase for P5K control). Such a small difference in MFI suggested that the buried-ligand architecture indeed partially inhibited the binding of C3/C3b to the microbubble surface and decreased the immunogenicity of targeted microbubbles.

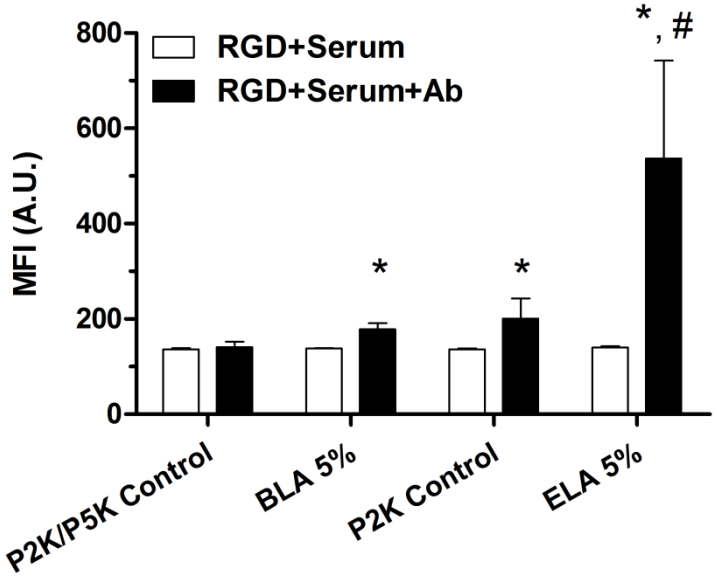

Figure 3.10. Flow cytometric analysis of complement component C3/C3b binding to 5% RGD peptide labeled 1-2 μm microbubbles. Significant binding occurred to RGD labeled ELA microbubbles in comparison with P2K control, suggesting the targeting ligand was immunogenic. BLA microbubbles also showed C3/C3b binding, indicating partial complement protein fixation. However, the increase of MFI value for targeted ELA microbubbles was much higher than that for BLA microbubbles, supporting our hypothesis that the buried-ligand architecture could indeed successfully shield the RGD peptide from complement recognition. "*" denotes a significant increase vs. the corresponding "RGD+Serum" measurement, and "#" denotes a significant increase vs. P2K control ($p<0.05$).

3.3.8. Effect of PEG Overbrush Height

To further illustrate the protective role of PEG chains, the MFI for 5% conjugated RGD peptides for microbubbles with different overbrush lengths was compared (Figure 3.11). In addition to the ELA and BLA-P5K design, a different bimodal brush layer using DSPE-

PEG3000 to form a shorter PEG overbrush was tested for complement C3/C3b binding. It was hypothesized that the shorter PEG overbrush would result in an intermediate inhibition of C3/C3b binding. Indeed, for all three size ranges, BLA-P3K microbubbles showed a measured MFI value that fell between the values detected for ELA and BLA-P5K designs when the same amount of RGD peptide was conjugated to the surface. For 6-8 μm microbubbles, there was no significant difference in C3/C3b binding between targeted BLA-P3K and BLA-P5K microbubbles.

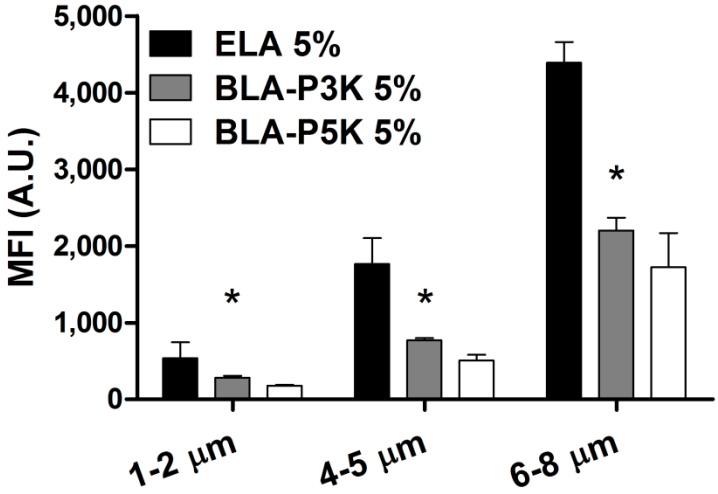

Figure 3.11. Illustration of the effect of PEG overbrush height on complement C3/C3b fixation. For targeted microbubbles, BLA-P3K showed an intermediate MFI value, supporting the hypothesis that DSPE-PEG3000 chains formed an intermediate brush layer to protect the targeting ligand from the complement system. "*" denotes a significant difference vs. the corresponding ELA 5% ($p<0.05$).

The buried-ligand architecture did not completely inhibit the binding of complement C3/C3b to the targeted microbubble surface, presumably due to the phase separation of the phospholipid species in the lipid monolayer coating the microbubble shell. It is also possible that the transient excursion of the PEG polymer chains could bring the RGD ligands past the overbrush and result in complement recognition. However, when compared to targeted ELA microbubbles with the same amount of RGD conjugated to the surface, the amount of C3/C3b binding for BLA microbubbles was significantly reduced (~ -52% and ~ -68% for BLA-P3K and BLA-P5K, respectively, for 5% RGD peptide). It is presumably the combined effect of the PEG overbrush shielding the RGD peptide and inhibiting C3/C3b fixation on the microbubble surface that resulted the reduced complement activation. Therefore, it is concluded that the buried-ligand architecture successfully protects RGD peptides on the surface of microbubbles from complement recognition, and targeted BLA microbubbles are significantly less immunogenic than ELA microbubbles *in vitro*.

3.3.9. Effect of Microbubble Surface Charge

Finally, the effect of surface charge on human complement fixation was investigated. Figure 3.12 shows the human complement C3/C3b binding plotted against the measured average zeta potential (Table 3.2) for all microbubble formulations within the 1-2 μm diameter range. A weak correlation between microbubble zeta potential and complement C3/C3b fixation was observed: as the negative zeta potential increased, there was more C3/C3b binding on the microbubble surface. It has been previously reported that high surface charge (either positive or negative) promotes complement activation (Chonn, Cullis et al. 1991). Here, similar findings

were observed to support this hypothesis. However, it is necessary to point out that complement fixation is a complex interplay of long and short range interactions between the C3/C3b molecule and the microbubble surface groups, and it therefore is likely that the combined effect of surface charge and details of the PEG brush dictate the binding of complement protein molecules. More experimental studies will be required to distinguish these two effects.

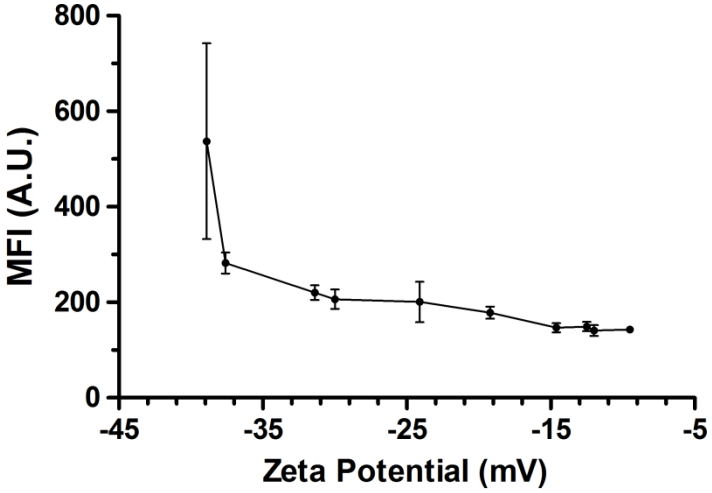

Figure 3.12. Illustration of the effect of microbubble surface charge on complement C3/C3b fixation. Higher negative zeta potential led to a higher complement C3/C3b binding, suggesting a weak correlation between microbubble surface charge and complement activation.

3.4. Conclusion

Complement activation-related pseudoallergy (CARPA) is an important adverse effect that has been observed clinically with non-targeted ultrasound contrast agents. Increased incidence of CARPA arising from immunogenic groups on targeted microbubbles is therefore a

significant safety concern for the viability of ultrasound molecular imaging. In this study, the immunogenicity of the targeted microbubbles with various surface architectures and ligand surface densities was investigated. Targeted microbubbles with either the exposed- or buried-ligand architecture (ELA or BLA, respectively) were generated using a post-labeling technique, and it was shown that they were stable during incubation in human complement-preserved serum at physiological conditions for at least 2 hrs with minimal change in size distribution or concentration. Three serum factors (albumin, IgG and complement C3/C3b) were tested for microbubble binding, and only C3/C3b binding was detected using our system. Even though RGD peptide is a physiological ligand, it was shown that it could still trigger an immune response when conjugated to the surface of microbubbles. However, the PEG overbrush on the surface of BLA microbubbles partially inhibited the recognition of RGD peptide by the complement system and, therefore, reduced the ligand-mediated immunogenicity. When the surface coverage of RGD peptide was increased by two orders of magnitude, C3/C3b binding was increased significantly for ELA microbubbles, while it stayed relatively constant for BLA microbubbles. In addition, evidence of the protective role of the PEG overbrush on complement C3/C3b fixation was observed by showing that P5K control microbubbles had the lowest C3/C3b binding and that BLA-P3K microbubbles could still partially inhibit complement binding even with a shorter PEG overbrush layer. The results presented in this Chapter show that the BLA strategy offers a means of targeting microbubbles without increasing complement activation and suggest that further studies are warranted to investigate the *in vivo* molecular imaging capabilities of such microbubbles.

Chapter 4: Effect of Poly(ethylene glycol) Brush Architecture on *In Vivo* Microbubble Circulation Persistence

4.1. Introduction

In order to improve the contrast sensitivity of imaging targeted microbubbles for molecular imaging applications, many attempts have been made to improve the targeting ligand and adhesion schemes and microbubble detection methods (Dayton and Ferrara 2002; Zhao, Borden et al. 2004; Borden, Sarantos et al. 2006; Dayton and Rychak 2007; Zhao, Kruse et al. 2007). Since the acoustic behavior of microbubbles is highly dependent on their size, more recently, research focus has been shifted to improve the echogenicity of the contrast agents themselves. Talu et al. (Talu, Hettiarachchi et al. 2007) used a flow focusing technique to produce monodisperse microbubbles and demonstrated their potential for enhanced contrast sensitivity *in vitro* by showing high correlation between microbubble echogenicity and size distribution. In an *in vivo* experiment, Sirsi et al. (Sirsi, Feshitan et al. 2010) measured the contrast enhancement of non-targeted microbubbles in mouse kidneys using high frequency ultrasound and showed that their contrast-to-tissue signal could be improved based on microbubble size and concentration.

In addition to contrast enhancement, microbubble circulation persistence is also directly correlated to their size. In the same experiment, Sirsi et al. (Sirsi, Feshitan et al. 2010) also found that large microbubbles persisted in circulation much longer than smaller ones. However, when the injected gas volume was matched, all microbubble sizes showed a similar persistence half-life. In an similar experiment using rat models, Streeter et al. (Streeter, Gessner et al. 2010)

showed supporting results that size-sorted 3 μm microbubble produced at least 3 times longer circulation time than size-sorted 1 μm and unsorted samples when imaged at lower frequency. All these findings indicated that the dissolution of the microbubble gas core played a larger role in contrast elimination than the filtering by the lungs and spleen during circulation (Kabalnov, Klein et al. 1998; Sirsi, Feshitan et al. 2010).

Many studies have been performed to investigate the effect of surface chemistry on the circulation persistence of biocolloids. Hydrophilic polymers, such as PEG chains or PEG chain derivatives, have long been incorporated into the surface of liposomes in order to prolong their circulation time owing to the polymeric steric hindrance effect (Immordino, Dosio et al. 2006). Phillips et al. (Phillips, Klipper et al. 1999) demonstrated that by adding 10 mol% DSPE-PEG5000 chains into the formulation, the persistence half-life of liposome-encapsulated hemoglobin was increased by greater than 3-fold when compared to non-PEG-containing formulations. More recently, du Toit et al. (du Toit, Govender et al. 2011) showed that the persistence of lipid nanobubbles could be enhanced by changing the surface charge with a polymeric anionic hydrogel shell. Interestingly, Fisher et al. (Fisher, Christiansen et al. 2002) showed different findings with lipid microbubbles. Using intravital microscopy, he demonstrated that the addition of negative charge on the surface of microbubbles could decrease their circulation time in the capillaries by increasing complement-mediated attachment to the endothelium.

The present study is to extend previous work on the stealth microbubble design, in which targeted microbubbles with various surface architectures were studied for their *in vivo* contrast enhancement and circulation persistence. Size isolated microbubbles with different surface architectures (Figure 4.1) were generated in order to eliminate the size effect on their circulation

behavior. RGD peptide was used as the targeting ligand to simulate a relevant biomarker for tumor progression. The microbubble contrast enhancement properties were examined in mouse models using a commercially available high frequency ultrasound scanner. It has been previously reported that there is a close correlation between complement activation *in vitro* and *in vivo* using animal models (Ishida, Kojima et al. 2000). Based on the results presented in Chapter 3, it was assumed that the buried-ligand architecture could effectively reduce complement activation *in vivo* and therefore decrease the microbubble elimination rate. The results presented in this chapter are relevant to contrast-enhanced small animal imaging and offer insights for generating stealth ultrasound contrast agents using the buried-ligand architecture design.

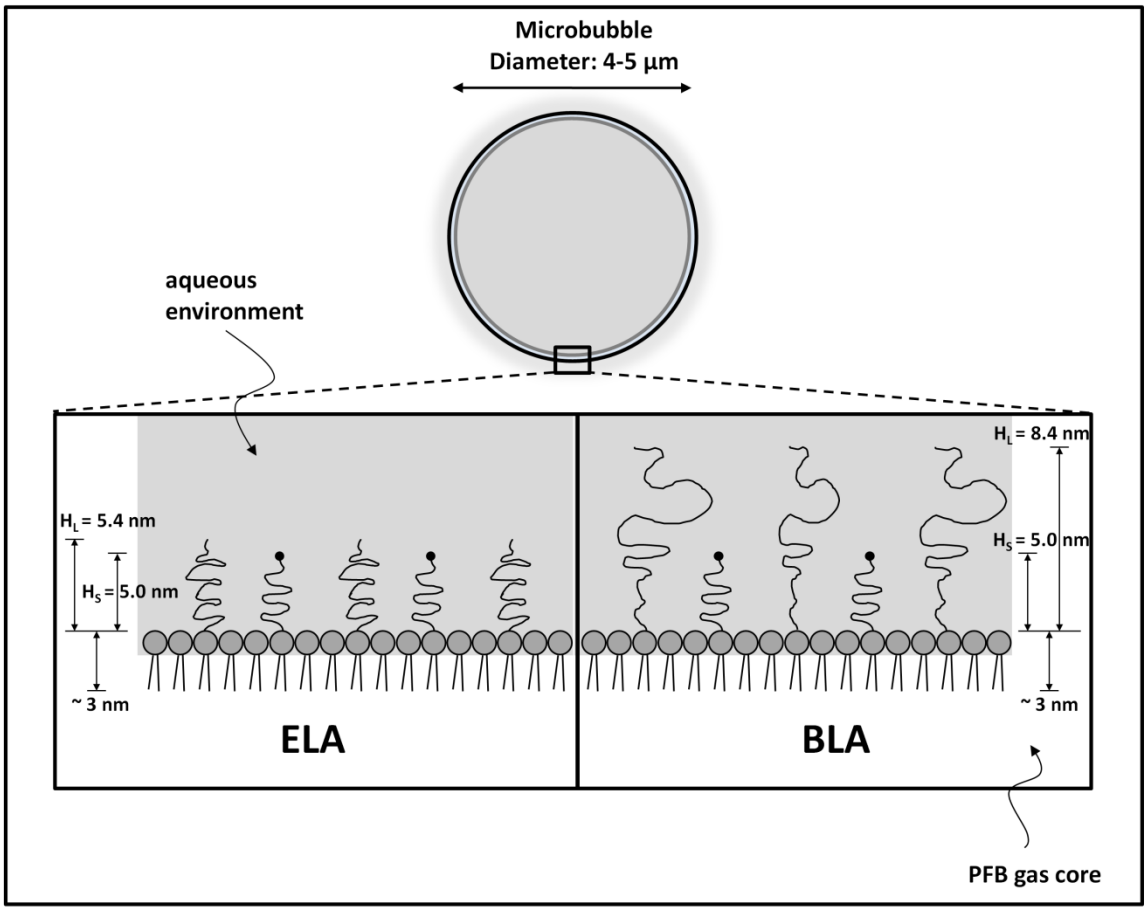

Figure 4.1. Cartoon illustrating microbubble surface architecture design for *in vivo* perfusion imaging studies. The PEG chain length was estimated using self-consistent field (SCF) theory (Lai and Zhulina 1992) as mentioned in Chapter 2.

4.2. Materials and Methods

4.2.1. Materials

Phospholipids were purchased from either Avanti Polar Lipids, Inc. (Alabaster, AL) or NOF America Corporation (White Plains, NY), including 1,2-distearyol-sn-glycero-3-phosphocholine (DSPC), 1,2-distearyol-sn-glycero-3-phosphoethanolamine-N-

[methoxy(polyethylene glycol)2000] (DSPE-PEG2000), 1,2-distearyol-sn-glycero-3-phosphoethanolamine-N-[maleimide(polyethylene glycol)2000] (DSPE-PEG2000-M) and 1,2-distearyol-sn-glycero-3-phosphoethanolamine-N-[methoxy(polyethylene glycol)5000] (DSPE-PEG5000). All phospholipids were stored in the freezer at -20 °C. The perfluorobutane gas (PFB, 99 wt% purity) used for microbubble generation was obtained from FluoroMed, L.P. (Round Rock, TX). The RGD peptide (99.9% purity) was purchased from Peptides International (Louisville, KY) and was dissolved in 3 vol% degassed acetic acid (Sigma-Aldrich). The dissolved RGD peptide was aliquoted into 50-μL volume and stored in nitrogen at -20 °C.

4.2.2. Microbubble Generation and Size Isolation

The compositions of microbubble samples for all the experiments performed are listed in Table 4.1. Microbubbles were generated using the probe sonication method as described elsewhere (Feshitan, Chen et al. 2009). Briefly, the indicated amounts of each phospholipid species were mixed and hydrated with a phosphate buffered saline (PBS) mixture (90 vol% PBS:10 vol% 1,2-propanediol:10 vol% glycerol; Sigma-Aldrich) to a final lipid/surfactant concentration of 2 mg/mL. The lipid solution was heated in a water bath at ~65 °C for 15 min, and then sonicated with a 20 kHz probe (model 250A, Branson Ultrasonics; Danbury, CT) at low power (power setting dialed to 3/10; 3W) in order to heat the lipid suspension above the DSPC main phase transition temperature (~ 55 °C) and further disperse the lipid aggregates into small, unilamellar liposomes. PFB was introduced by flowing it over the surface of the lipid suspension. Subsequently, high power sonication (power setting dialed to 10/10; 33 W) was applied to the suspension for about 10 s at the gas-liquid interface to generate microbubbles. The

generated microbubbles were concentrated by centrifugation flotation in a bucket-rotor centrifuge (Model 5804, Eppendorf; Westbury, NY) at 300G for 3 min. The infranatant, which contained residual lipids and vesicles that did not form part of the microbubble shells, was recycled to produce the next batch of microbubbles. All resulting microbubble cakes were combined and re-suspended in PBS to improve total yield.

Table 4.1. Microbubble compositions for *in vivo* perfusion imaging studies

	Phospholipid Composition (mol %)			
Samples	DSPC	DSPE-PEG2000	DSPE-PEG2000-M	DSPE-PEG5000
ELA Control	90	10	-	-
ELA	90	-	10	-
BLA Control	90	5	-	5
BLA	90	-	5	5

The microbubble size isolation method was used as first introduced by Feshitan et al. (Feshitan, Chen et al. 2009). A brief description of the size isolation protocol is presented here. After combining all the initial cakes, microbubbles with diameter less than 4 μm were removed by centrifuging at 110G for 1 min. The cake was collected and re-suspended in PBS, while the infranatant was discarded. This washing step was repeated 5-7 times to fully ensure all the smaller microbubbles were removed from the sample. Microbubbles with diameter greater than 5 μm were removed by centrifuging at 70G for 1 min. The infranatant containing 4-5 μm microbubbles was collected, and the cake was discarded. The collected infranatant was centrifuged again at 120G to concentrate the sample. This step was repeated 3-5 times to ensure a sufficient number of 4-5 μm microbubbles were collected. The final concentrated 4-5 μm

microbubble sample (concentration $>1\times10^9$ #/mL) was then re-suspended in 1 mL PBS and stored in room temperature overnight. Although we have previously shown that size isolated microbubble samples were stable at 4 °C for at least 2 weeks (Feshitan, Chen et al. 2009), all the microbubble samples used for this study were freshly prepared within 24 hrs to ensure experimental consistency.

4.2.3. RGD Peptide Conjugation to Targeted Microbubbles

To generate targeted microbubbles, the final concentrated 4-5 μm microbubble cake was re-suspended in 1 mL PBS mixed with 5 mM EDTA (pH 6.5). A Coulter Multisizer III particle counter (Beckman Coulter; Opa Locka, FL) with a 50 μm aperture was used to measure the size distribution and particle concentration. The amount of RGD peptide needed was then calculated as previously described (Chen and Borden 2010). RGD peptide was added to react with maleimide functional groups on the distal end of PEG chains at a molar ratio of 30:1 (RGD:maleimide). The reaction was carried out on a benchtop rotator for 12 hours in room temperature. Unreacted RGD peptide was removed by centrifuging the microbubble suspension at 110G for 1 min. The concentrated microbubble cake was then re-suspended in PBS and analyzed by the Multisizer.

4.2.4. Animal Preparation and Handling

All animals were handled according to the National Institute of Health guidelines, and our experimental protocol was approved by the Columbia University Institutional Animal Care

and Use Committee. Female CD-1 mice between 4 to 8 weeks of age (Charles River Laboratories; Wilmington, MA) were used for the contrast persistence studies. Before imaging an animal, it was first anesthetized in an induction chamber using aerosolized 2% isoflurane-oxygen mixture. Once sedated, it was placed on a heated mouse handling table while continuously breathing 1% to 2% isoflurane-oxygen mixture via nosecone delivery for the duration of the experiment. The animal heart rate, respiratory rate and temperature were monitored using a TMH-150 physiological monitoring unit (VisualSonics; Toronto, Ontario, Canada). The mouse was placed in the prone position, and its back was shaved with an electric clipper. A depilatory cream was applied to the animal skin to dissolve any remaining hair that would interfere with the ultrasound imaging. A modified 27-gauge 1½ butterfly catheter (Terumo Medical Corporation; Somerset, NJ) was inserted into the mouse's tail vein for microbubble injections. A Vevo 770 small animal ultrasound imaging scanner with a 40-MHz imaging transducer (VisualSonics) was placed over the kidney region and coupled with Aquasonic-100 ultrasound transmission gel (Parker Laboratories; Fairfield, NJ) to ensure the quality of signal transmission. Figure 4.2 shows an actual image taken of a prepared mouse on the imaging platform ready for microbubble injection. After the mouse regained consciousness at the end of each imaging session, it was returned to its cage.

Figure 4.2. A prepared mouse on the imaging platform ready for microbubble injection.

4.2.5. Microbubble Injection and Image Acquisition

A 500 μL diluted microbubble suspension at 1×10^{8} #/mL concentration in sterilized 0.9% NaCl saline solution (Hospira, Inc.; Lake Forest, IL) was freshly made before each animal injection. A 50 μL bolus injection of the diluted microbubble sample, followed immediately by 50 μL sterilized saline flushing solution, was injected while imaging data was continuously acquired. The mouse kidneys were selected as the imaging location for this study because of the proximity to the skin surface and the high concentration of vasculature. Contrast mode images were collected while respiratory gating was applied in synchronization with the mouse respiratory cycle to reduce motion artifact during data analysis. The effective frame rate during image acquisition was between 1-2 frames/sec. At the focal length (6 mm), the peak negative pressure is 3.49 MPa with an acoustic power of 0.017 mW and a mechanical index of 0.57 (VisualSonics Vevo 770 High-Resolution Imaging System Operator Manual). The time-gain compensation (TGC) settings were kept at a value of 10 throughout all imaging sessions to ensure signal linearization during data analysis. The video data was collected prior to a bolus

injection of microbubbles, and was continued for up to 30 min to allow the majority of the microbubbles to be cleared by the animal. If there were still microbubbles visibly circulating in the bloodstream, the image acquisition was prolonged to accommodate for the longer persistence. Figure 4.3 shows typical images of the mouse kidney before and after a bolus injection of microbubble contrast agents. Only one microbubble injection was given to the same mouse during each imaging session to minimize effects of a potential immune response caused by repeated injections (n = 6-8 per group).

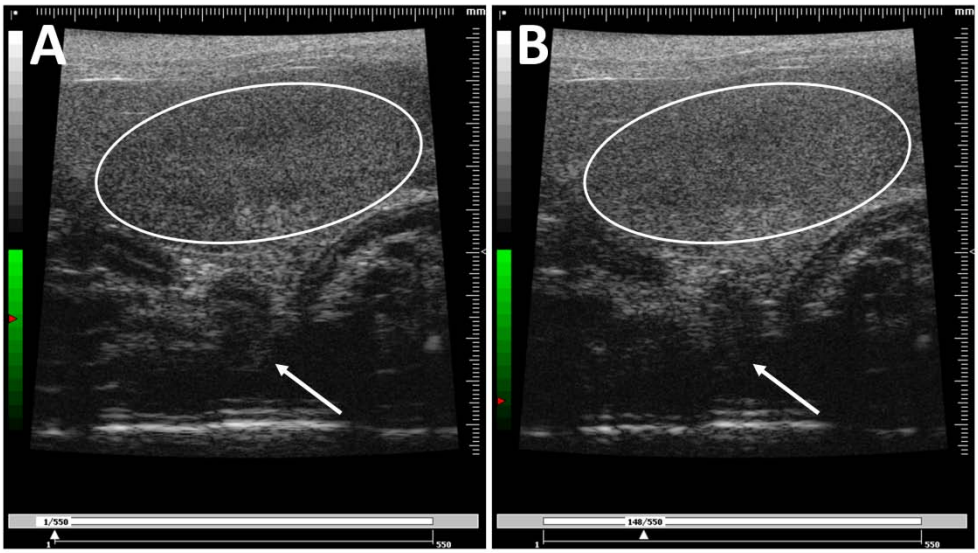

Figure 4.3. Typical images of the mouse kidney before (A) and after (B) a bolus injection of microbubbles. The kidney region is outlined in white. Significant increase of contrast signal was observed as speckles within the kidney region. Arrows point out the microbubble shadowing effect due to signal attenuation.

4.2.6. Data Analysis

All image analyses were done using either the Vevo 770 application software (VisualSonics) or a custom developed image processing program in LabVIEW (National Instruments Corporation; Austin, TX). Two sets of regions of interest (ROIs) were selected and analyzed to ensure data consistency (Figure 4.4). In the first set, one large ROI in the upper portion of the kidney was selected so that it gave the maximum increase of signal intensity while minimizing effects of signal attenuation and microbubble shadowing (Figure 4.4B). In the second set, multiple ROIs were drawn across different regions of the kidney (Figure 4.4C). The multiple ROIs were divided into two groups: three in the upper region and three in the lower region of the kidney. The measured signal intensity was averaged within these two groups, and the final values were used for analysis. All images were examined to ensure there was no gross movement of the kidney to cause ROI shifting. The contrast enhancement was calculated using the mean grayscale video intensity determined by integrating the pixel intensity values over the ROI in every acquired frame. All computed contrast enhancement data sets were baseline adjusted and plotted using Prism 5 graphing software (Graphpad Software, Inc.; La Jolla, CA) for data fitting.

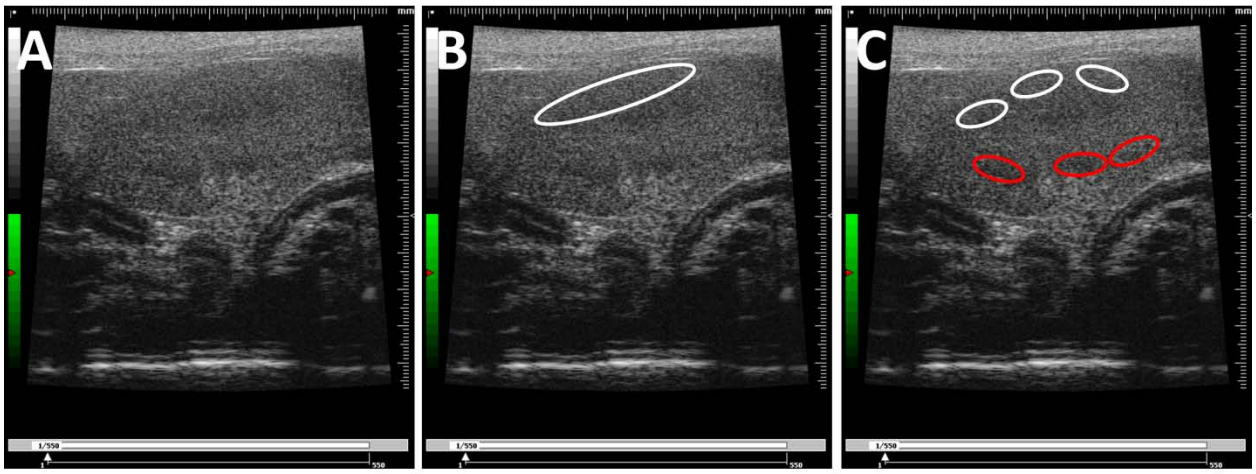

Figure 4.4. Typical ultrasound images of the mouse kidney showing the drawings of two sets of regions of interest (ROIs) following two different selection criteria. (A) The original image of the kidney. (B) The image of the kidney with one large ROI selected in the upper portion. (C) The image of the kidney with multiple smaller ROIs selected across different regions of the kidney.

Two pharmacokinetic drug persistence models were used to describe microbubble perfusion in the kidney: a single-compartment model as described by Saltzman (Saltzman 2001; Sirsi, Feshitan et al. 2010) (Equation 4.1) and a two-compartment model as described by Sirsi et al. (Sirsi, Hernandez et al. 2011) (Equation 4.2 – 4.4). The single-compartment model assumes common first-order kinetics for the spreading and elimination, and uniform distribution of an intravenously injected drug in a single compartment. Slow absorption is taken into consideration to represent the entry of the drug into the compartment.

$$C(t) = \frac{C_0 k_1}{k_2 - k_1}(e^{-k_1 t} - e^{-k_2 t}) \qquad \text{Equation 4.1}$$

where C is the relative amount of measured contrast enhancement; C_0 is the initial amount of contrast; k_1 is a first order rate constant describing the influx of the contrast agent into the system;

k_2 is a first order rate constant describing the elimination of the contrast agent from the system and t is the contrast persistence time.

The two-compartment model assumes that, after the drug is injected rapidly into the body, it is slowly distributed throughout one compartment while irreversibly accumulated in a second compartment. A first-order kinetic is used to describe the accumulation of the drug that contributes to its elimination from free circulation, and the total concentration of the drug is a combination of that in both compartments.

$$C(t) = C_1(t) + C_2(t) \qquad \text{Equation 4.2}$$

$$C_1(t) = \frac{C_0 k_1}{(k_2+k_3)-k_1}\left[e^{-k_1 t} - e^{-(k_2+k_3)t}\right] \qquad \text{Equation 4.3}$$

$$C_2(t) = C_0 k_1 k_3 \left[\frac{e^{(k_4-k_1)t}-1}{k_1^2-k_1k_2-k_1k_3-k_1k_4+k_2k_4+k_3k_4} + \frac{e^{(k_4-k_3-k_2)t}-1}{k_2^2+k_3^2-k_1k_2-k_1k_3+k_1k_4+2k_2k_3-k_3k_4}\right]$$

Equation 4.4

where C_1 is the relative amount of measured contrast enhancement from the intravascular compartment (compartment 1); C_2 is the relative amount of measured contrast enhancement from the non-circulating microbubbles (compartment 2); k_3 is a first order rate constant describing the efflux from compartment 1, which is the same as the influx into compartment 2 and k_4 is a first order rate constant describing the elimination of microbubbles from compartment 2. All curve fitting parameters, such as amplitude, persistence half-life, decay rate and total integrated signal enhancement (Area Under the Curve or AUC) , were obtained using the nonlinear regression tool in Prism 5 software. All statistical analyses were also performed using Prism 5 software.

4.3. Results

4.3.1. Microbubble Size Distribution

For each set of microbubble components, the probe sonication method produced a milky, white microbubble suspension that was stable over the experimental timeframe. Freshly made microbubble suspensions were highly polydisperse in size as measured by the Multisizer. Figure 4.5 compares the number- and volume-weighted size distributions between freshly made and size-isolated ELA microbubbles as an example. Other microbubble formulations showed similar size distributions. For a freshly sonicated microbubble suspension, the number-weighted size distribution showed that most of the microbubbles (>90%) were smaller than 4 μm in diameter. Interestingly, the Multisizer measurement did not show distinct peaks (at 1-2 μm, 4-5 μm and 6-8 μm) to indicate a multimodal size distribution in either number- or volume-weighted data as we previously reported using the Accusizer (Feshitan, Chen et al. 2009).

The size isolation method developed by Feshitan et al. (Feshitan, Chen et al. 2009) uses centrifugation flotation to allow a rapid and efficient size selection of microbubbles and reduce sample polydispersity. Figure 4.6 shows the number- and volume-weighted size distributions after size isolation for all microbubble samples as measured by the Multisizer, and Table 4.2 lists the initial concentration, mean diameter and injected gas volume for all four microbubble groups. In order to ensure stability, the concentrations of all microbubble samples were maintained above 1×10^9 #/mL before injection. In Chapter 2, it was shown that small ligands with molecular weight <1 kDa, such as RGD peptides, could diffuse freely through the PEG brush layer and react completely with the functional groups at the distal end of the PEG chains. The conjugation of RGD peptide to the surface did not affect either microbubble size distribution or concentration.

There was no significant difference in the injected gas volume, which was calculated based on the volume-weighted mean diameter, between the four microbubble groups.

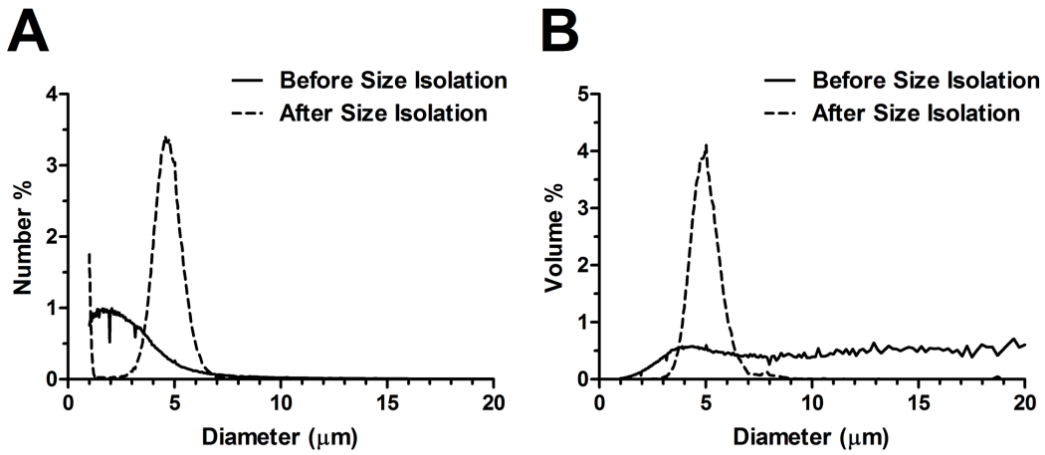

Figure 4.5. Typical microbubble number- (A) and volume-weighted (B) size distributions before and after size isolation. Freshly made microbubble suspensions were highly polydisperse, with most of the microbubbles (>90%) smaller than 4 μm (based on number-weighted size distribution). Interestingly, no obvious multimodal size distribution with distinct size peaks was observed for microbubble samples measured by the Multisizer, as apposed to the previous measurements made using the Accusizer (see Chapter 2 and Feshitan et al. (Feshitan, Chen et al. 2009)).

Table 4.2. Microbubble size distributions and concentrations

Samples	Initial Concentration (#/mL) (Mean)	Number-Weighted Mean Diameter (μm) (Mean ± SD)	Volume-Weighted Mean Diameter (μm) (Mean ± SD)	Injected Gas Volume (μL) (Mean)
ELA Control	3.93E+09	4.3 ± 0.1	5.0 ± 0.0	0.32
ELA	2.39E+09	4.2 ± 0.2	4.9 ± 0.1	0.31
BLA Control	2.09E+09	4.4 ± 0.2	5.2 ± 0.1	0.37
BLA	2.04E+09	4.0 ± 0.2	4.8 ± 0.2	0.29

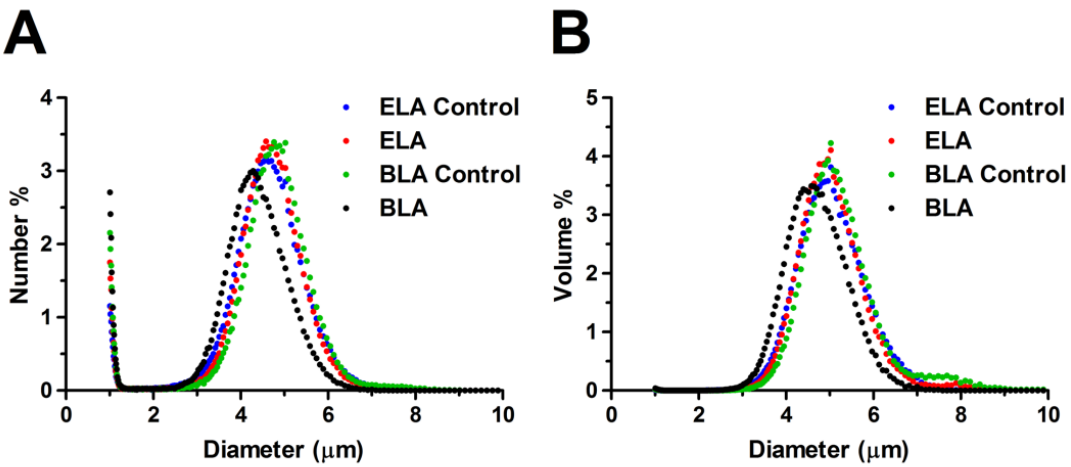

Figure 4.6. Microbubble number- (A) and volume-weighted (B) size distributions after size isolation by differential centrifugation. Neither the various surface architectures nor the presence of the targeting RGD peptide on the surface affected the size distribution. All detailed mean diameter and concentration values are listed in Table 4.2.

4.3.2. ROI Selection

In order to ensure that the selection of ROIs correctly represented the signal change of the entire kidney, two sets of ROIs were drawn for analysis following two different selection criteria (Figure 4.4). Time-intensity curves (TICs) of both sets of ROIs were generated for comparison to ensure data consistency. The TICs were calculated using the contrast detection software (VisualSonics or LabVIEW) by integrating the image pixel intensities over the ROI. Figure 4.7 shows typical TICs generated from the single large ROIs in the upper portion of the kidney for each microbubble formulation together with the fitted one-compartment pharmacokinetic contrast persistence model lines. Both ELA Control and BLA Control microbubbles gave similar persistence in circulation. The TICs for BLA microbubbles were typically very similar to

the ones for BLA Controls, with similar contrast enhancement level and persistence time, while for ELA microbubbles, the observed circulation time was noticeably shorter.

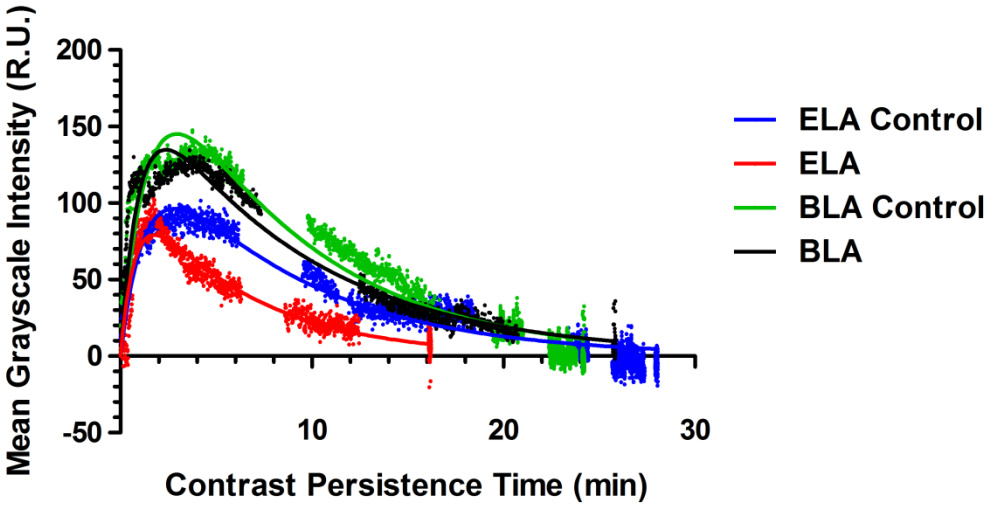

Figure 4.7. Typical time-intensity curves (TICs) generated using the single large ROIs in the upper portion following bolus injections of microbubbles with various surface architectures. Representative TICs are shown for each microbubble formulation tested. All data was baseline corrected using background images before injections as the corresponding references. The fitted one-compartment pharmacokinetic model was shown as solid lines.

A second set of TICs were generated using the averaged intensity values from the multiple smaller ROIs in both the upper and lower portions of the kidney. Figure 4.8 compares representative TICs for all microbubble formulations. It can be clearly seen that the lower ROIs (red ROIs in Figure 4.4C) typically showed much less maximum signal intensities when compared to the upper ROIs (white ROIs in Figure 4.4C), ranging between 20% and 65% of those for the upper ROIs for each microbubble group. This was attributed to the signal

attenuation (shadowing effect) from the microbubbles in the upper portion of the kidney. As a result, the signal increase detected in the lower portion was significantly reduced and could not be used to correctly represent the signal change of the entire tissue. Therefore, only the upper portion of the kidney was used to characterize microbubble contrast enhancement and persistence during data analysis.

4.3.2. High Frequency *In Vivo* Imaging

All mice were given 50 μL bolus injections of microbubbles at 1×10^8 #/mL concentration. Images of the animal's left kidney were continuously recorded during the bolus injection using a high-resolution small animal imaging scanner in the fundamental mode with a 40-MHz transducer. Figure 4.9 shows representative ultrasound images of the mouse kidney before and after a bolus injection of ELA microbubbles. The ROI used to calculate the contrast intensity change is outlined in white. Figure 4.9A is the background image of the kidney before microbubble injection. Figure 4.9B is the image taken at the peak amplitude of the signal intensity with grayscale contrast, which typically occurred 60-90 s after the bolus injection was given, and Figure 4.9C is the same image using the contrast detection software (VisualSonics) to highlight the increase of video intensity after microbubble injection.

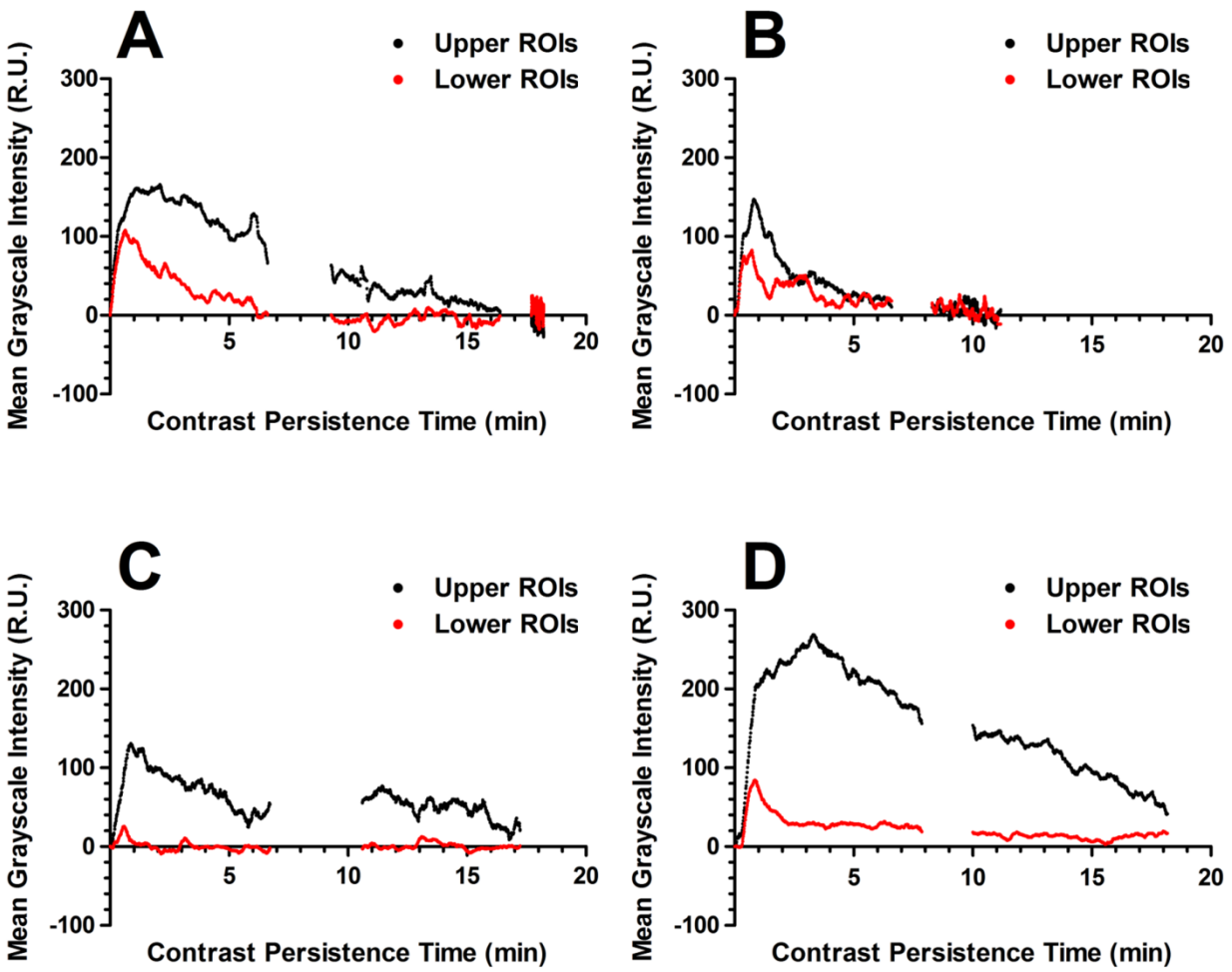

Figure 4.8. Representative averaged time-intensity curves (TICs) obtained using the smaller ROIs. Significantly reduced maximum signal intensities were observed in the lower ROIs for all microbubble groups, indicating microbubble-induced attenuation. All subsequent two-compartment model fitting was done using the averaged signal intensities calculated from the upper ROIs only. (A) ELA Control. (B) ELA. (C) BLA Control. (D) BLA.

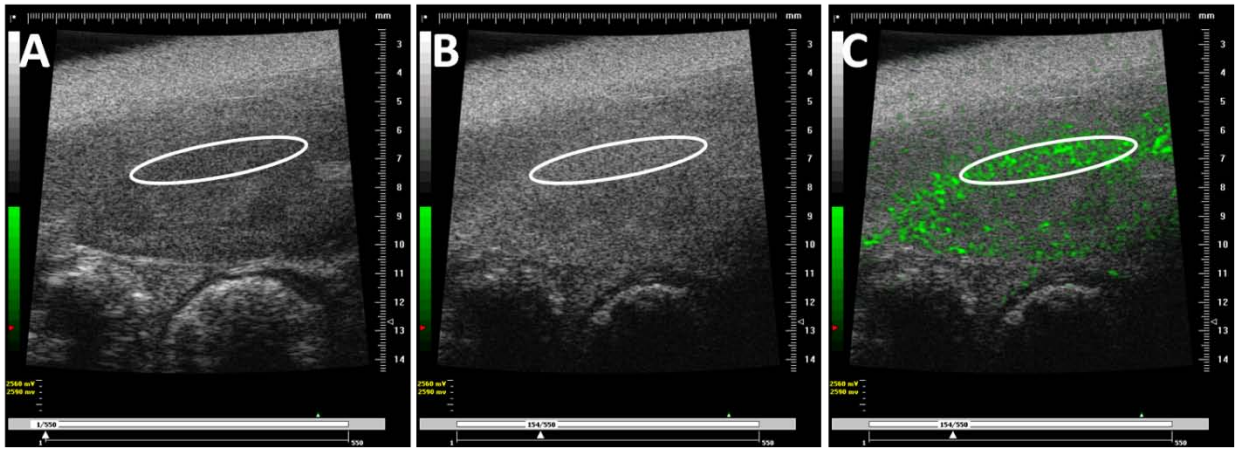

Figure 4.9. Representative ultrasound images of the mouse kidney showing contrast enhancement before (A) and after (B, C) a bolus injection of ELA microbubbles. The region-of-interest was outlined in white and used for the time-intensity curve analysis. (A) The background image of the mouse kidney before injection. (B) Grayscale contrast image of the same kidney at the peak signal intensity, typically occurred 60-90 s after the bolus was given. (C) The same image using contrast detection software to highlight the presence of microbubbles.

All four microbubble groups showed noticeable positive contrast enhancement after the bolus injections. The increase of brightness and speckling was observed evenly throughout the tissue in the ROI. The change of signal intensity calculated using the contrast detection software gave similar measurements between ELA and BLA samples, regardless of the presence of the targeting ligands, indicating that the surface architecture of the microbubbles did not affect the signal enhancement ability of these contrast agents.

4.3.3. One-Compartment Pharmacokinetic Model

The one-compartment pharmacokinetic model described by Saltzman (Saltzman 2001) was first used to analyze the TICs generated using the single large ROIs in order to determine the signal amplitude and contrast persistence half-time for microbubbles with different surface architectures. The model assumes that microbubbles are intravascular only during free circulation, and there is no passive accumulation of contrast agents onto or outside the vasculature. While these assumptions may not fully describe the kinetics of microbubble influx and clearance in circulation, the model fits the data generally well, with typical $R^2 > 0.90$, and allows the quantification and comparison of several important pharmacokinetic parameters such as the maximum intensity enhancement and the exponential microbubble elimination rate constant.

Positive contrast enhancement was detected for all microbubble samples. Figure 4.10 compares the grayscale signal amplitude among the four microbubble groups. The signal amplitude was determined by the maximum signal intensity increase using the TICs. There was no significant difference in signal amplitude between exposed and buried surface architectures as determined by a Students' t-test ($P = 0.50$ for ELA Control vs. BLA Control). In addition, the presence of the targeting ligand did not affect the signal amplitude ($P = 0.18$ for ELA Control vs. ELA and $P = 0.88$ for BLA Control vs. BLA), indicating that the contrast enhancement ability of microbubbles as ultrasound contrast agents was mainly dependent on microbubble diameter, or the gas core volume, not the surface structure of the monolayer phospholipid shell.

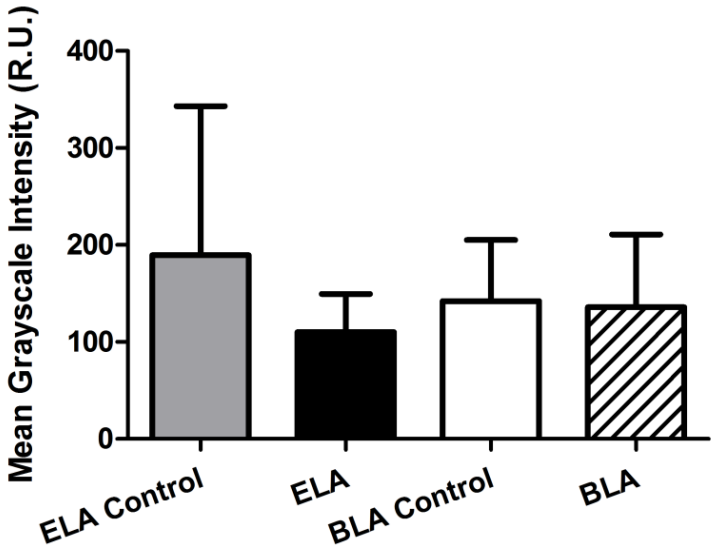

Figure 4.10. Maximum microbubble signal intensity obtained using the one-compartment pharmacokinetic model. The data was determined based on the TIC data within each ROI (single large ROI in the upper portion of kidney). No significant difference in signal amplitude was measured between exposed and buried surface architecture. In addition, the presence of RGD peptide on the surface did not affect the contrast enhancement ability of the microbubbles either.

The contrast circulation time was characterized by two parameters: persistence half-life and 25% time point, which was the time point when the intensity signal dropped down to 25% of its maximum amplitude value (Figure 4.11) (Mullin, Gessner et al. 2011). For the same number of microbubbles injected (5×10^6 #/bolus), ELA Control showed the longest persistence half-life with the largest uncertainties (14.6±8.27 min), while BLA Control had a non-statistically different persistence half-life (9.36±3.65 min, P = 0.20). The same trend was found in the signal 25% time point data (Figure 4.10B) for the control microbubbles. ELA Control showed the longest 25% time (26.0±16.2 min), while BLA Control gave a comparable measurement (16.0±6.41 min) with no statistical difference (P = 0.19).

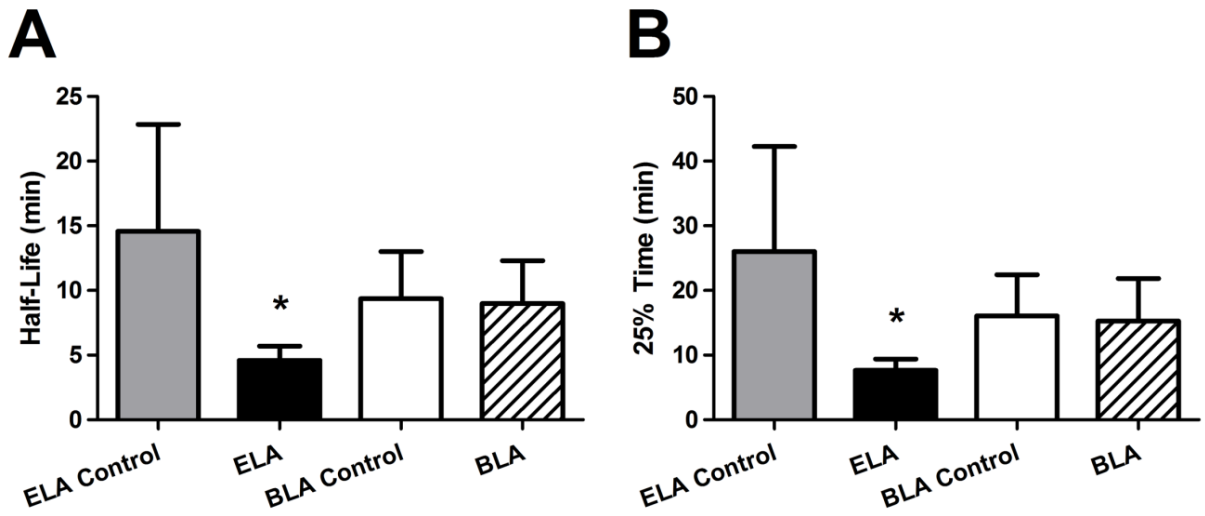

Figure 4.11. Persistence half-life and 25% time point of microbubbles obtained using the one-compartment pharmacokinetic model. The half-life (A) was determined from the TIC data at which the signal intensity decayed to half of its maximum amplitude, and the 25% time point (B) was determined at which the signal intensity decayed to 25% of its maximum amplitude. Significant persistence difference was measured between ELA and ELA Control, while BLA and BLA Control microbubbles showed similar circulation time. This data supported the hypothesis that the PEG overbrush was able to prolong the microbubble *in vivo* circulation time.

For the targeted microbubbles, ELA showed significantly reduced persistence half-life (4.59±1.11 min) when compared to ELA Control ($P < 0.01$). The presence of the RGD peptide on the surface shortened the microbubble circulation time by 68%. The 25% time point for ELA microbubbles was shortened significantly as well, down to 7.63±1.78 min, representing a 71% decrease when compared to ELA Control.

On the other hand, targeted BLA microbubbles showed a remarkably similar persistence half-life as to BLA Control (8.99±3.32 min) with no statistical difference ($P = 0.86$), confirming

the hypothesis that the buried-ligand architecture protected the RGD peptide from being detected by the immune system, and therefore reduced the ligand-induced immunogenicity and prolonged the contrast persistence time. Similarly, the 25% time point for targeted BLA microbubbles did not show a difference from BLA Control (15.3±6.56 min; P = 0.84), once again rendering support to the protective role of the PEG overbrush.

Next, we explored the effect of the total gas volume injected on the signal amplitude and persistence half-life (Figure 4.12). The total gas volume injected was calculated based on the volume-weight mean diameter measured by the Multisizer and the total number of microbubbles injected. As expected, all four microbubble groups gave similar total gas volume injected (~0.3 μL). There was no obvious relationship observed between either the signal amplitude or the persistence half-life and the total gas volume injected over this range.

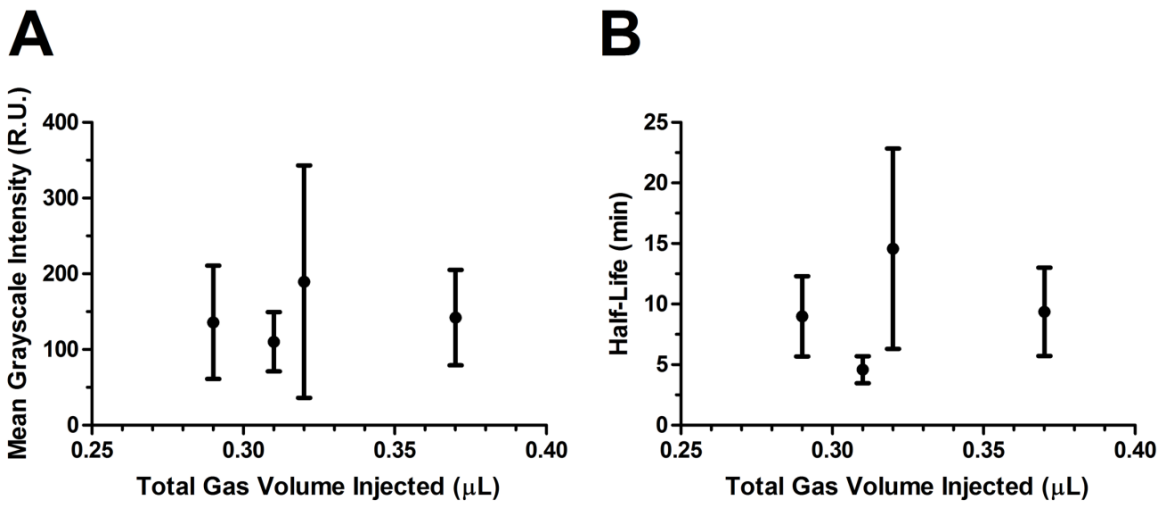

Figure 4.12. Illustration of the effect of total gas volume injected on signal amplitude and persistence half-life. No correlation was observed for either signal amplitude or persistence half-life on the total gas volume injected for the microbubble suspensions tested.

Figure 4.13 compares the model fitted parameters C_0, k_1, k_2 and AUC among tested microbubble groups. The C_0 parameter (Figure 4.13A) is the fitted initial amount of contrast intensity, and is directly related to the signal amplitude shown in Figure 4.10. It showed an identical trend as the signal intensity, with no significant difference detected between control and targeted groups, or microbubbles with different surface architectures.

The k_1 parameter (Figure 4.13B) is the fitted first-order influx rate constant, and is a measure of the inflow rate of the contrast agents in the mouse kidney. No trend was observed among the tested microbubble groups with mean k_1 values ranging between 1.9 and 2.8 min^{-1}, which was as expected since the influx rate depended on the bolus injection speed and the spreading of microbubbles in circulation and perfusion into the kidney.

The k_2 parameter (Figure 4.13C) is the fitted first-order elimination rate constant, and is a measure of the clearance rate of the contrast agents in the mouse kidney. No significant difference of the k_2 parameter was detected between ELA Control and BLA Control ($P = 0.36$). For targeted microbubbles, ELA showed a significantly higher k_2 value when compared to ELA Control ($P < 0.001$), while BLA microbubbles gave a similar k_2 value as their BLA Control counterparts ($P = 0.56$).

The AUC parameter (Figure 4.13D) is the integrated grayscale intensity, and is a measure of the total contrast signal enhancement in the ROIs from the microbubbles. Among the four groups tested, ELA Control showed the highest AUC, while ELA gave the lowest, with the mean AUC value being only 16% of that calculated for ELA Control. However, no statistical difference was determined between these two groups ($P = 0.07$) owing to the large variations among the calculated AUC values for ELA Control. On the other hand, BLA Control and BLA

microbubbles showed comparable AUC values, and were both statistically similar to that calculated for ELA Control (P = 0.30 and P = 0.31, respectively).

4.3.4. Two-Compartment Pharmacokinetic Model

For surface-modified microbubbles, it is possible that specific or non-specific interactions may result in accumulation of these contrast agents onto the vasculature during imaging. In order to test for this phenomenon, a more sophisticated two-compartment pharmacokinetic model was developed by Sirsi et al. (Sirsi, Hernandez et al. 2011) that separates the total intensity signal into two subcomponents that describe (1) the signal intensity generated by freely circulating microbubbles and (2) the signal intensity generated by passively accumulated or adherent, non-circulating microbubbles. The averaged TICs generated from the multiple smaller ROIs in the upper portion of the kidney were used to fit the two-compartment model in order to further characterize the circulation persistence of microbubbles with different surface architecture designs.

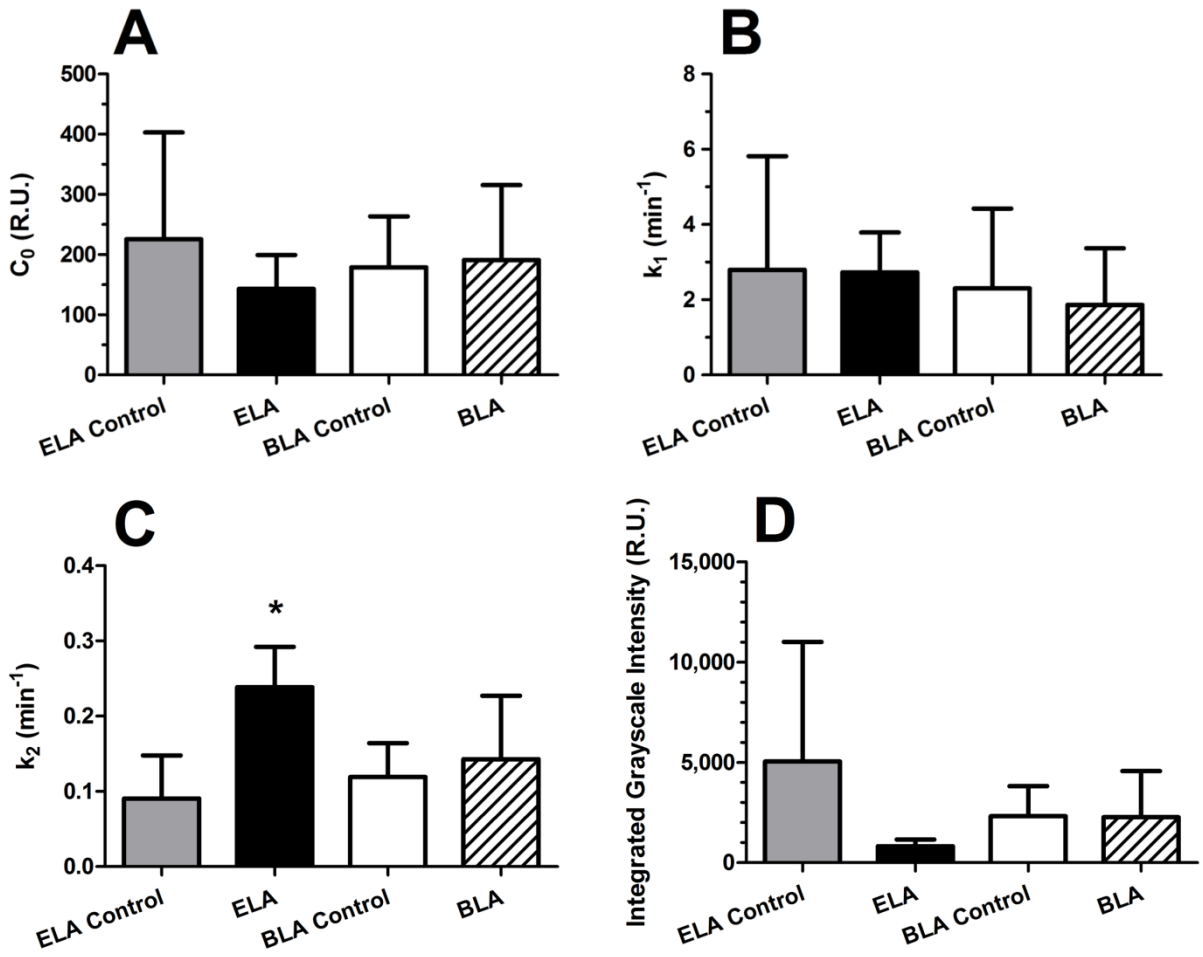

Figure 4.13. Fitted parameters of the TIC data using the one-compartment pharmacokinetic model. The parameters were determined using the least square regression analysis. (A) C_0 is proportional to the signal amplitude. Similar to the maximum signal intensity, no significant difference was measured across all microbubble samples. (B) k_1 is a measure of the influx rate of the microbubbles into the kidneys. No significant difference was measured across all samples. (C) k_2 is a measure of the decay rate of the microbubble signal. ELA showed significantly more rapid contrast elimination when compared to ELA Control, while BLA and BLA Control showed similar contrast decay rate. (D) AUC is a measure of the total integrated contrast enhancement determined by the area under the fitted curve. ELA showed only 16% contrast enhancement when compared to ELA Control, though no statistical difference was calculated. BLA and BLA Control both showed more similar contrast enhancement as to ELA Control (45% and 46%, respectively).

Figures 4.14 and 4.15 show a comparison of the two-compartment model fitted parameters among the four microbubble groups. Similar to the result obtained using the one-compartment model, the fitted C_0 parameter (Figure 4.14) once again did not show any significant difference between either the control and targeted microbubbles, or microbubbles with different surface architectures.

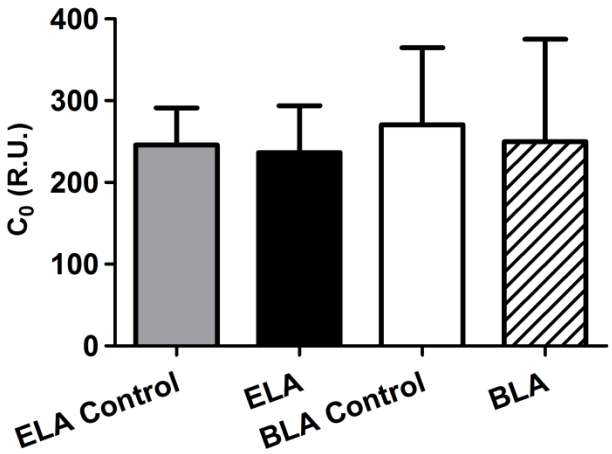

Figure 4.14. Fitted C_0 parameter using the two-compartment model. Similar to the one-compartment result, no significant difference was detected between either control and targeted microbubbles or microbubbles with different surface architectures.

Analogous to the one-compartment model, the k_1 parameter (Figure 4.15A) is the rate constant that describes the influx rate of microbubbles into the mouse kidneys upon injection. Once again, no statistical difference of the k_1 parameter was detected among the microbubble groups.

The k_2 parameter (Figure 4.15B) in the two-compartment model is the rate constant that describes the elimination of microbubbles from circulation owing to mechanisms other than adhesion to the kidney vasculature, such as dissolution, active clearance from the MPS and filtering by the liver, spleen and lungs, etc. No significant difference of the k_2 parameter was detected between ELA Control and BLA Control ($P = 0.52$). For targeted microbubbles, ELA showed a significantly faster clearance rate in comparison to ELA Control ($P < 0.05$), once again, indicating ligand-induced elimination. On the other hand, BLA microbubbles had a similar k_2 value as their BLA Control counterparts ($P = 0.30$).

The k_3 parameter (Figure 4.15C) is the rate constant that describes the elimination of microbubbles from circulation due to passive accumulation or non-specific adhesion. No trend was observed among the four groups with mean k_3 values ranging between 0.02 and 0.11 min^{-1}.

Finally, the k_4 parameter (Figure 4.15D) is the rate constant that describes the elimination of adherent microbubbles from the kidney vasculatures. Since the model assumes irreversible accumulation of contrast agents onto to the kidney endothelium, the k_4 parameter mainly accounts for the dissolution rate of the adherent microbubbles. No significant difference was detected for the k_4 parameter, which was expected since microbubble dissolution did not depend on their surface architecture or the presence of the targeting ligand.

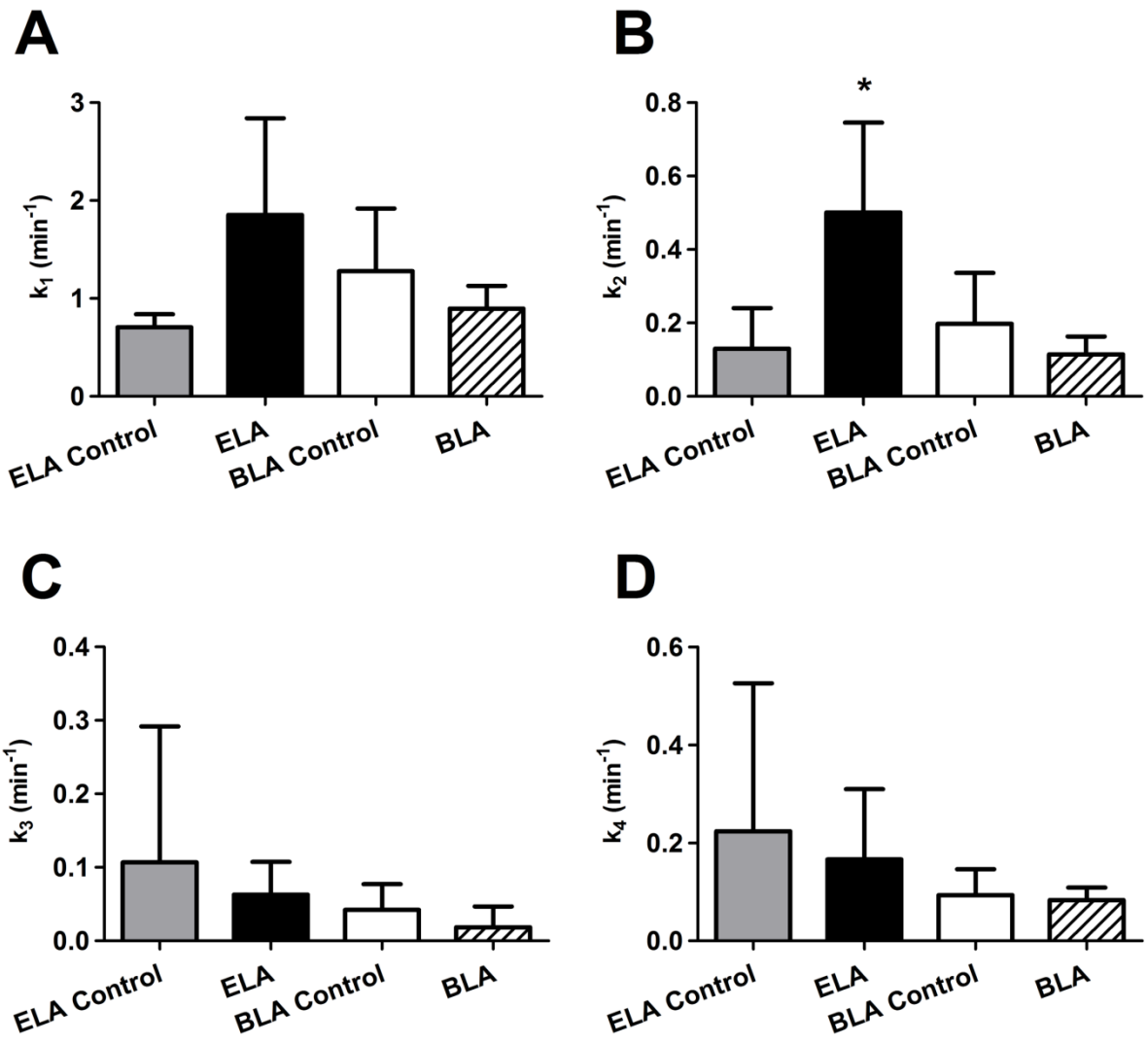

Figure 4.15. Fitted parameters of the averaged TIC data using the two-compartment pharmacokinetic model. (A) k_1 is a measure of the influx rate of microbubbles into the kidney. No significant difference was detected among the four groups. (B) k_2 is the microbubble elimination rate due to mechanisms other than accumulation onto the kidney vasculature. ELA showed significantly faster clearance rate than ELA Control, while BLA showed comparable k_2 values as BLA Control. (C) k_3 is the adhesion rate constant of microbubbles "stuck" at the kidney vasculature. No significant difference was observed among the groups. (D) k_4 is the microbubble dissolution rate constant. No significant difference was detected among the groups.

4.4. Discussion

Size-selected microbubbles with different surface architectures were used for *in vivo* ultrasound imaging to study their contrast enhancement ability in mouse kidneys at 40 MHz. Two surface architectures were designed and tested: exposed- and buried-ligand architectures (Figure 4.1), and RGD peptide was conjugated to the microbubble shell as the targeting ligand to simulate molecular imaging applications.

Two sets of ROIs were drawn for analysis following two different selection criteria. On one hand, a single large ROI was selected in the upper portion of the kidney (Figure 4.4B) in order to detect the maximum increase of signal enhancement while the potential for microbubble-induced attenuation was minimized. Microbubble-induced attenuation is undesired because it artificially reduces the contrast enhancement during imaging. Therefore, it is important to minimize signal attenuation during quantitative contrast flow measurements. On the other hand, multiple smaller ROIs were drawn across different regions of the kidney (Figure 4.4C), and their measured signal intensities were averaged to represent the total change of the entire tissue. Sirsi et al. (Sirsi, Feshitan et al. 2010) reported that microbubble shadowing was observed in the lower region of mouse kidneys after bolus injections of 1-2 μm microbubbles with similar lipid compositions, but at a higher concentration. The present data confirmed their findings by showing that the TICs generated using the lower ROIs (red ROIs in Figure 4.4C) had significantly reduced maximum signal intensities than those generated using the upper ROIs (white ROIs in Figure 4.4C), indicating microbubble shadowing. Therefore, only the upper portion of the mouse kidneys was selected for data analysis.

Previous studies have demonstrated that microbubble size and concentration strongly affect their acoustic behavior and contrast persistence (Talu, Hettiarachchi et al. 2007; Kaya, Feingold et al. 2009; Sirsi, Feshitan et al. 2010). To eliminate these effects, only size-isolated microbubble suspensions with the same concentration were used for the study. Large microbubbles have been shown to produce higher contrast enhancement with longer circulation persistence than the smaller ones (Sirsi, Feshitan et al. 2010; Streeter, Gessner et al. 2010). Because 4-5 μm microbubbles are presented in a freshly generated suspension with relatively higher concentration than 6-8 μm ones, they were chosen to be used as the size-selected sample for all injections (Feshitan, Chen et al. 2009). The perfusion data confirmed the size and concentration dependence by showing that all microbubble samples had similar contrast enhancement in the mouse kidneys regardless of their surface architecture or targeting ligand presentation (Figure 4.10).

A similar trend was observed for the effect of total gas volume injected on microbubble contrast enhancement and persistence based on data fitting using the one-compartment model (Figure 4.12): no correlation was found between either the signal amplitude or the persistence half-life and the total gas volume injected. This was expected since the total gas volume depended on the size distribution and concentration of the injected microbubble suspension. Sirsi et al. (Sirsi, Feshitan et al. 2010) have previously pointed out that the amount of contrast enhancement was not determined by the volume of gas that was injected, but rather how the gas was distributed within the microbubbles. Here, further evidence was shown, lending support to this conclusion (Figure 4.12).

On the other hand, the microbubble surface architecture affected their circulation persistence significantly (Figure 4.11). ELA Control showed significantly longer persistence

(both half-life and 25% time point) than ELA microbubbles, while BLA Control and BLA microbubbles had similar circulation time. The presence of RGD peptide on the surface of ELA microbubbles clearly shortened their persistence, and this was believed to be caused by the ligand-induced complement activation (see Chapter 3). Similar results were previously reported to link increased complement activation to increased elimination rate of liposomes from blood circulation (Ishida, Kojima et al. 2000; Huong, Ishida et al. 2001). The present data supported the hypothesis that the buried-ligand architecture could protect the targeting ligand from exposure to the surrounding environment and therefore prolonged the microbubble persistence by reducing their immunogenicity. The contrast elimination was further explored by fitting the TIC data to the one-compartment pharmacokinetic model and evaluating the k_2 parameter (Figure 4.13C). Significant faster elimination rate was observed for ELA microbubbles than ELA Control, while no difference was detected between BLA and BLA Control.

A more sophisticated two-compartment model was also used to further differentiate the mechanisms of microbubble clearance during circulation (Figure 4.15). The value of k_2 parameter (Figure 4.15B), the elimination rate of contrast signal from circulation, was significantly higher for ELA microbubbles compared to ELA Control, once again, indicating that targeted ELA microbubbles were cleared from the system much faster. More importantly, no significant difference was detected in the value of k_3 parameter (Figure 4.15C), the rate at which microbubbles became adherent in the kidney, in comparison to ELA Control. This result clarifies that the reason of the fast clearance for ELA microbubbles was not due to passive accumulation or non-specific adhesion, but rather caused by other mechanisms, such as active clearance by the MPS. On the other hand, the total elimination rate of BLA microbubbles was not increased due to the presence of the RGD peptide in comparison to BLA Control. Once

again, these results were consistent with the protective role of the PEG overbrush. It is important to note that targeted BLA microbubbles could potentially trigger complement activation while remaining long circulating. It is possible that the complement immune system was still activated after injection. However, the presence of the PEG overbrush physically inhibited the accessibility of macrophages to the opsonins and thus protected the contrast agents from elimination.

It has been reported that repeated injection of "empty" PEGylated liposomes led to accelerated blood clearance phenomenon of the second dose of liposomes even when the injections were spaced by a few days (Ishida and Kiwada 2008). Interestingly, the same phenomenon was not observed in the present experiment when control microbubbles (ELA or BLA) were injected in the "pre-exposed" mice with only one day apart. This may be explained by several factors. First, PEGylated liposomes can circulate in blood on the order of days, much longer than microbubbles. This gives them more chance to be in contact with the MPS for potential immune recognition. Second, the current microbubble injections were repeated in the same animal only one day apart. This short "resting" period might not be enough for the production of antibodies for microbubble elimination before the second injection was given. A longitudinal study will be required, however, in order to fully understand the impact of repeated injection of targeted contrast agents on their circulation persistence.

The buried-ligand architecture design clearly improved the circulation persistence of targeted contrast agents when compared with the exposed-ligand architecture design (68% reduction in persistence half-life for ELA microbubbles in comparison with 4% reduction for BLA microbubbles based on results shown in Figure 4.11A). When combined with USRF, the stealth microbubble construct offers both spatial and temporal control of selective adhesion

(Borden, Zhang et al. 2008). By utilizing BLA microbubbles for targeted molecular imaging applications, the need for dwell time after injection can be potentially eliminated because of the triggered binding at the targeted site. In addition, BLA microbubbles showed longer circulation persistence, which could increase the binding efficiency since the probability of targeted adhesion is directly proportional to the number of passes of microbubbles through the circulatory system. Since there seems likely to be a tradeoff between the imaging wait time and binding efficiency, using size-selected BLA microbubbles for targeted molecular imaging applications could potentially improve the imaging protocol significantly.

4.5. Conclusion

Microbubbles with various surface architectures were generated and size selected using the differential centrifugation technique. RGD peptide was conjugated to the surface as the targeting ligand using a post-labeling technique. The contrast enhancement and circulation persistence of these microbubbles were delineated from images of the mouse kidneys using a high frequency ultrasound scanner at 40 MHz. For the same injected concentration, microbubbles with various surface architectures produced similar contrast enhancement regardless of the presentation of the targeting ligands on the surface. However, their contrast persistence was highly affected by the PEG brush architecture. Targeting ligand inducing complement activation resulted in shortened circulation time for ELA microbubbles significantly when compared to ELA Control (68% reduction in persistence half-life). On the other hand, the buried-ligand architecture successfully protected the RGD peptide from exposure to the surrounding environment and thus prolonged the bloodstream persistence, as evidenced by the

almost identical persistence time. No accelerated blood clearance phenomenon was observed for repeated microbubble injections in pre-exposed mice when the injections were only one day apart. The data presented here could potentially change the protocol of targeted molecular imaging when the stealth microbubble design is utilized.

Chapter 5: Concluding Remarks and Future Directions

5.1. Accomplishment of Specific Aims

5.1.1. Ligand Conjugation to Bimodal PEG Brushes on Microbubbles

The difference between ligand diffusion and binding to the monolayer shell of microbubbles was studied using various poly(ethylene glycol) (PEG) brush architectures, ligand sizes and binding modes. Microbubbles were pre-formed using high-speed amalgamation technique, and two fluorescently labeled ligands with vast molecular weight difference were conjugated to the microbubbles. The ligand diffusion and binding rate was monitored by measuring the median fluorescence intensity change over time using flow cytometry.

Two binding phenomena were observed. For microbubbles with a bimodal PEG brush layer on the surface, the diffusion and conjugation of small molecules, such as NHS-FITC with molecular weight <1 kDa, was not affected due to the PEG overbrush. The ligand binding kinetics was the same between ELA and BLA microbubbles. On the other hand, for macromolecules, such as SA-FITC with molecular weight >10 kDa, the diffusion and binding rate was significantly changed: BLA microbubbles showed a much slower binding kinetics than their ELA counterparts. This phenomenon was believed to be caused due to the steric hindrance effect of the flexible PEG chains. The diffusion of macromolecules was partially inhibited because of the excluded volume of the PEG brushes. The binding of SA-FITC to BLA microbubbles suggested a possible phase separation between lipid species on the monolayer surface, leading to populations of revealed and concealed ligands. In addition, flow cytometry allowed the binding kinetics data to be analyzed based on microbubble size. It was found that

ligand conjugation kinetics was independent of microbubble size, regardless of ligand size or microbubble architectures. These results demonstrated the feasibility of post-labeling for small ligands to BLA microbubbles to generate stealth targeted ultrasound contrast agents.

Epi-fluorescence microscopy was utilized to visually confirm ligand conjugation to the surface of microbubbles. Streptavidin-induced structure formation (e.g., folds and protrusions) on ELA microbubbles was observed for the first time. Instead of using mechanical pressurization, complex surface structures were obtained simply through multivalent ligand binding. It was proposed that this phenomenon may be correlated to flow cytometry scattering measurements.

5.1.2. Microbubble-Induced Complement Activation *In Vitro*

The role of PEG brush architectures on microbubble-induced complement activation *in vitro* was studied using human complement-preserved serum. The post-labeling technique was utilized to generate targeted ELA and BLA microbubbles with various PEG brush architectures using RGD peptide conjugated to the surface as the targeting ligand, and the degree of complement activation was quantified by measuring complement C3/C3 binding using flow cytometry.

The stability of microbubbles in human serum was examined, and it was shown that microbubbles, regardless of their surface architecture or the presence of targeting ligands, were stable for at least 2 hrs at physiological conditions. Human serum factor binding test showed that complement component C3/C3b, in comparison to human serum albumin and immunoglobulin G, was the only protein that significantly bound to targeted microbubbles. For

ELA microbubbles, complement C3/C3b binding was directly correlated to the amount of RGD peptide on the surface: increased amount of RGD induced more complement C3/C3b binding. On the other hand, this direct correlation was not observed for BLA microbubbles: when the amount of RGD peptide was increased by 2 orders of magnitude, no significant increase of complement C3/C3b binding to BLA microbubbles was measured. The amount of C3/C3b binding was also proportional to microbubble surface area: larger targeted microbubbles induced more complement activation. This most likely was due to the increased RGD peptide presentation on the surface as well. Control microbubbles without any targeting ligand showed complement C3/C3b binding too, though the amount was much less when compared to targeted microbubbles. This finding suggested that the underlying phospholipid species could trigger complement recognition and induce potential immune response. The effect of the surface architecture on complement activation was further studied by comparing C3/C3b binding to targeted microbubbles with the same amount of RGD conjugated to the surface but with different PEG brush heights. It was found that the PEG brush height is directly correlated to complement binding: the higher the PEG overbrush, the more it could shield the targeted ligand from exposure and thus reduce complement recognition. Finally, the effect of microbubble surface charge was investigated, and it was shown that the negative charge on the microbubbles induced complement C3/C3b binding. This data supported the notion that the negative charge associated with the phosphate group in DSPE-PEG2000 played a critical role in complement activation.

5.1.3. Targeted Microbubble *In Vivo* Perfusion Imaging

The contrast enhancement and circulation persistence of targeted microbubbles with various surface architectures was studied in mouse kidneys using a high frequency ultrasound scanner with a 40 MHz transducer. Similar to the previous experiments, microbubbles were pre-formed and the RGD peptide was conjugated to the microbubble surface using a post-labeling technique. Because of the strong dependence of microbubble acoustic properties on the diameters, 4-5 μm size-isolated microbubbles were used for this study. In order to avoid complement activation induced by repeated microbubble injections, only one bolus injection was done per animal per day. A one-compartment pharmacokinetic model was used to fit the contrast intensity data in order to quantify signal enhancement and circulation time. It was found that the contrast enhancement of microbubbles was not affected by their PEG brush architectures or the presence of targeting ligands on the surface. The ability of microbubbles to increase the contrast of ultrasound images was only dependent on their size distribution and concentration. However, the persistence half-life was strongly affected by the PEG overbrush: ELA microbubbles showed a significantly reduced circulation time when compared to ELA Control, while BLA and BLA Control showed comparable persistence half-lives. This data suggested the ability of the buried-ligand architecture to prolong targeted microbubble bloodstream circulation by inhibiting complement recognition and surface fixation. These findings strongly supported the hypothesis that targeted microbubbles with the buried-ligand architecture could reduce the immunogenicity and prolong their circulation persistence without compromising their contrast enhancement ability.

5.2. Impact on the Field

Previous studies have suggested that polymer brushes could retard the diffusion of large molecules to the PEG grafted surface due to their excluded volume. This effect has become the design base of long circulating Stealth liposomes and many other colloidal particles. Following the same principles, PEG chains are incorporated into the monolayer shell of microbubbles in order to form a steric barrier against coalescence and macromolecule surface adsorption. However, for targeted molecular imaging applications, the surface functionalization is typically done by conjugating the targeted ligands at the distal end of the PEG chains, and the presence of these specific ligands on the surface could trigger immune response and decrease their circulation time. In order to avoid these undesired effects, a bimodal PEG brush layer with the buried-ligand architecture (BLA) is designed to generate stealth microbubbles with improved binding selectivity, decreased immunogenicity and prolonged circulation persistence.

The ligand conjugation study reveals great insight into the role of the PEG brush layer on molecular diffusion and binding to the monolayer surface of microbubbles with various surface architectures. The ability to inhibit ligand diffusion and binding by PEG chains has been shown previously by Needham et al. (Needham, Zhelev et al. 1999). The present study, however, shed new light on the binding of solutes to tethered groups in various brush architectures on the surface of microbubbles. Evidence is shown to confirm that BLA microbubbles indeed partially prevented the binding of macromolecules (molecular weight >10 kDa) to the bimodal PEG grafted surface while allowing the uninhibited attachment of small ones (molecular weight < 1 kDa). This finding demonstrates the feasibility of utilizing the post-labeling technique for generating targeted contrast agents using small ligands, such as peptides, and provides the basis for translating this platform strategy for large-scale production of targeted contrast agents.

Perhaps more importantly, it provides insights for fundamental tethered ligand-receptor interactions at grafted Langmuir-monolayer surfaces. For example, one could engineer the polymer surface coverage density and chain length in order to achieve the desired overbrush height so that ligand conjugation is only possible for molecules within a certain size limit. This strategy could be developed to utilize BLA microbubble as a separation platform for selective molecular binding in solution.

The most unexpected result comes from the observation that, for the first time, complex microstructures on the surface of microbubbles are induced simply via streptavidin-biotin binding. Fluorescence microscopy provides direct confirmation of these wrinkled structures that are normally not detected for microbubbles bound to other small ligands. Furthermore, the percentage of microbubbles in a given suspension that deviate from the normal spherical shape can be quantified using flow cytometry.

The *in vitro* immunogenicity and *in vivo* contrast persistence experiments are the next steps in showing the advantage of having the buried-ligand architecture as the stealth microbubble design over the exposed-ligand architecture (ELA). By measuring the binding of complement component C3/C3b to targeted microbubbles *in vitro*, complement activation is quantified. The study clearly shows the correlation between targeting ligand concentration and complement activation: the higher RGD peptides are presented on the surface of microbubbles, the more C3/C3b binding occurs. However, this phenomenon is not observed for BLA microbubbles, suggesting the ability of the PEG overbrush to shield the targeting ligand from exposure to the surrounding environment and therefore decrease the microbubble immunogenicity. This protective role is further illustrated by tailoring the length of the PEG chains and showed that complement activation is directly related to the PEG overbrush height.

In the *in vivo* experiments, by measuring the contrast persistence of targeted microbubbles with various PEG brush architectures in mouse kidneys, it is clearly shown that BLA microbubbles are more stable during circulation in comparison to their ELA counterparts. This work provides the most direct confirmation of the advantage for utilizing BLA design to generate stealth microbubbles for targeted molecular imaging applications.

5.3. Future Directions

The most obvious extension of the present work is to study the effect of the buried-ligand architecture on microbubble contrast persistence *in vivo* longitudinally. In order to translate the stealth BLA microbubble design for molecular imaging studies, it is extremely important to know the "long term" effect of the targeted microbubbles since repeated injection is most likely required for these applications. A direct comparison between ELA and BLA microbubble circulation persistence after repeated injections in both healthy and diseased animal models could provide further evidence to support the utilization of BLA design to generate targeted ultrasound contrast agents.

Furthermore, it is relevant to study the adhesion efficiency of targeted BLA microbubbles. It is essential to create a stealth targeted contrast agent on which the ligand does not increase complement activation or other immunogenic factors. Yet, it is equally important to show that the contrast agent could firmly adhere to a target site with high selectivity and remains echogenic for subsequently imaging. In addition, the effect of the ultrasound radiation force on BLA microbubbles adhesion to target sites during shear flow needs to be studied as well in order to

optimize the acoustic parameters for transient activation of these stealth microbubble contrast agents.

References

Ago, K., K. Nagasawa, et al. (2005). "Development of an aerobic cultivation system by using a microbubble aeration technology." Journal of Chemical Engineering of Japan **38**(9): 757-762.

Basilico, R., M. J. K. Blomley, et al. (2002). "The first phase I study of a novel ultrasound contrast agent (BR14): Assessment of safety and efficacy in liver and kidneys." Academic Radiology **9**: S380-S381.

Becker, H. and P. N. Burns (2000). Handbook fo contrast echocardiography. Berlin, Springer.

Bird, R. B., W. E. Stewart, et al. (2002). Transport Phenomena. New York, John Wiley & Sons, Inc.

Birshtein, T. M., Y. V. Liatskaya, et al. (1990). "Theory of supermolecular structures of polydisperse block copolymers: 1. Planar layers of grafted chains." Polymer **31**(11): 2185-2196.

Blanchard, D. C. (1975). "Bubble scavenging and water-to-air transfer of organic material in sea." Advances in Chemistry Series(145): 360-387.

Bohmer, M. R., R. Schroeders, et al. (2006). "Preparation of monodisperse polymer particles and capsules by ink-jet printing." Colloids and Surfaces a-Physicochemical and Engineering Aspects **289**(1-3): 96-104.

Borden, M. A. and P. A. Dayton (2008). Targeted ultrasound contrast agents. Molecular Imaging in Oncology. M. G. Pomper and J. G. Gelovani. New York, Informa Healthcare USA, Inc. **1:** 329.

Borden, M. A., G. V. Martinez, et al. (2006). "Lateral phase separation in lipid-coated microbubbles." Langmuir **22**(9): 4291-4297.

Borden, M. A., G. Pu, et al. (2004). "Surface phase behavior and microstructure of lipid/PEG-emulsifier monolayer-coated microbubbles." Colloids and Surfaces B-Biointerfaces **35**(3-4): 209-223.

Borden, M. A., S. Qin, et al. (2010). Ultrasound Contrast Agents. Molecular Imaging: Principles and Practice. R. Weissleder, B. D. Ross, A. Rehemtulla and S. S. Gambhir. Shelton, People's Medical Publishing House**:** 1359.

Borden, M. A., M. R. Sarantos, et al. (2006). Ultrasound radiation force modulates ligand availability on targeted contrast agents, B C Decker Inc.

Borden, M. A., H. Zhang, et al. (2008). "A stimulus-responsive contrast agent for ultrasound molecular imaging." Biomaterials **29**(5): 597-606.

Calliada, F., R. Campani, et al. (1998). "Ultrasound contrast agents - Basic principles." European Journal of Radiology **27**: S157-S160.

Cassell, E. A., K. M. Kaufman, et al. (1975). "Effects of bubble size on microflotation." Water Research **9**(12): 1017-1024.

Chen, C. C. and M. A. Borden (2010). "Ligand conjugation to bimodal poly(ethylene glycol) brush layers on microbubbles." Langmuir **26**(16): 13183-13194.

Chen, C. C. and E. E. Dormidontova (2005). "Architectural and structural optimization of the protective polymer layer for enhanced targeting." Langmuir **21**(12): 5605-5615.

Chen, G. H. (2004). "Electrochemical technologies in wastewater treatment." Separation and Purification Technology **38**(1): 11-41.

Chonn, A., P. R. Cullis, et al. (1991). "The role of surface-charge in the activation of the classical and alternative pathways of complement by liposomes." Journal of Immunology **146**(12): 4234-4241.

Cooper, J. M., J. Shen, et al. (1994). "The imaging of streptavidin and avidin using scanning-tunneling-microscopy." Journal of Materials Science-Materials in Electronics **5**(2): 106-110.

Cosgrove, D. and C. Harvey (2009). "Clinical uses of microbubbles in diagnosis and treatment." Medical & Biological Engineering & Computing **47**(8): 813-826.

Crum, L. A. (1975). "Bjerknes forces on bubbles in a stationary sound field." Journal of the Acoustical Society of America **57**(6): 1363-1370.

D'Andrea, L. D., A. Del Gatto, et al. (2006). "Peptide-based molecules in angiogenesis." Chemical Biology & Drug Design **67**(2): 115-126.

D'Arrigo, J. S. (2003). Stable gas-in-liquid emulsions: production in natural waters and artificial media. Amsterdam, Elsevier Science B.V.

Dan, N. and M. Tirrell (1993). "Effect of bimodal molecular-weight distribution on the polymer brush." Macromolecules **26**(24): 6467-6473.

Dayton, P., A. Klibanov, et al. (1999). "Acoustic radiation force in vivo: A mechanism to assist targeting of microbubbles." Ultrasound in Medicine and Biology **25**(8): 1195-1201.

Dayton, P. A., J. S. Allen, et al. (2002). "The magnitude of radiation force on ultrasound contrast agents." Journal of the Acoustical Society of America **112**(5): 2183-2192.

Dayton, P. A. and M. Borden (2008). Ultrasound Instrumentation and Techniques. Molecular Imaging in Oncology. M. G. Pomper and J. G. Gelovani. New York, Informa Healthcare USA, Inc. **1:** 718.

Dayton, P. A. and K. W. Ferrara (2002). "Targeted imaging using ultrasound." Journal of Magnetic Resonance Imaging **16**(4): 362-377.

Dayton, P. A., K. E. Morgan, et al. (1997). "A preliminary evaluation of the effects of primary and secondary radiation forces on acoustic contrast agents." Ieee Transactions on Ultrasonics Ferroelectrics and Frequency Control **44**(6): 1264-1277.

Dayton, P. A. and J. J. Rychak (2007). "Molecular ultrasound imaging using microbubble contrast agents." Frontiers in Bioscience **12**: 5124-5142.

de Gennes, P. G. (1980). "Conformations of polymers attached to an interface." Macromolecules **13**(5): 1069-1075.

de Jong, N., M. Emmer, et al. (2009). "Ultrasonic characterization of ultrasound contrast agents." Medical & Biological Engineering & Computing **47**(8): 861-873.

de Jong, N., L. Hoff, et al. (1992). "Absorption and scatter of encapsulated gas filled microsphere - theoretical considerations and some measurements." Ultrasonics **30**(2): 95-103.

Dean, R. B. (1944). "The formation of bubbles." Journal of Applied Physics **15**(5): 446-451.

Deshpande, N., M. A. Pysz, et al. (2010). "Molecular ultrasound assessment of tumor angiogenesis." Angiogenesis **13**(2): 175-188.

Dhoot, S., H. Watanabe, et al. (1994). "Measurement of forces in interactions between bimodal layers of diblock copolymers adsorbed on mica." Colloids and Surfaces a-Physicochemical and Engineering Aspects **86**: 47-60.

du Toit, L. C., T. Govender, et al. (2011). "Investigating the Effect of Polymeric Approaches on Circulation Time and Physical Properties of Nanobubbles." Pharmaceutical Research **28**(3): 494-504.

Feinstein, S. B., P. M. Shah, et al. (1984). "Microbubble dynamics visualized in the intact capillary circulation." Journal of the American College of Cardiology **4**(3): 595-600.

Feinstein, S. B., F. J. Tencate, et al. (1984). "Two-dimensional contrast echocardiography. 1. in vitro development and quantitative analysis of echo contrast agents." Journal of the American College of Cardiology **3**(1): 14-20.

Ferrante, E. A., J. E. Pickard, et al. (2009). "Dual targeting improves microbubble contrast agent adhesion to VCAM-1 and P-selectin under flow." Journal of Controlled Release **140**(2): 100-107.

Ferrara, K., R. Pollard, et al. (2007). "Ultrasound microbubble contrast agents: fundamentals and application to gene and drug delivery." Annual Review of Biomedical Engineering **9**: 415-447.

Feshitan, J. A., C. C. Chen, et al. (2009). "Microbubble size isolation by differential centrifugation." J Colloid Interface Sci **329**(2): 316-24.

Fisher, N. G., J. P. Christiansen, et al. (2002). "Influence of microbubble surface charge on capillary transit and myocardial contrast enhancement." Journal of the American College of Cardiology **40**(4): 811-819.

Fisher, N. G., J. P. Christiansen, et al. (2002). "Myocardial and microcirculatory kinetics of BR14, a novel third-generation intravenous ultrasound contrast agent." Journal of the American College of Cardiology **39**(3): 530-537.

Fox, F. E. and K. F. Herzfeld (1954). "Gas bubbles with organic skin as cavitation nuclei." Journal of the Acoustical Society of America **26**(6): 984-989.

Gattinoni, L., E. Carlesso, et al. (2011). "Assessing gas exchange in acute lung injury/acute respiratory distress syndrome: diagnostic techniques and prognostic relevance." Current Opinion in Critical Care **17**(1): 18-23.

Gillam, L. D., S. Kaul, et al. (1985). "Functional and pathologic effects of multiple echocardiographic contrast injections on the myocardium, brian and kidney." Journal of the American College of Cardiology **6**(3): 687-694.

Goedel, W. A., C. Luap, et al. (1999). "Stratification in monolayers of a bidisperse melt polymer brush as revealed by neutron reflectivity." Macromolecules **32**(22): 7599-7609.

Gorce, J. M., M. Arditi, et al. (2000). "Influence of bubble size distribution on the echogenicity of ultrasound contrast agents - A study of SonoVue (TM)." Investigative Radiology **35**(11): 661-671.

Gramiak, R. and P. M. Shah (1968). "Echocardiography of the aortic root." Invest Radiol **3**(5): 356-66.

Greis, C. (2008). Contrast Media, Ultrasound, Commercial Products. Encyclopedia of Diagnostic Imaging. A. L. Baert. Leuven, Springer. **1:** 547.

Harashima, H., K. Sakata, et al. (1994). "Enhanced hepatic-uptake of liposomes through complement activation depending on the size of liposomes." Pharmaceutical Research **11**(3): 402-406.

Hargreaves, R. J. (2008). "The role of molecular imaging in drug discovery and development." Clin Pharmacol Ther **83**(2): 349-53.

Harvey, E. N., A. H. Whiteley, et al. (1944). "Bubble formation in animals II. Gas nuclei and their distribution in blood and tissues." Journal of Cellular and Comparative Physiology **24**(1): 23-34.

Hollinshead, C. M., R. D. Harvey, et al. (2009). "Effects of Surface Pressure on the Structure of Distearoylphosphatidylcholine Monolayers Formed at the Air/Water Interface (dagger)." Langmuir.

Huong, T. M., T. Ishida, et al. (2001). "Species difference in correlation between in vivo/in vitro liposome-complement interactions." Biological & Pharmaceutical Bulletin **24**(4): 439-441.

Iagaru, A., X. Chen, et al. (2007). "Molecular imaging can accelerate anti-angiogenic drug development and testing." Nat Clin Pract Oncol **4**(10): 556-7.

Immordino, M. L., F. Dosio, et al. (2006). "Stealth liposomes: review of the basic science, rationale, and clinical applications, existing and potential." International Journal of Nanomedicine **1**(3): 297-315.

Ishida, T. and H. Kiwada (2008). "Accelerated blood clearance (ABC) phenomenon upon repeated injection of PEGylated liposomes." International Journal of Pharmaceutics **354**(1-2): 56-62.

Ishida, T., H. Kojima, et al. (2000). "Biodistribution of liposomes and C3 fragments associated with liposomes: evaluation of their relationship." International Journal of Pharmaceutics **205**(1-2): 183-193.

Israelachvili, J. N. (1991). Intermolecular and Surface Forces. London, Elsevier.

Janssen, B. J. C., E. G. Huizinga, et al. (2005). "Structures of complement component C3 provide insights into the function and evolution of immunity." Nature **437**(7058): 505-511.

Jeppesen, C., J. Y. Wong, et al. (2001). "Impact of polymer tether length on multiple ligand-receptor bond formation." Science **293**(5529): 465-468.

Johnson, B. D. and R. C. Cooke (1980). "Organic particle and aggregate formation resulting from the dissolution of bubbles in seawater." Limnology and Oceanography **25**(4): 653-661.

Johnson, B. D. and R. C. Cooke (1981). "Generation of stablized microbubbles in seawater." Science **213**(4504): 209-211.

Kabalnov, A., D. Klein, et al. (1998). "Dissolution of multicomponent microbubbles in the bloodstream: 1. Theory." Ultrasound in Medicine and Biology **24**(5): 739-749.

Kaufmann, B. A., K. Wei, et al. (2007). "Contrast echocardiography." Current Problems in Cardiology **32**(2): 51-96.

Kaya, M., S. Feingold, et al. (2009). Acoustic characterization of individual monodisperse contrast agents with an optical-acoustical system. Proceedings of the 2009 IEEE Ultrasonics Symposium, Rome.

Kemper, A. J., J. E. Oboyle, et al. (1983). "Hydrogen peroxide contrast-enhanced two-dimensional echocardiography: real-time in vivo delineation of regional myocardial perfusion." Circulation **68**(3): 603-611.

Kenworthy, A. K., K. Hristova, et al. (1995). "Range and magnitude of the steric pressure between bilayers containing phospholipids with covalently attached poly(ethylene glycol)." Biophys J **68**(5): 1921-36.

Kim, D. H., M. J. Costello, et al. (2003). "Mechanical properties and microstructure of polycrystalline phospholipid monolayer shells: Novel solid microparticles." Langmuir **19**(20): 8455-8466.

Kim, D. H., A. L. Klibanov, et al. (2000). "The influence of tiered layers of surface-grafted poly(ethylene glycol) on receptor-ligand-mediated adhesion between phospholipid monolayer-stabilized microbubbles and coated class beads." Langmuir **16**(6): 2808-2817.

Kim, S. H. and E. I. Franses (2005). "New protocols for preparing dipalmitoylphosphatidylcholine dispersions and controlling surface tension and competitive adsorption with albumin at the air/aqueous interface." Colloids and Surfaces B-Biointerfaces **43**(3-4): 256-266.

Kitzman, D. W., M. E. Goldman, et al. (2000). "Efficacy and safety at the novel ultrasound contrast agent Perflutren (definity) in patients with suboptimal baseline left ventricular echocardiographic images." American Journal of Cardiology **86**(6): 669-674.

Klibanov, A. L. (1999). "Targeted delivery of gas-filled microspheres, contrast agents for ultrasound imaging." Adv Drug Deliv Rev **37**(1-3): 139-157.

Klibanov, A. L. (2005). "Ligand-carrying gas-filled microbubbles: Ultrasound contrast agents for targeted molecular imaging." Bioconjugate Chemistry **16**(1): 9-17.

Klibanov, A. L. (2009). "Preparation of targeted microbubbles: ultrasound contrast agents for molecular imaging." Medical & Biological Engineering & Computing **47**(8): 875-882.

Klibanov, A. L., K. Maruyama, et al. (1990). "Amphipathic polyethyleneglycols effectively prolong the circulation time of liposomes." FEBS Lett **268**(1): 235-7.

Klibanov, A. L., P. T. Rasche, et al. (2004). "Detection of individual microbubbles of ultrasound contrast agents - Imaging of free-floating and targeted bubbles." Investigative Radiology **39**(3): 187-195.

Kojima, H. (2010). Microbubble generator used in e.g. ballast water processing apparatus, mixes and introduces jet stream of gas-liquid multiphase flow and gas injected from gas injection portion into gas-liquid mixing portion to generate microbubble, MU CO LTD (MUMU-Non-standard)**:** 39.

Kraizman, M. A. (1974). Electroflotation of sewage or mineral pulp - pulse train of electric current to electrodes ensures optimum flotation conditions, M A Kraizman et al. (KRAI-Individual).

Kuhl, T. L., D. E. Leckband, et al. (1995). Modulation and modeling of interaction forces between lipid bilayers exposing terminally grafted polymer chains. Stealth Liposomes. D. Lasic and F. Martin. Boca Raton, CRC Press**:** 73.

Kuhlman, W., I. Taniguchi, et al. (2007). "Interplay between PEO tether length and ligand spacing governs cell spreading on RGD-modified PMMA-g-PEO comb copolymers." Biomacromolecules **8**(10): 3206-3213.

Kvale, S., H. A. Jakobsen, et al. (1996). "Size fractionation of gas-filled microspheres by flotation." Separations Technology **6**(4): 219-226.

Lai, P. Y. and E. B. Zhulina (1992). "Structure of a bidisperse polymer brush: Monte Carlo simulation and self-consistent field results." Macromolecules **25**(20): 5201-5207.

Lang, R. M., K. M. Borow, et al. (1987). "Effect of intracoronary injections of sonicated microbubbles on left-ventricular contractility." American Journal of Cardiology **60**(1): 166-171.

Langmuir, I. (1917). "The constitution and fundamental properties of solids and liquids. II. Liquids." Journal of the American Chemical Society **39**: 1848-1906.

Lanza, G. M. and S. A. Wickline (2001). "Targeted ultrasonic contrast agents for molecular imaging and therapy." Progress in Cardiovascular Diseases **44**(1): 13-31.

Lee, D. J., A. Lyshchik, et al. (2008). "Relationship between retention of a vascular endothelial growth factor receptor 2 (VEGFR2)-targeted ultrasonographic contrast agent and the level of VEGFR2 expression in an in vivo breast cancer model." Journal of Ultrasound in Medicine **27**(6): 855-866.

Leong-Poi, H., J. Song, et al. (2002). "Influence of microbubble shell properties on ultrasound signal: Implications for low-power perfusion imaging." Journal of the American Society of Echocardiography **15**(10): 1269-1276.

Levicky, R., N. Koneripalli, et al. (1998). "Stratification in bidisperse polymer brushes from neutron reflectivity." Macromolecules **31**(8): 2616-2621.

Lim, A. K. P., N. Patel, et al. (2004). "Evidence for spleen-specific uptake of a microbubble contrast agent: a quantitative study in healthy volunteers." Radiology **231**(3): 785-788.

Lindner, J. R. (2004). "Molecular imaging with contrast ultrasound and targeted microbubbles." Journal of Nuclear Cardiology **11**(2): 215-221.

Lindner, J. R. (2009). "Contrast ultrasound molecular imaging of inflammation in cardiovascular disease." Cardiovascular Research **84**(2): 182-189.

Lindner, J. R., P. A. Dayton, et al. (2000). "Noninvasive imaging of inflammation by ultrasound detection of phagocytosed microbubbles." Circulation **102**(5): 531-538.

Lindner, J. R., J. Song, et al. (2001). "Ultrasound assessment of inflammation and renal tissue injury with microbubbles targeted to P-selectin." Circulation **104**(17): 2107-2112.

Liu, X. Y., L. M. Ruan, et al. (2010). "Preparation of RGD-modified long circulating liposome loading matrine, and its in vitro anti-cancer effects." International Journal of Medical Sciences **7**(4): 197-208.

Lodish, H., A. Berk, et al. (2008). Molecular Cell Biology. New York, W. H. Freeman and Company.

Longo, G. S., D. H. Thompson, et al. (2008). "Ligand-receptor interactions between surfaces: The role of binary polymer spacers." Langmuir **24**(18): 10324-10333.

Lozano, M. M. and M. L. Longo (2009). "Complex formation and other phase transformations mapped in saturated phosphatidylcholine/DSPE-PEG2000 monolayers." Soft Matter **5**(9): 1822-1834.

Lozano, M. M. and M. L. Longo (2009). "Microbubbles Coated with Disaturated Lipids and DSPE-PEG2000: Phase Behavior, Collapse Transitions, and Permeability." Langmuir.

Lyshchik, A., A. C. Fleischer, et al. (2007). "Molecular Imaging of vascular endothelial growth factor receptor 2 expression using targeted contrast-enhanced high-frequency ultrasonography." Journal of Ultrasound in Medicine **26**(11): 1575-1586.

Main, M. L., A. C. Ryan, et al. (2008). "Acute mortality in hospitalized patients undergoing echocardiography with and without an ultrasound contrast agent (multicenter registry results in 4,300,966 consecutive patients)." American Journal of Cardiology **102**(12): 1742-1746.

Mancini, M., A. Greco, et al. (2009). "Ultrasound molecular imaging by targeted microbubble contrast agents." Minerva Biotecnologica **21**(2): 97-110.

McCulloch, M., C. Gresser, et al. (2000). "Ultrasound contrast physics: A series on contrast echocardiography, article 3." Journal of the American Society of Echocardiography **13**(10): 959-967.

Miller, D. L., M. A. Averkiou, et al. (2008). "Bioeffects considerations for diagnostic ultrasound contrast agents." Journal of Ultrasound in Medicine **27**(4): 611-632.

Miller, J. C., H. H. Pien, et al. (2005). "Imaging angiogenesis: applications and potential for drug development." J Natl Cancer Inst **97**(3): 172-87.

Moghimi, S. M., A. J. Andersen, et al. (2010). "Complement activation cascade triggered by PEG-PL engineered nanomedicines and carbon nanotubes: the challenges ahead." Journal of Controlled Release **146**(2): 175-181.

Moghimi, S. M. and I. Hamad (2008). "Liposome-mediated triggering of complement cascade." Journal of Liposome Research **18**(3): 195-209.

Moghimi, S. M., I. Hamad, et al. (2006). "Methylation of the phosphate oxygen moiety of phospholipid-methoxy(polyethylene glycol) conjugate prevents PEGylated liposome-mediated complement activation and anaphylatoxin production." Faseb Journal **20**(14): 2591-+.

Moghimi, S. M., I. Hamad, et al. (2006). "Activation of the human complement system by cholesterol-rich and pegylated liposomes - modulation of cholesterol-rich liposome-mediated complement activation by elevated serum LDL and HDL levels." Journal of Liposome Research **16**(3): 167-174.

Moghimi, S. M. and J. Szebeni (2003). "Stealth liposomes and long circulating nanoparticles: critical issues in pharmacokinetics, opsonization and protein-binding properties." Progress in Lipid Research **42**(6): 463-478.

Moore, C. A., M. L. Smucker, et al. (1986). "Myocardial contrast echocardiography in humans. 1. Safety - A comparison with routine coronary arteriography." Journal of the American College of Cardiology **8**(5): 1066-1072.

Moore, N. W. and T. L. Kuhl (2006). "Bimodal polymer mushrooms: compressive forces and specificity toward receptor surfaces." Langmuir **22**(20): 8485-8491.

Moore, N. W., D. J. Mulder, et al. (2008). "Adhesion from tethered ligand-receptor bonds with microsecond lifetimes." Langmuir **24**(4): 1212-1218.

Mosqueira, V. C. F., P. Legrand, et al. (2001). "Relationship between complement activation, cellular uptake and surface physicochemical aspects of novel PEG-modified nanocapsules." Biomaterials **22**(22): 2967-2979.

Mullin, L., R. Gessner, et al. (2011). "Effect of anesthesia carrier gas on in vivo circulation times of ultrasound microbubble contrast agents in rats." Contrast Media & Molecular Imaging: 7.

Murphy, K., P. Travers, et al. (2008). Janeway's Immunobiology. New York, Garland Science, Taylor & Francis Group, LLC.

Nallamothu, R., G. C. Wood, et al. (2006). "A tumor vasculature targeted liposome delivery system for combretastatin A4: design, characterization, and in vitro evaluation." Aaps Pharmscitech **7**(2): 10.

Nam, J. and M. M. Santore (2007). "The adhesion kinetics of sticky vesicles in tension: The distinction between spreading and receptor binding." Langmuir **23**(21): 10650-10660.

Nam, J. and M. M. Santore (2007). "Adhesion plaque formation dynamics between polymer vesicles in the limit of highly concentrated binding sites." Langmuir **23**(13): 7216-7224.

Needham, D., D. V. Zhelev, et al. (1999). Surface Chemistry of the Sterically Stabilized PEG-Liposome. Liposomes: Rational design. J. A. New York**:** 13.

Noppl, D. A. and D. Needham (1996). "Avidin-biotin interactions at vesicle surfaces: Adsorption and binding, cross bridge formation, and lateral interactions." Biophysical Journal **70**(2): SU359-SU359.

Nyborg, W. L. (2006). Mechanisms for bioeffects of ultrasound relevant to therapeutic applications. Emerging Therapeutic Ultrasound. J. R. Wu and W. L. Nyborg. New Jersey, World Scientific Publishing Co. Pte. Ltd. **1:** 347.

Perkins, A. C., M. Frier, et al. (1997). "Human biodistribution of an ultrasound contrast agent (Quantison(TM)) by radiolabelling and gamma scintigraphy." British Journal of Radiology **70**(834): 603-611.

Phillips, W. T., R. W. Klipper, et al. (1999). "Polyethylene glycol-modified liposome-encapsulated hemoglobin: A long circulating red cell substitute." Journal of Pharmacology and Experimental Therapeutics **288**(2): 665-670.

Pohlman, R., B. Werden, et al. (1972). "Ultrasonic cleaning process - its dependence on energy density, time of action, temperature, and modulation of sonic field." Ultrasonics **10**(4): 156-&.

Quaia, E. (2005). Contrast Media in Ultrasonography. Berlin, Springer.

Quaia, E., M. J. K. Blomley, et al. (2002). "Initial observations on the effect of irradiation on the liver-specific uptake of Levovist." European Journal of Radiology **41**(3): 192-199.

Rani, S. A., B. Pitts, et al. (2005). "Rapid diffusion of fluorescent tracers into Staphylococcus epidermidis biofilms visualized by time lapse microscopy." Antimicrobial Agents and Chemotherapy **49**(2): 728-732.

Rychak, J. J., J. Graba, et al. (2007). "Microultrasound molecular imaging of vascular endothelial growth factor receptor 2 in a mouse model of tumor angiogenesis." Molecular Imaging **6**(5): 289-296.

Rychak, J. J., J. R. Lindner, et al. (2006). "Deformable gas-filled microbubbles targeted to P-selectin." Journal of Controlled Release **114**(3): 288-299.

Saltzman, W. M. (2001). Drug delivery: engineering principles for drug therapy. Oxford, Oxford University Press, Inc.

Schutt, E. G., D. H. Klein, et al. (2003). "Injectable microbubbles as contrast agents for diagnostic ultrasound imaging: the key role of perfluorochemicals." Angew Chem Int Ed Engl **42**(28): 3218-35.

Sessa, C., A. Guibal, et al. (2008). "Biomarkers of angiogenesis for the development of antiangiogenic therapies in oncology: tools or decorations?" Nature Clinical Practice Oncology **5**(7): 378-391.

Sirsi, S., J. Feshitan, et al. (2010). "Effect of microbubble size on fundamental mode high frequency ultrasound imaging in mice." Ultrasound in Medicine and Biology **36**(6): 935-948.

Sirsi, S., S. Hernandez, et al. (2011). "Polyplex-microbubble hybrids for ultrasound-targeted plasmid DNA delivery to solid tumors." Journal of Controlled Release **in submission**.

Sontum, P. C. (2008). "Physicochemical characteristics of Sonazoid (TM), a new contrast agent for ultrasound imaging." Ultrasound in Medicine and Biology **34**(5): 824-833.

Stapleton, S. (2007). Contrast enhanced high frequency ultrasound imaging of mice. Graduate Department of Medical Biophysics. Toronto, University of Toronto. **Master of Science:** 143.

Streeter, J. E., R. Gessner, et al. (2010). "Improving sensitivity in ultrasound molecular imaging by tailoring contrast agent size distribution: in vivo studies." Molecular Imaging **9**(2): 87-95.

Stride, E. and M. Edirisinghe (2008). "Novel microbubble preparation technologies." Soft Matter **4**(12): 2350-2359.

Stride, E. and M. Edirisinghe (2009). "Novel preparation techniques for controlling microbubble uniformity: a comparison." Medical & Biological Engineering & Computing **47**(8): 883-892.

Stride, E. and N. Saffari (2003). "Microbubble ultrasound contrast agents: a review." Proc Inst Mech Eng H **217**(6): 429-47.

Szebeni, J. (2005). "Complement activation-related pseudoallergy caused by amphiphilic drug carriers: the role of lipoproteins." Current Drug Delivery **2**: 7.

Szebeni, J. (2005). "Complement activation-related pseudoallergy: a new class of drug-induced acute immune toxicity." Toxicology **216**(2-3): 106-121.

Talu, E., K. Hettiarachchi, et al. (2008). "Maintaining monodispersity in a microbubble population formed by flow-focusing." Langmuir **24**(5): 1745-1749.

Talu, E., K. Hettiarachchi, et al. (2007). "Tailoring the size distribution of ultrasound contrast agents: Possible method for improving sensitivity in molecular imaging." Molecular Imaging **6**(6): 384-392.

Tanwir, K. and V. Tsoukanova (2008). "Lateral distribution of a poly(ethylene glycol)-grafted phospholipid in phosphocholine monolayers studied by epifluorescence microscopy." Langmuir **24**(24): 14078-87.

Tartis, M. S., D. E. Kruse, et al. (2008). "Dynamic microPET imaging of ultrasound contrast agents and lipid delivery." Journal of Controlled Release **131**(3): 160-166.

Toda, M., T. Kitazawa, et al. (2008). "Complement activation on surfaces carrying amino groups." Biomaterials **29**(4): 407-417.

Torchilin, V. P., M. I. Papisov, et al. (1995). Molecular Mechanism of Liposome and Immunoliposome Steric Protection with Poly(ethylene glycol): Theroretical and Experimental Proofs of the Role of Polymer Chain Flexibility. Stealth Liposomes. D. Lasic and F. Martin. Boca Raton, CRC Press, Inc.**:** 51.

Traganos, F. (1984). "Flow cytometry - principles and applications. 1." Cancer Investigation **2**(2): 149-163.

van Liew, H. D. and M. E. Burkard (1995). "Behavior of bubbles of slowly permeating gas used for ultrasonic imaging contrast." Investigative Radiology **30**(5): 315-321.

Villanueva, F. S., R. J. Jankowski, et al. (1998). "Microbubbles targeted to intercellular adhesion molecule-1 bind to activated coronary artery endothelial cells." Circulation **98**(1): 1-5.

Villanueva, F. S., R. J. Jankowski, et al. (1997). "Albumin microbubble adherence to human coronary endothelium: Implications for assessment of endothelial function using myocardial contrast echocardiography." Journal of the American College of Cardiology **30**(3): 689-693.

Walday, P., J. Ostensen, et al. (1994). "Albunex - a new ultrasound contrast agent - effects on hemodynamics, contrast and biodistribution in different species." Investigative Radiology **29**: S142-S144.

Walday, P., H. Tolleshaug, et al. (1994). "Biodistributions of air-filled albumin microspheres in rats and pigs." Biochemical Journal **299**: 437-443.

Walzog, B., D. Schuppan, et al. (1995). "THE leukocyte integrin Mac-1 (CD11B/CD18) contributes to binding of human granulocytes to collagen." Experimental Cell Research **218**(1): 28-38.

Willmann, J. K., Z. Cheng, et al. (2008). "Targeted microbubbles for imaging tumor angiogenesis: Assessment of whole-body biodistribution with dynamic micro-PET in mice." Radiology **249**(1): 212-219.

Willmann, J. K., R. H. Kimura, et al. (2010). "Targeted Contrast-Enhanced Ultrasound Imaging of Tumor Angiogenesis with Contrast Microbubbles Conjugated to Integrin-Binding Knottin Peptides." Journal of Nuclear Medicine **51**(3): 433-440.

Willmann, J. K., A. M. Lutz, et al. (2008). "Dual-targeted contrast agent for US assessment of tumor angiogenesis in vivo." Radiology **248**(3): 936-944.

Wilson, S. R., L. D. Greenbaum, et al. (2009). "Contrast-enhanced ultrasound: what is the evidence and what are the obstacles?" American Journal of Roentgenology **193**(1): 55-60.

Wong, J. Y., T. L. Kuhl, et al. (1997). "Direct measurement of a tethered ligand-receptor interaction potential." Science **275**(5301): 820-2.

Wu, Y., C. Cain-Hom, et al. (2010). "Therapeutic antibody targeting of individual Notch receptors." Nature **464**(7291): 1052-U122.

Xu, S. Q., Z. H. Nie, et al. (2005). "Generation of monodisperse particles by using microfluidics: control over size, shape, and composition." Angewandte Chemie-International Edition **44**(5): 724-728.

Yanagisawa, K., F. Moriyasu, et al. (2007). "Phagocytosis of ultrasound contrast agent microbubbles by Kupffer cells." Ultrasound in Medicine and Biology **33**(2): 318-325.

Zeqiri, B., P. N. Gelat, et al. (2003). "A novel sensor for monitoring acoustic cavitation. Part I: Concept, theory, and prototype development." IEEE Transactions on Ultrasonics Ferroelectrics and Frequency Control **50**(10): 1342-1350.

Zhao, S., M. Borden, et al. (2004). "Radiation-force assisted targeting facilitates ultrasonic molecular imaging." Mol Imaging **3**(3): 135-48.

Zhao, S., D. E. Kruse, et al. (2007). "Selective imaging of adherent targeted ultrasound contrast agents." Physics in Medicine and Biology **52**(8): 2055-2072.

Zimmerman, W. B., V. Tesar, et al. (2008). "Microbubble Generation." Recent patents on engineering **2**(1): 8.

Biography

Cherry Chen Chen was born on October 26, 1984 in Tianjin, China. At the age of sixteen, she sailed along the western wind and came to New York to live with her grandmother in Flushing, NY. She attended John Bowne High School and graduated in 2003 as the salutatorian in her class. After high school, she followed her mother's footstep and joined the Chemical & Biological Engineering Department at Polytechnic University, Brooklyn, NY. During her undergraduate education, she worked with Dr. Jovan Mijovic and Dr. Mary Cowman to study the rheological properties of hyaluronan, during which time she discovered a strong interest in scientific research. She received her Bachelor of Science degree in 2007 with Summa Cum Laude honor.

Cherry was accepted to the Department of Chemical Engineering at Columbia University as a PhD student in 2007. She joined the research group of Dr. Mark Borden and began her study on engineering microbubbles as ultrasound contrast agents for molecular imaging. During her time at Columbia University, she co-authored several research articles and gave presentations at national/international conferences. She received her Doctoral of Philosophy degree in 2011. After graduation, she will continue her research on microbubbles and hopes to eventually develop these novel agents for clinical cancer therapy. As an alternative, she also wishes to travel around the world in 80 days.